Maximilian Besenhard, BSc

Synthesis and Tuneable Properties of Nanoporous Platinum

MASTER THESIS

For obtaining the academic degree
Diplom-Ingenieur

Master Programme of
Technical Physics

Graz University of Technology

Supervisor:

Univ.-Prof. Dr.rer.nat Roland Würschum

Institut für Materialphysik

Graz, November 2010

Maximilian Besenhard, BSc

Synthese und durchstimmbare Eigenschaften von nanoporösem Platin

MASTERARBEIT

zur Erlangung des akademischen Grades
Diplom-Ingenieur

Masterstudium Technische Physik

Graz University of Technology

Technische Universität Graz

Betreuer:

Univ.-Prof. Dr.rer.nat Roland Würschum

Institute of Material Physics

Graz, November 2010

Gewidmet meinem Vater,
der mir zeigte was möglich ist
und mir immer ein Vorbild sein wird.

Abstract

Synthesis and Tuneable Properties of Nanoporous Platinum

This thesis deals with measurements of the electrical resistance of nanoporous platinum in dependence of electrochemical surface charging. By inserting the sample into an electrochemical cell and applying a chargingvoltage, a field induced superficial charge at the topmost atomic layer can be created at the metal-electrolyte interface. Due to the high surface-to-volume ratio of nanoscale samples this influence causes macroscopic changes in physical properties like the electrical resistance or the magnetization.

Nanoporous platinum samples were generated by means of dealloying a CuPt starting alloy. This process results in a bicontinuous porous network with a high surface-to-volume ratio but with a lower percentage of grain boundaries compared to nanocrystalline samples. The high fragility of the nanoporous platinum samples limited the applied chargingvoltages. Hence resistance measurements were mainly performed in the so-called pseudocapacitive region, with no charge transition between the metal and the electrolyte.

The initial reversible increase of R with positive charging obeyed the same sign of charging coefficients as that of nanoporous gold and nanocrystalline platinum. Upon multiple cycling or increasing the charging voltage, sign inversion of the charging coefficient occurs. Furthermore, this sign inversion is reversible, i.e. the sign of the charging coefficient can be tuned by means of the applied potentials. The observed relative resistance changes upon capacitive charging are much higher than those reported for nanoporous gold and nanocrystalline samples. This is in good agreement with the models that the resistance in nanocrystalline samples is mainly affected by grain boundaries and that additional alterations in the d-band filling permit higher variations in resistivity.

Furthermore, initial studies of the magnetic behavior of nanoporous platinum in dependence of electrochemical charging and initial attempts of dealloying a homogeneous starting alloy using ionic liquids as electrolytes were performed.

Kurzfassung

Synthese und durchstimmbare Eigenschaften von nanoporösem Platin

Diese Diplomarbeit befasst sich mit Messungen des elektrischen Widerstandes von nanoporösem Platin in Abhängigkeit von der Beladung. Der Einbau der Probe in eine elektrochemische Zelle ermöglichte es, mittels Anlegen einer Beladungsspannung, eine Feld induzierte Überschussladung der obersten Atomlage an der Metall/Elektrolyt Grenzfläche zu erreichen. Aufgrund des hohen Oberfläche zu Volumen Verhältnisses von nanoskaligen Proben, kann eine makroskopische Veränderung physikalischer Eigenschaften, wie des elektrischen Widerstandes und der Magnetisierung, erreicht werden.

Nanoporöses Platin wurde über den Prozess der elektrochemischen Korrosion (sog. Dealloying) aus einer CuPt Legierung hergestellt. Dieser Prozess erzeugt ein kontinuierlich zusammenhängendes poröses Netzwerk mit einem großen Oberflächen zu Volumen Verhältnis aber einem geringeren Anteil an Korngrenzen im Vergleich zu nanokristallinen Proben. Die starke Brüchigkeit der nanoporösen Proben schränkte den Bereich der Beladungsspannungen ein. Auf Grund dessen, wurden Widerstandsmessungen hauptsächlich im sogenannten pseudo-kapazitiven Bereich durchgeführt, in dem kein Ladungstransfer zwischen Metall und Elektrolyt satt fand.

Der anfängliche reversible R Anstieg mit positiver Beladung folgte dem gleichen Vorzeichen des Beladungskoeffizienten wie im Falle von nanoporösem Gold und nanokristallinem Platin. Durch wiederholtes Zyklieren oder Erhöhen der Beladungsspannung ergab sich eine Vorzeichenumkehr des Beladungskoeffizienten. Diese Vorzeichenumkehr ist reversibel. Das Vorzeichen des Beladungskoeffizienten konnte belibig eingestellt werden, z.B. durch die Wahl geeigneter Beladungsspannungen. Die gemessenen relativen Widerstandsänderungen durch kapazitive Beladung waren wesentlich größer, als jene von nanoporösem Goldproben und nanokristallinen Platinproben. Dies stimmt mit dem Modell überein, dass der Widerstand nanokristalliner Proben hauptsächlich von Korngrenzeneffekten beeinflusst wird und, dass die zusätzlichen Änderungen der Besetzung des d-Bandes auch höhere Änderungen der Widerstandes zulassen.

Des Weiteren wurden erste Versuche zur Durchstimmbarkeit der Magnetisierung nanoporöser Platinproben und des Dealloyingprozesses in ionischen Flüssigkeiten durchgeführt.

Contents

Abstract **III**

Kurzfassung **V**

Contents **ii**

1 Introduction **1**

2 Experimental Basic **3**

2.1 (Cyclic) Voltammetry (CV) 3

2.2 Chrono Amperometry (CA) 6

2.3 Double layer charging 6

2.4 Chemical determination of the surface area 7

2.5 Four-point method of resistance measurements 9

2.6 Formation of nanoporosity via dealloying 10

2.7 Principles of tuning the resistance of platinum and other metals by means of electrochemical charging 13

2.8 Introduction of the charging coefficients ϱ and $\varrho_{size.ind.}$ to compare charge driven resistance changes 16

3 Experimental Procedure **21**

3.1 Fabrication of nanoporous platinum samples by means of dealloying 21

3.2 Preperation of nanocrystalline platinum samples 23

3.3 Voltammetry and chrono amperometry 23

3.4 Resistance measurements in dependence of charging 24

4 Experimental Results **29**

4.1 Sample Characterization 29

4.2 Resistance measurements in dependence of electrochemical charging 39

4.3 Initial studies with ionic liquids 55

5 Discussion **61**
5.1 Resistance measurements in dependence of electrochemical charging 61

6 Summary and Conclusion **71**

A Initial studies of magnetic behavior of nanoporous platinum in dependence of electrochemical charging **75**
A.1 Principle of tuning the Magnetization of platinum 75
A.2 Procedure of magnetic measurements in dependence of electrochemical charging . 77
A.3 Results of magnetic measurements in dependence of electrochemical charging . . . 78
A.4 Discussion of magnetic measurements in dependence of electrochemical charging . 79
A.5 Additional calculations of chapter A.4 81

B Additional information and data according to resistance measurements **83**
B.1 Additional plots for chapter 4.2.2 83
B.2 Additional plots for chapter 4.2.3 84
B.3 Resistance correction for the TUG-NCP-samples 85

Bibliography **89**

Acknowledgments **97**

Chapter 1

Introduction

This thesis is about the synthesis of nanoporous platinum (NPP) samples and tunable physical properties that became measurable using these kind of specimens. Nanoporous platinum is a bicontinuous porous network consisting of ligaments with a diameter of only a few nanometers. This porous network facilitates the penetration of an electrolyte to all surface regions of the sample. Based on the works of Wahl [1] and Sagmeister [2] who performed resistance measurements on nanoporous gold (NPG) and nanocrystalline platinum (NCP), the focus of this master thesis was on measurements of the tunable resistance of nanoporous platinum. Nanoscale materials feature a high surface-to-volume ratio and a lot of their properties are dominated by interface phenomena. The concept of this work is to change the macroscopical properties of these materials by means of a field induced modification of their interfaces [3]. The electrical field was obtained from applying a potential between the specimen and a counter electrode in an electrochemical cell, which leads to the attraction of ionic species to the surface, similar to the charging of a capacitor. In the case of metals, this surface charging enables a tuning of the lattice parameter and the correlated macroscopic length [4, 5, 6], the paramagnetic susceptibility [7], the electrical resistance [2, 1, 8] and the reflectivity [9]. Tunable properties have been in focus of intensive research over the last years and the mentioned publications give only a brief excerpt. The properties of bulk metals can not be tuned by means of surface charging. Because of the high density of (nearly free) charge carries, external fields yields variations from charge neutrality only in the topmost monolayer. In contrast, in the case of slightly doped semiconductors, the penetration depth of the surface charge region may reach dimensions of many atomic layers, which permits the application of latter field effect for transistors. Nanoporous platinum samples were fabricated by means of dealloying. Dealloying, is the selective dissolution of one or more less noble components out of an alloy, ending up in a bicontinuous porous network of the remaining components. Theoretical models about the morphological process resulting in these porous networks can be found in works of Erlebacher et al. [10, 11]. Used starting alloys were prepared by the group of Jin from the Karlsruher Intitute of Technology and the dealloying process was performed in cooperation with S. Landgraf from the Institute of Physical and Theoretical Chemistry at the TUGraz.

As mentioned before, this thesis is based on the works of Sagmeister et al. [9, 2] who performed resistance measurements on nanocrystalline platinum samples, which were prepared by means of grouting and agglomeration powder, and Wahl et al. [12, 1] who performed resistance measurements on nanoporous gold samples, prepared by means of dealloying. Both kind of materials differ tremendously in the amount of grain boundaries, which is much higher in the case of nanocrystalline samples. Resistance measurements of nanoporous platinum samples will be presented within this master thesis for the first time. A comparison of the obtained results to those of nanocrystalline platinum and nanoporous gold samples should reveal information about the influence of grain boundaries and the d-band filling on the resistance.

Additionally, initial studies of the magnetic behavior of nanoporous platinum in dependence of electrochemical charging and initial attempts of dealloying a homogenous starting alloy using ionic liquids as electrolytes are shown as well.

Chapter 2

Experimental Basic

In this chapter the principles and techniques of measurements which are applied in this master's thesis are discussed. For the reason that special focus lies on electrochemistry, some frequently used techniques are explained separately in sections 2.1 -2.4. The general characteristics of nanoporous samples, fabricated via dealloying, are discussed in section 2.6 in detail because of their importance to subsequent discussion in chapter 5.

2.1 (Cyclic) Voltammetry (CV)

Voltammetric methods are the main techniques used in this thesis to diagnose and control chemical processes at the surface of the sample. Their principles are discussed below.

2.1.1 Three electrode system

Straight after immersing a metal in a solution containing ions of the same metal, the equilibrium condition of their chemical potentials,

$$\mu_{Cu^{++}}(solution) = \mu_{Cu^{++}}(metal) \tag{2.1}$$

may not be valid. This results in ion exchange, metal deposition or metal dissolution (depending on the sign of the difference in chemical potentials). Nevertheless, this reaction will stop before reaching equilibrium condition (see equation 2.1) because of an arising potential difference between the phases resulting from electrolyte double layer charging at the interface. For the reason that additional work is necessary to overcome the arising potential difference, the equilibrium condition differs from equation 2.1. The new equilibrium condition is the equality of electrochemical potentials μ^*:

$$\begin{aligned}\mu^*_{Cu^{++}}(solution) = \mu_{Cu^{++}}(solution) + z_i \cdot F \cdot \varphi(solution) = \\ \mu_{Cu^{++}}(metal) + z_i \cdot F \cdot \varphi(metal) = \mu^*_{Cu^{++}}(metal)\end{aligned} \tag{2.2}$$

The potential difference $\Delta\varphi = \varphi(solution) - \varphi(metal)$ is the corresponding Galvani potential, F the Faraday constant and z_i the ion valency[1]. Measuring the Galvani potential is not possible, but Galvani potential differences are easily accessible by measuring the voltage drop between two (metal-) electrodes immersed in electrolytes containing ions of the same metal. The Galvanic potential of a standard hydrogen electrode (SHE) at standard conditions [13] was defined as zero arbitrarily.

Measuring the Galvanic potentials for a non zero current is not possible due to the simple method described above. Current flow leads to overpotentials, for example, due to diffusion or hindered reactions. These overpotentials would occur (differently) on both electrodes used to measure the potential difference. Hence a third electrode is used as a reference. The potential difference between the additional electrode with a known electrode potential, called a reference electrode (RE), and one of the prior electrodes named a working electrode (WE), measured high ohmic, leads to the correct WE potential [14]. The reference electrode should be placed close to the investigated electrode, called working electrode (WE), to reduce the (unknown) ohmic voltage drop resulting from current flow through the electrolyte. The third one is called a counter electrode (CE) and is used for current supply only.

2.1.2 Cyclic voltammetry (CV)

For the application of cyclic voltammetry [14], which is often referred as electrochemical spectroscopy, a three electrode system is required. The potential between the WE and RE is ramped linearly versus time between two distinct values, U_l-U_h (the lowest U_l and the highest U_h). Reaching one of these potential values, the potential ramp is inverted which leads to a triangular voltage versus time behavior. The current from WE to CE is plotted versus this potential. The potential between WE and RE is controlled via the applied potential difference between WE and CE. Using aqueous electrolytes U_l-U_h are often chosen as the potentials for hydrogen- and oxygen gas evolution. Different potentials enable different reduction and oxidation reactions. The position and shapes of the current peaks depend on the WE-material, ion concentrations of the used electrolyte, the potential sweep rate $v[\,\mathrm{mVs}^{-1}]$ and prior chemical treatment. Usually the potentials for hydrogen- and oxygen gas evolution are chosen as boundaries, because this guaranties complete reproducibility[2].

Figure 2.1 shows a CV for platinum in 1-M KOH, recorded using a sweep rate of $v = 100\,\mathrm{mVs}^{-1}$. The peaks are identified as follows. Double layer charging between $450 - 550\,\mathrm{mV}$, followed by

---

[1] The electrochemical potential difference is defined as the difference in **molar** Gibbs energy at specified potentials.

[2] Under the assumption that all reactions are chemically reversible in this potential regime.

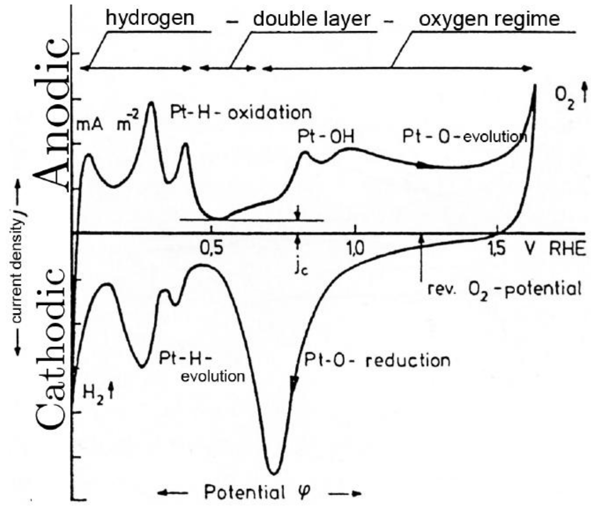

Figure 2.1: Schematic cyclic voltammogram of platinum, redrawn after [14]

chemisorption of oxygen

$$Pt + OH^- \rightarrow Pt - OH + e^- \tag{2.3}$$

from $\approx 550\,\mathrm{mV}$ and

$$2Pt - OH \rightarrow Pt - O + H_2O \tag{2.4}$$

from $\approx 800\,\mathrm{mV}$ and oxygen evolution above $1600\,\mathrm{mV}$. Upon cathodic sweeping oxygen is reduced with a few $100\,\mathrm{mV}$ overpotential (because of oxygen chemisorption), with a subsequent double layer regime up to $350\,\mathrm{mV}$, followed by atomic hydrogen deposition, the hydrogen regime:

$$Pt + H_2O + e^- \rightarrow Pt - H + OH^-. \tag{2.5}$$

After hydrogen gas evolution at U_l, the previously generated molecular hydrogen and the deposited atomic hydrogen are oxidized in the anodic sweep. It should be mentioned here that the exact reaction mechanisms of oxide film formation are unknown even for platinum. The correct electrode processes are still a matter of debate [15, 16].

Exact comparability of cyclic voltammograms in literature is difficult. The potential of current extrema can vary with the experimental procedure, for example because of different temperatures or distances between the WE and RE. The shape of single peaks and the general pattern can also vary for several reasons. One of them is the surface character, e.g porous or planar. Usually the peaks are sharper in the case of planar surfaces. In chapter 3.3.1 it is shown that in the case of high porous platinum samples, the expected peak pattern could only be obtained at very low sweep rates $v = 1\,\mathrm{mVs}^{-1}$ and below. Higher sweep rates give rise to a smearing out of the CV characteristics (see figure 3 in [5]) which was explained due to limited transport kinetics in the nanoporous systems [5]. Even different surface orientations of a single crystal exhibit discrepancies in corresponding CVs. This leads to superpositions of peaks in case of polycrystalline surfaces, smearing out a characteristic peak pattern even more.

2.2 Chrono Amperometry (CA)

The chrono amperometry is a related technique. The current is recorded for a specific potential. In contrast to the recording of a cyclic voltammogram, the potential is held constant and does not change with time. The form of an CA curve , current versus time ($I(t)_{const.Pot}$), gives information about reaction kinetics. Reactions proceeding at different time scales, for example double layer charging and chemical reaction at the surface, can be distinguished [12].

2.3 Double layer charging

The theories concerning the electrochemical double layer at metal/electrolyte interfaces are discussed in detail in [14]. Some concepts and notations are briefly discussed here. According to the *Helmholtz model*, the double layer (and the related potential gradient) is divided in an inner and outer Helmholtz layer. The inner Helmholz layer originates from a layer of solvated ions accumulated at the interface. It is much narrower ($\frac{a}{2}$ where a is the radius of the solvation shell) and has a higher potential gradient than the outer layer. The latter is also referred as a diffuse layer and the assigned potential gradient, determined by the charge distribution, is obtained from the the Maxwell-Boltzmann distribution. The extension of the outer Helmholtz layer (κ) can be up to a few $10\,\text{nm}$ but decreases drastically with increasing ionic strength. In the case of solutions with concentrations of $0.1\ \frac{mol}{l}$, the outer Helmholtz layer can even be as thin as or thinner than the inner ($\kappa < 0.1\,\text{nm}$, $\frac{a}{2} \approx 0.1 - 0.5\,\text{nm}$) [14]. As mentioned in the previous section, sample charging is referred as double layer charging if no chemisorption (chemical reactions of adsorbed species with surface atoms/molecules) takes places. Nevertheless, capacitive currents are always present in the entire potential range. Exclusively capacitive charging of an oxidized surface is often referred as “pseudo capacitive charging”. A draft of the described situation is shown in figure 2.2.

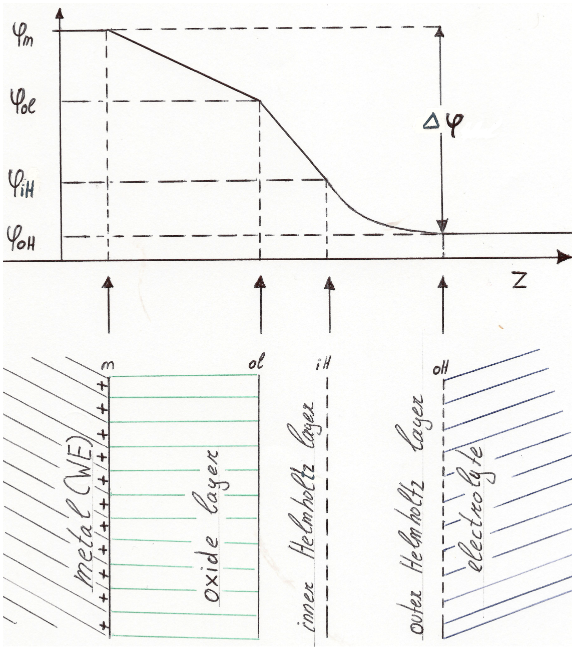

Figure 2.2: Draft of pseudo capacitive charging according to the Helmholtz model, and a schematic potential curve

2.4 Chemical determination of the surface area

As mentioned in the introduction, a large interface-to-volume ratio is necessary to observe effects like changes in resistance or magnetization due to electrochemical charging. Charge effects should be related to the surface area to be comparable, as proposed in chapter 2.8. Kinetics of chemical reactions are influenced by the surface area and its characteristics as well, and play a major role in CV evaluation. Because the knowledge of NPP-samples surface area seems to be quite desirable, its determination (or better estimation) was investigated. Physical methods like BET measurements (BET stands for the inventors of the BET-model; Brunauer, Emmet, Teller) used in [9] were not performed. The surface area was determined chemically using methods designed for CV because of its accessibility. A selection of different methods are presented in [17]. The authors discussed their reliability and principles. Applicability of different methods is reported to depend on the investigated material and its structure. The obtained surface area values are also described as depending on the determination method, which indicates that obtained results have to be treated carefully. Both methods used in this thesis to investigate the real surface area are described below.

2.4.1 Determination of the surface area using voltammetry

For this method CVs with different sweep rates are recorded in a narrow potential range for which only double layer charging is expected. In fact it does not have to be the double layer charging regime (see figure 2.1) but only a lack of specific ad- or desorption is required. The currents in the middle of this range, plotted versus their sweep rates, should result in a straight line, whose slope is the total differential capacitance τC^d of the interface:

$$\tau C^d = \frac{dQ}{dE} = I \cdot \frac{dt}{dE} = \frac{I}{\frac{dE}{dt}} = \frac{I}{v}. \tag{2.6}$$

The differential capacity C^d is normalized to the surface area [14][3]. By means of comparing τC^d [F] with a reference value C^d $[\frac{\mathrm{F}}{cm^2}]$, the actual surface area can be obtained:

$$\frac{\tau C^d}{A} = \frac{\tau C_0^d}{A_0} \Rightarrow A = \frac{\tau C^d}{\frac{\tau C_0^d}{A_0}} = \frac{\tau C^d}{C_0^d}. \tag{2.7}$$

2.4.2 Determination of the surface area from charging curves

The principle of this method is that the charge attributed to a specific ad- or desorption is expected to result in a known occupancy. Therefore, from the total accumulated charge the total surface area can be determined if the specific charge associated with the process is known. In the case of platinum the evaluation of the atomic hydrogen ad- or desorption peak is recommended. Oxygen ad- or desorption is reported to give non-consistent values of the surface area [18]. This divergence is assumed to result from the non-equilibrium character of oxygen monolayer adsorption [15] and from gas accumulation with time [18]. Details of the surface area determination of NPP are described next.

If one assumes a coverage with (decoverage of) a hydrogen monolayer arising through the cathodic (anodic) sweep in a CV between hydrogen gas evolution and the commencement of the double layer regime, the recorded charge can be compared to a consumption of $\approx 210\,\mu C \mathrm{cm}^{-2}$ required for a monolayer of atoms (assuming a density of $1.31 \cdot 10^{15}$ atoms cm^{-2}, which is close to that pertaining to the (100) face). $210\,\mu C\mathrm{cm}^{-2}$ is a value generally expected for polycrystalline platinum. It is taken as an average value between major low index faces for polycrystalline surfaces [17][4]. Corrections have to be made in order exclude the affect of additional double layer charging. Figure 2.3 explains how to determine the charge out of a CV. The method implies that the potential of coverage with one monolayer can be identified and lies below potentials at which hydrogen evolution becomes significant. A proper determination of the end point of ad- or desorption can be attained by extrapolating Q_H to infinite sweep rate which enables separation between adsorption and Faradaic charges for H_2 evolution, or due to performing voltammetric measurements at low temperatures as described by Trasatti and Petrii [17] [5]. It should be mentioned that for low sweep rates anomalous effects in the voltammetric behavior are reported as becoming more remarkable [20]. This is explained on the basis of absorption of hydrogen into the porous structure and its influence on the different stages of the hydrogen electrode reaction.

---

[3] $C^d = \frac{\tau C^d}{A} = \frac{I}{v \cdot A} = \frac{j}{v}$.

[4] A value of $200\,\mu C\mathrm{cm}^{-2}$ is reported by Binder *et al.* [19].

[5] Mentioned techniques could not be applied because of limited resources.

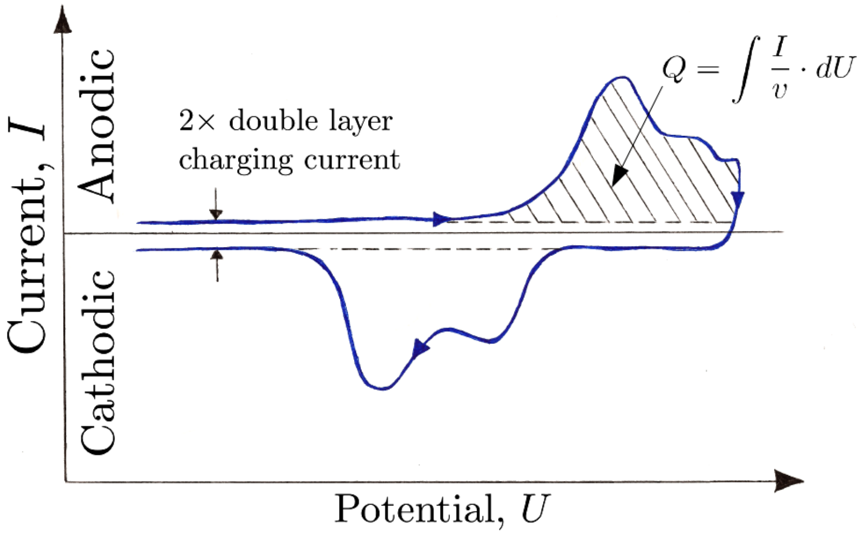

Figure 2.3: Typical cyclic voltammogram for an electrochemical surface process. The charge assigned to chemisorption only can be calculated from the shaded area.

2.5 Four-point method of resistance measurements

Because exact measurements of the resistivity in metals are not trivial, the influence of connection resistances or cables can not be neglected. Measuring only the resistance of the sample and nothing else is possible with the aid of a four-point method. Its principle is sketched in figure 2.4. The sample has to be connected by four wires, two outward and two between. A constant, well-known current is supplied via the outward wires. This results in voltage drop according to Ohm's law $U = I \cdot R$. This voltage drop is measured for resistance calculation by use of the inner wires, named sensing wires.

$$R_{between\ inner\ wires} = I_{supplied} \cdot U_{measured} \tag{2.8}$$

The high resistance voltage measurements between the sensing wires ensure negligibility of contact resistances.

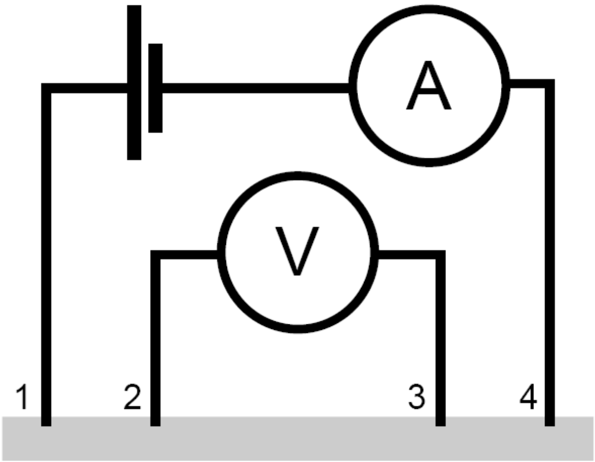

Figure 2.4: The basic idea of the four-point method

2.6 Formation of nanoporosity via dealloying

This section deals with the principles of dealloying, especially for $Cu_{75}Pt_{25}$-alloys used in this work. In this thesis all compositions are denoted in atomic percent. Dealloying became an important tool to generate samples exhibiting an extremely high surface area and many publications using different starting materials are presented in today's literature.

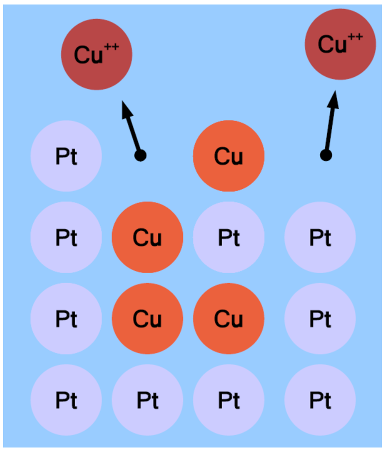

Figure 2.5: Basic dealloying principle

Dealloying is the selective dissolution of one or more, less noble component(s) out of an alloy, ending up in a bicontinuous porous network of the remaining components. The following assumptions are made for binary alloys. The basic principle is sketched in figure 2.5 for a Cu-Pt alloy. The driving force for this dissolution could be the presence of oxidizing species or an applied voltage as used here. One would think that applying voltages leading to the dissolution of the less noble component and do not oxidize the more noble component, would lead to surface enrichment of the latter and end up in passivation [21]. The distinctive feature is the evolution of a nanoporous structure if the applied potential exceeds a certain potential, referred as critical potential E_{crit} in literature. This nanoporous structure, an example is given in figure 2.6b, looks like a metal foam consisting of connected ligaments. Porosity formation is expected to be feasible up to sample thicknesses of more than 4 mm [22]. The exact mechanism for the formation of such a porosity is still a matter of debate. Erlebacher presented a kinetic Monte Carlo model incorporating site coordination-dependent surface diffusion and dissolution [10]. This model depicts the measurable electrochemical characteristics such as polarization curves and measured critical potentials [23].

Surface diffusivity seems to play a major role in this morphological process. The order of surface diffusivity differs drastically between Au and Pt (10^{-14} cm/s for Au and 10^{-18} cm/s for platinum[6], both at room temperatures [24]). The low surface diffusivity of platinum is said to be the reason for the evolution of smaller ligament structures and a lower coarsening insusceptibility at room temperature of NPP compared to NPG [23]. Jin et al. describe the generation of extraordinarily small NPG structures (ligaments of $1-2$ nm in diameter) underneath an additional oxide layer [25]. The smaller structures may be assigned to the inhibited surface diffusion of Au through oxide film formation. The initial structures depend on the dealloying potential. Higher potentials lead to smaller initial nanoporous structures with characteristic size down to 4 nm for NPG [6].

Nanoporous samples, which differ from nanocrystalline samples, are of special interest for the resistance measurements because of their lower amount of grain boundaries (compared to the same surface to volume ratio) as already mentioned in the introduction. The presence or evolution of porosity is often proved through peak broadening in literature [26, 27, 28]. Peak broadening depends on the size of the coherent scattering domain (CSD). A decreasing CSD leads to increasing peak broadening, which is often used to estimate grain sizes [29]. Obviously the CSD size decreases through dealloying. The question is now whether this is because of the (slightly) different orientations of the structure in the ligaments due to varying tension or dislocations, or because of the creation of new grain boundaries. So the question of the transformation of preexisting and evolution of new grain boundaries should be treated very carefully.

Summarized by Sun et al. [30] polycrystalline ligaments with grain sizes $\approx 10-30$ nm had been reported for a sample made by dealloying $Ag_{58}Au_{42}$ by Biener et al. [31]. The same authors showed nanocristallinity within Au ligaments with TEM-micrographs [32] and proposed that the high strength levels determined for NPG are due to ligaments which contain grain boundaries [33]. Nevertheless it is said in [30]: *In the current study, NPG ligaments with withs $\approx 10-30$ nm were observed to be single crystalline, and poly- or nanocrystalline ligaments were seen only in a sample subjected to extended dealloying*. They also presented TEM-micrographs showing grain boundaries containing multiple ligaments. The topic of grain boundaries in NPG was investigated by Van Petegem et al. [28]. From electron backscatter diffraction (EBSD) before and after dealloying, the conservation of the grain structure is approved.

There is another very important difference between the NPG and NPP samples fabricated for this thesis. A preferential attack of, and electrolyte penetration into the alloy along grain boundaries is reported by Pugh et al. [23, 24]. The proposed dealloying mechanism is demonstrated in 2.6a. The surface enrichment of Cu on $Cu_{71-80}-Pt_{29-20}$ alloys was demonstrated through the the open potential, which was about the same as for pure copper independent of the Pt concentration [23]. A higher copper concentration at the surface of copper rich Cu-Pt nanoparticles, than expected from the atomic composition, is also reported in [34]. The authors argue that this is consistent with segregation of copper, because of its lower surface energy, reported in [35]. The author of this thesis interprets the work of Ruban et al. differently and can hardly find a reason for copper segregation in Pt-Cu alloys from this paper. Whether or not, Ruban et al. calculated segregation energies for impurities in a host metal. Therefore, it should be taken into account that segregation energies, in the case of binary alloys with higher concentrations of the second constituent, may differ significantly from that of pure host metals. Summarized in the work of Yuguang et al. [36], two experimental studies on a $Cu_{75}Pt_{25}$ (111)-surface lead to different results for segregation. Using low energy ion scattering (LEIS), a surface compound of $20\ \%$-Pt at the first layer (slight copper segregation) was found by Shen et al [37]. Gauthier et al. [38] found slight Pt segregation at the topmost layer. The authors examined a disordered $Cu_{75}Pt_{25}$-sample by low energy electron diffraction (LEED). The enrichment of copper at the grain boundaries described by Pugh et al. [23] may result from a different sample fabrication and no exact proof for copper segregation is presented in the work of Gupta et al. [34].

---

[6] The diffusion coefficient in the alloy at the electrolyte interface may differ significantly from that of pure metals in vacuum [11].

Irrespective of whether the preferential attack of grain boundaries originates from copper enrichment or heterogeneity of boundary atoms, it leads to extremely high sample brittleness, which handicaps the sample handling extremely. This made rational measurement procedures (e.g. weighing, X-ray defraction,...) for sample characterization impossible.

For the dealloying process, a solid solution was required. There are publications about the generation of nanoporous systems starting with multiple phases [39], which should result in more stable heterogeneous samples, but the focus for this thesis was on the fabrication of homogeneous samples. The phase diagrams of the used starting alloys show complete miscibility [40, 41].

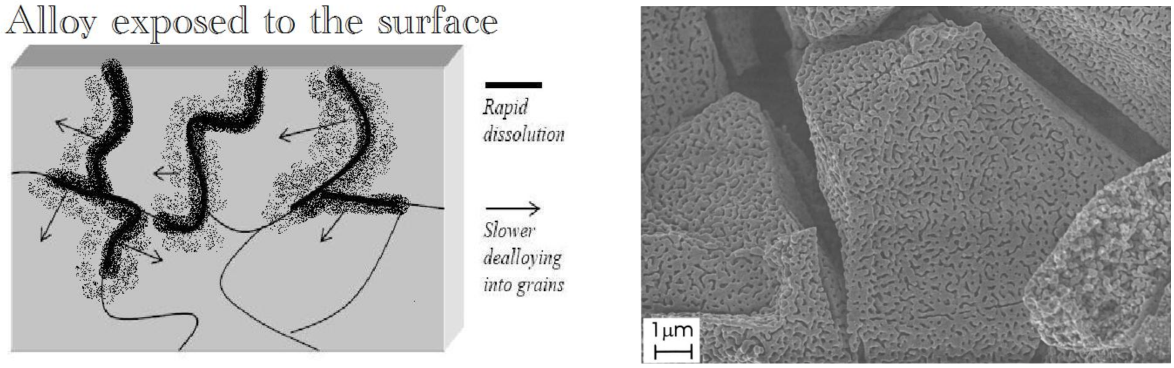

(a) Presumed dealloying mechanism. Redrawn from [24]

(b) SEM image of bicontinuous porosity created by the dealloying of $Cu_{80}Pt_{20}$ in 1-M $HClO_4$ at 1.24 V vs. NHE for 20 hours followed by heat-treatment at 800°C for 15 minutes (Reproduced by permission of The Electrochemical Society) [23].

Figure 2.6: Development of NPP in $CuPt$ alloys

2.7 Principles of tuning the resistance of platinum and other metals by means of electrochemical charging

In this section the principles of resistance changes, especially for platinum, due to surface effects are discussed. Again a large surface-to-volume ratio is required to detect the surface sensitive resistance variations described below. The incorporation and removal of impurities, variations of charge carrier concentrations at the metal-electrolyte interfacial region, different probabilities for diffuse scattering of conducting electrons, and variations in thickness of the conducting branches are the accepted mechanism for resistance variations. The classification into three different contributions to resistivity changes in electrochemistry, the field effect, the size effect, and surface adsorption are adopted from the review about surface technique in electrochemistry by Tucceri [8]. In this review experiments and theories for resistance changes of thin metal films are discussed, which should also be valid for the nanoporous structures investigated within this work.

2.7.1 The field effect

After immersing a metal sample in the electrolyte and applying a voltage (see figure 2.7a) an electrochemical double layer is formed. Electrochemical double layer charging can lead to such high electric field strengths in the entire interfacial region, which can only be attained elsewhere at cone ends in vacuum [42]. An applied positive potential, for example, led to the migration of anions to the WE , which can be compared to the charging of a capacitor in the absence of chemical reactions because no charge transfer happens between the metal and electrolyte, and electron depletion in its surface region. In this surface region of thickness δ a state of solid matter results that deviates from charge neutrality. The screening δ, in case of metals, occurs within diameters of several lattice planes [3].

To detect the resistivity changes corresponding to the surface region deviating form charge neutrality, called the space-charge-region from now on, a high percentage of surface atoms is required. Approximating the ligament structure of the nanoporous structures, see section 2.6, to be ideally cylindric with a diameter d, the percentage of volume ω assigned to the surface-charge-region of the thickness δ results in

$$\omega = \frac{4 \cdot \delta}{d} \tag{2.9}$$

[3]. Ligament diameters of $1.52\,\text{nm} - 1.64\,\text{nm}$ are reported for NPP fabricated from dealloying $Cu_{75}Pt_{25}$-alloys in H_2SO_4, as used for this thesis, in the PhD thesis of Pugh [24]. Assuming a screening length of $\delta = 0.4\,\text{nm}$ as done by Wahl [12] yields a value of $\approx 100\%$ affectable material according to equation 2.9. About the same values are reported in case of NPG-samples in [12]. The latter approach makes only a rough estimate and the implausible value of $\omega = 1$ may be valued far to high [43].

In the following, the models of resistance variations according to literature will be presented. To go conform with available literature the models presented in this section, examine resistance variations of thin films. Because most literature deals with thin films, variations of the thin film resistivity by means of charging are discussed here. To explain resistivity changes due to the field effect, the Drude model, based on the free electron model, is often used.

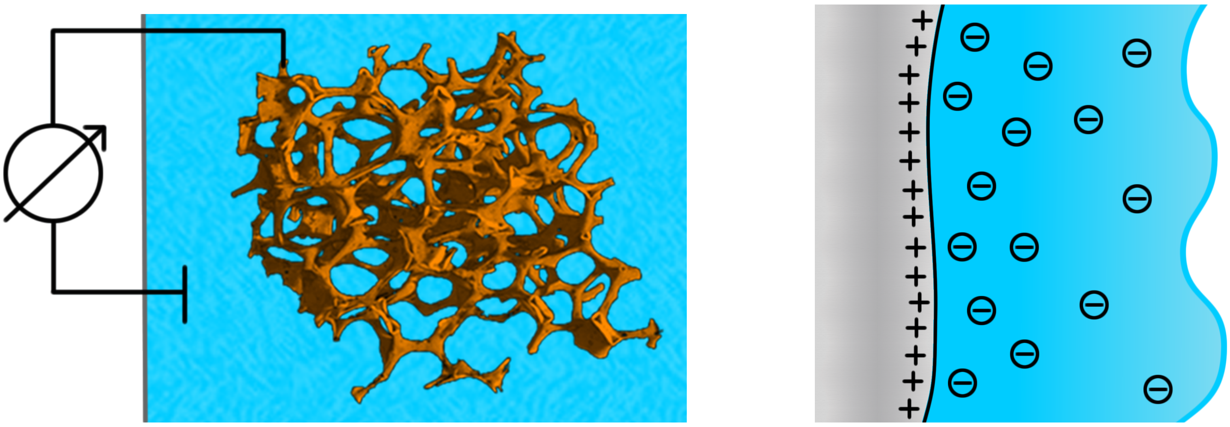

(a) Concept of charging porous structure [44]

(b) Double layer at the interface

Figure 2.7: Principle of charge carrier depletion on the metal/electrolyte interface due to electrical double layer charging [12].

$$\sigma_{Drude} = \frac{ne^2\tau}{m^*} \tag{2.10}$$

Here σ denotes the conductivity, n the number of electrons per volume, e the electron charge, τ the relaxion time and m^* the effective mass which deviates from the free electron mass because of lattice and electron-electron interactions. If Δn labels the difference in electron density in the surface region δ and D the thin film thickness, the relative conductivity changes obtained from the Drude model are

$$\frac{\sigma - \sigma_0}{\sigma_0} = \frac{\delta \cdot \Delta n}{\delta \Delta n + D \cdot (n_0)}, \tag{2.11}$$

where σ_0 is the conductivity when $\Delta n = 0$ at n_0. Nevertheless the equation 2.10 is a drastic oversimplification, even for the *free electron model*. A more sophisticated approach is discussed in [45], based on *linear response theory* taking into account the speed at the Fermi surface , and the density of states (DOS) at the Fermi level [7]. The influence of the DOS on τ is discussed in the works of Sagmeister et al. [9, 2].

Platinum is a transition metal, and the models mentioned above are not adequate to describe the resistivity changes resulting from charge alterations at the surface due to the field effect. The conductivity of platinum is mainly affected from the scattering of s-band electrons, which are said to be mainly responsible for the electron transport into empty states of the d-band. This may be approximated by,

---

[7] $\sigma_{lin.res.} = (e \cdot v_F)^2 \tau N(E_F) \frac{1}{3}$; v_F=Fermi velocity ; $N(E_F)$=DOS at the Fermi level.

$$\sigma_{Pt} \propto \frac{\text{number of electrons in the s-band} n_s}{\text{number of holes in the d-band}^{(1/3)}} = \frac{n_s}{N_d(E_F)} \tag{2.12}$$

where $N_d(E_F)$ is the DOS of the d-band at the Fermi level [9]. Figure 2.8 shows the DOS of platinum calculated by Müller et al. [46] exhibiting the characteristics mentioned above.

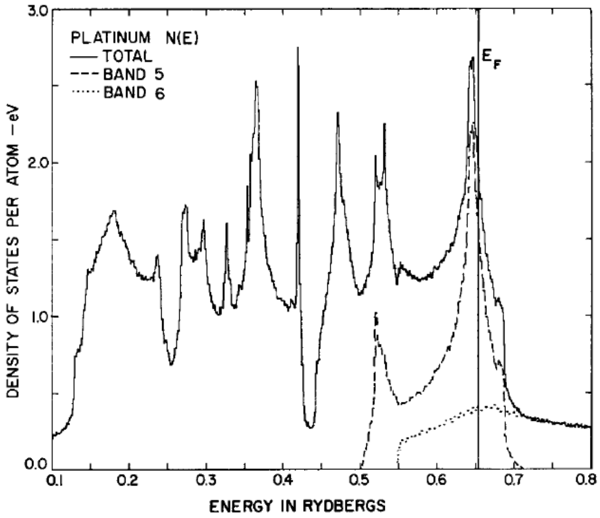

Figure 2.8: The density of states of platinum, N(E), in the d-band region. The authors refer the d and s band as bands 5 and 6. (Reprinted from [46] with permission from Elsevier)

2.7.2 The size effect

If the metal film thickness D approaching values comparable to the mean free path (mfp) of conduction electrons l_0, scattering at the surface becomes dominant. Hence the resistivity of the thin film ρ_{film} starts to increases when D reaches this limit. According to Tucceri [8] the theory developed by Fuchs and Sondheim using the Bolzmann equation to describe free electron gas distribution in an ideal solid, the so called *size effect* on the electron transport properties simplifies to

$$\rho_{film} = \rho_b \cdot \left[1 + \frac{3l_0(1-p)}{8D}\right] \text{, if } \frac{D}{l_0} > 1 \tag{2.13a}$$

$$\rho_{film} = \rho_b \cdot \frac{4(1-p)}{3(1+p)} \left[\frac{D}{l_0} log(\frac{l_0}{D})\right]^{(-1)} \text{, if } \frac{D}{l_0} < 0.1 \text{ and p<<1.} \tag{2.13b}$$

ρ_b denotes the resistivity of the bulk material and p the so called specularity parameter presenting the probability of an electron being reflected specularly or diffuse at the film surface. $p = 0$ for complete diffuse scattering, and $p = 1$ for complete specular scattering.

Fujihira and Kuwana [47] studied the *size effect* in electrochemistry trying to fit experimental data of thin platinum films connected as WE by using equation 2.13a. A fit of the data according to

equation 2.13a could only be attained when taking into account unreasonable l_0 values or $p < 0$. Wissmann [48] discusses modifications of equation 2.13a resulting from increasing scattering of electrons at the inner crystallite boundaries, because of decreasing crystallite sizes in the film with decreasing thickness, reported for films generated as in [47]. He also mentions deviations for transition metals caused by the inapplicability of the *free electron model* for the conduction electrons which is a premise for the validity of 2.13a. This might explain the failure of the fit in the work of Fujihira and Kuwana [47].
The main issue of this subsection was the introduction of the specularity parameter p, which is mentioned to depend on the film structure, roughness, topography, defects and imperfections at the metal film surface and adsorbed species in [8]. Variations in the scattering rate of conduction electrons are discussed to be a main effect on resistance changes, especially for nanoporous structures [1].

2.7.3 Effects of surface adsorption

Tucceri [8] discusses three mechanisms that have been proposed to explain the influence of surface adsorption on thin films resistivity.

1. Adsorption affects the number of free electrons of the metal film
2. Adsorbates form new scattering centers on the metal surface for the conduction electrons.
3. The adsorbate reacts with the surface metal atoms and removes a layer of conducting film.

The challenge for qualitative discussion is that the effects mentioned usually obey the same algebraic sign (e.g. all effects explain higher resistance values) and are difficult to separate. Because of the enormous amount of literature dealing with adsorption phenomena on the resistivity only some papers are mentioned which describe sign inversion in resistivity change [8, 48].

2.8 Introduction of the charging coefficients ϱ and $\varrho_{size.ind.}$ to compare charge driven resistance changes

The comparison of the charge and voltage dependent change in resistance with literature is often restricted because of limited information. The relationship between $\frac{\Delta R}{R \cdot \Delta Q}$ (Q=measured charge), $\frac{\Delta R}{R \cdot (\Delta Q/m)}$ (m=sample mass), $\frac{\Delta R}{R \cdot (\Delta Q/A)}$ (A=surface area of the sample) is not a trivial one and latter relationships can not be compared among each other. A quantitative comparison of charge driven resistance changes should be possible without taking into account the geometry of the sample. If the influence of a surface dependent effect on the resistivity is known, it should be possible to give a sample independent, general relationship of the change in resistance by means of charging. This can in principal be achieved by introducing the relationship $\varrho_{size.ind.}$ presented in the following.

1. **Scaling the resistance changes**
   The following considerations are valid for a porous system comprised of ligaments with identical thickness. Considering a cylindrical metal piece with the resistance R_0, resistivity ρ_0, the length l_{cyl} and the radius r_{cyl}, a change in resistivity of $\Delta\rho$ would result in a geometry independent relationship using

   $$\frac{\Delta R}{R_0} = \frac{\Delta R - R_0}{R_0} = \frac{l_{cyl} \cdot r_{cyl}^2 \cdot \pi \cdot (\Delta\rho)}{l_{cyl} \cdot r_{cyl}^2 \cdot \pi \cdot \rho_0} = \frac{\Delta\rho}{\rho_0}.$$

   Even the comparison of various serial circuits, parallel circuits, and combinations made of latter cylinders would give the same value of $\frac{\Delta R}{R_0}$. The latter is important because, in a simple model the nanoporous or nanocrystalline samples can be considered as a parallel and serial circuit of multiple cylindrical ligaments.

2. **Effect of charging**
   If resistance changes are caused by sample charging, a quantitative relationship should take into account the amount of transferred charge ΔQ. A larger sample (containing more ligaments) with a larger surface area would yield higher values of ΔQ under equal conditions, which is sketched in figure 2.9. Hence a geometry independent charging relationship has to be normalized by the exposed sample surface area A which results in the charging coefficient.

   $$\varrho = \frac{\Delta R}{R_0} \cdot \frac{A}{\Delta Q} \tag{2.14}$$

   A positive charging coefficient ($\varrho > 0$) means that R increases with charging, and a negative charging coefficient ($\varrho < 0$) means an R decrease with charging.

3. **Thickness dependence**
   Possible resistance variations due to charging depend on the amount of sample material exposed to the electrolyte. Hence smaller sample structures, i.e smaller ligament diameters, give rise to higher values of ϱ. The discrepancies of ϱ originating from diverse ligament diameters d are taken into account by a size dependent relationship $c_{size}(d)$. For a known effect on the resistivity change, it should be possible to establish a proportionality factor c_{size} which correlates ϱ for different ligament diameters and which depends on latter only. For a single ligament this is sketched in figure 2.10. If R is the measured resistance, the following relationship should be independent of the ligament size

   $$\frac{\Delta R_{d1}}{R_{0d1}} \cdot c_{size1} = \frac{\Delta R_{d2}}{R_{0d2}} \cdot c_{size2}. \tag{2.15}$$

   Finally the sample geometry and ligament size independent relationship describing the resis-

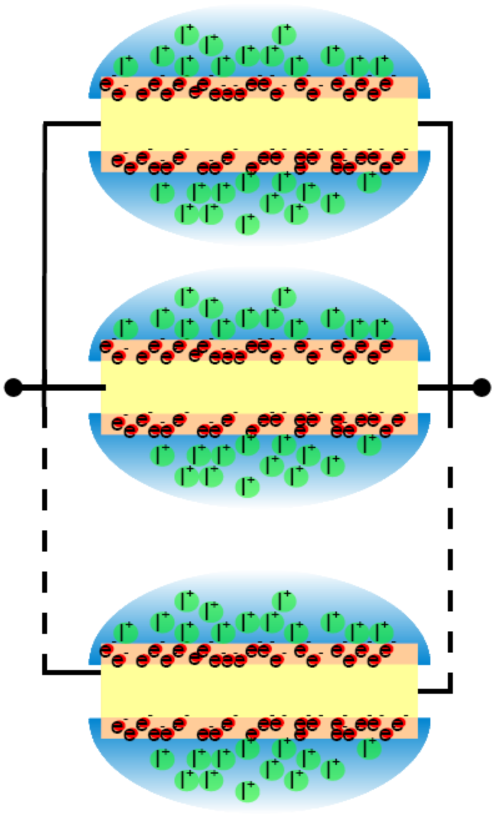

Figure 2.9: Draft of a parallel circuit comprising multiple “ligaments”. The induced charge increases with the number of ligaments because of the larger surface area.

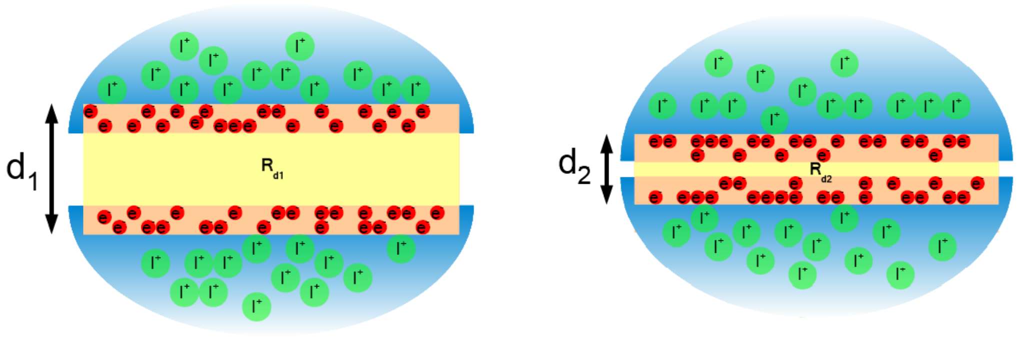

(a) ”Unchanged resistance” R_{0d1}, size effect constant c_{size1}

(b) ”Unchanged resistance” R_{0d2}, size effect constant c_{size2}

Figure 2.10: Comparison of the resistance change in dependence of ligament thickness

tance variations by means of charging is defined as follows:

$$\varrho_{size.ind.} = \frac{\Delta R}{R_0} \cdot \frac{A \cdot c_{size}}{\Delta Q} = \varrho \cdot c_{size}. \tag{2.16}$$

ΔR vs. ΔQ dependencies can only be compared by using equation 2.16, which is in fact not possible in case of different structure sizes due to the lack of knowledge in the relationship c_{size}.

It should be mentioned that choosing proper R_0 values is required to compare resistance changes by means of equation 2.16. Therefore it becomes clear, that grain boundaries and defects, which have a major impact on R_0 values, influence the measurable resistance changes too. A sample containing fewer grain boundaries should exhibit higher values of in $\varrho_{size.ind.}$.

Again, a positive size independent charging coefficient ($\varrho_{size.ind.} > 0$) means that R increases with charging, and a negative size independent charging coefficient ($\varrho_{size.ind.} < 0$) means an R decrease with charging.

Chapter 3

Experimental Procedure

This chapter describes the experimental procedure and lists used chemical components. The focus lies on the exact documentation to ensure reproducibility of all measurements and not on their basics. Reasons for the experimental settings used are given and possible variations in results and instrumental interactions are discussed.

3.1 Fabrication of nanoporous platinum samples by means of dealloying

3.1.1 Alloy fabrication

To obtain homogeneous dealloyed samples a solid solution served as starting material (see chapter 2.6), which was manufactured at the Karlsruher Institute of Technology (KIT). For the fabrication of NPG an $Ag_{75}Au_{25}$ alloy was used, and a $Cu_{75}Pt_{25}$ alloy for generating NPP. The fabrication of the NPG starting material and the NPG itself is described in the Master's thesis of Patrick Wahl [12]. The generation of the $Cu_{75}Pt_{25}$ starting alloy is described below. The master $Cu_{75}Pt_{25}$ alloy was arc melted from high purity Pt and Cu wires, subsequently rolled to $270\,\mu$m and homogenized at $700\,^{\circ}$C for one hour (vacuum annealed). After repeating the rolling and annealing, the alloy was cut into almost equal sized rectangular samples ($\approx$ 0.7 cm $\times$ 1.4 cm of about 140 mg, for subsequent dealloying at the TUGraz).

3.1.2 Dealloying process

The dealloying process, which transformed the alloys into the desired nanoporous structure, was performed in collaboration with Stefan Landgraf from the Institute of Physical and Theoretical Chemistry at the TUGraz. This section summarizes the applied assembling. 1-M

H_2SO_4 was used as electrolyte, as is done in the works of Pugh et al. [22, 23]. An 1-M $Ag/AgCl$ reference electrode was used and a tungsten rod served as counter electrode (figure 3.1). Potentials in the range of $1.5 - 1.7\,\mathrm{V}$ were to be used in the dealloying process, which was assumed to be completed after a current drop below $\approx 50\,\mu\mathrm{A}$. See chapter 4.1.2 for further details. The equipment for recording currents and voltages is summarized in figure 3.2. Eight samples were fabricated separately for this thesis, labeled $TUG - NPP_{1-8}$ below.

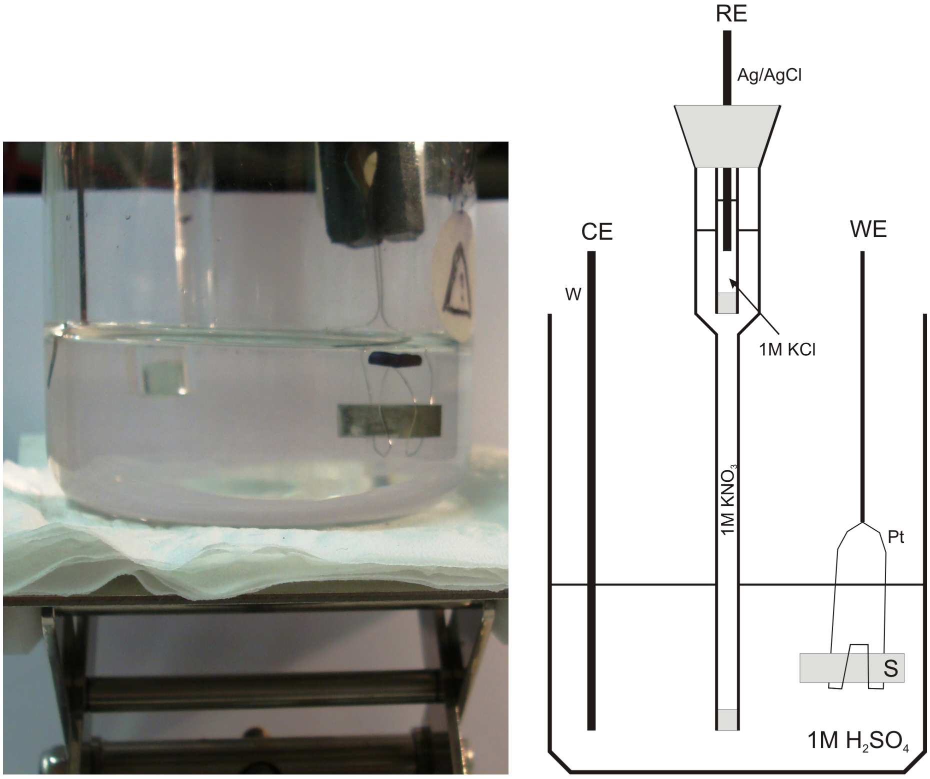

(a) Photo **(b)** Sketch [49]

Figure 3.1: Set-up used for dealloying

The sample used for the magnetic moment measurements were dealloyed at the Karlsruher Institute of Technoloy (KIT). Again, $Cu_{75}Pt_{25}$, served as starting material. At the KIT the alloy samples were dealloyed in 1-M $HClO_4$ under potentiostatic control at $900\,\mathrm{mV}$ versus a pseudo Ag/AgCl reference electrode (which was estimated to be $\approx 240\,\mathrm{mV}$ vs. SHE) and a coiled-Cu wire served as CE. The dealloying was stopped after the current deceeded a value of $10\,\mu\mathrm{A}$[1]. Three samples were investigated within this thesis, labeled $KIT - NPP_{1-4}$ in the following.

---

[1] The samples were about five times smaller than the samples fabricated at the “TU-Graz”.

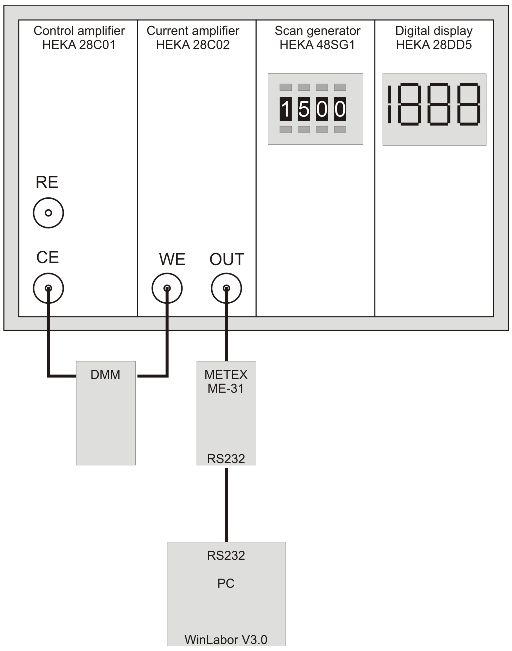

Figure 3.2: Equipment for recording currents and applying the desired potentials [49]

3.2 Preperation of nanocrystalline platinum samples

The nano-cristalline-platinum (NCP)-samples were generated as described in the Master's thesis of Martin Sagmeister [9, 2]. "Chem Pur- Platinum black" powder was used here as well and even the specimen holder was the same one build by Sagmeister. The main difference in the measurements of these NCP-samples and the NPP-samples described above is that only four wires, which is the minimum to execute four thermal sensing could be connected to the NCP-samples because of the specimen's limiting design. The importance of connecting the WE due to an additional fifth wire with the potentiostat, symmetrically placed between the sensing wires of the four thermal sensing, is described in section 3.4. Two nanocrystalline platinum samples were fabricated during this thesis, labeled $TUG - NCP_{1-2}$.

3.3 Voltammetry and chrono amperometry

This section describes the experimental procedure used to record CVs and CA curves described in chapter 2.1 and 2.2. A Petri dish served as a basin containing the electrolyte (only 1-M KOH or 1-M KCl were used as electrolyte within this work) and a saturated Ag/AgCl reference electrode ($0.199\,\mathrm{V}$ vs. SHE at $25\,^{\circ}\mathrm{C}$) was used. For the measurements on gold, a platinum rod was used as counter electrode. Gas evolution was observed at the platinum rod CE during measurements on the NPP samples. Hence the platinum rod was substituted by a carbon fabric because of its larger surface area. The latter was replaced several times before a new measurement was started. The samples were connected via a wire of the same material (platinum or gold). A *Voltalab - PGZ 100* potentiostat was used to record CVs and CA curves, subsequent evaluation was executed using *Matlab*.

3.3.1 CV and CA settings

As mentioned in chapter 2.1.2 the seep rate has to be very low to resolve the electrochemical in porous systems. This becomes obvious from figure 3.3. Depending on the samples, sweeprates of $v = 1\,\mathrm{mVs}^{-1}$ and lower had to be used to overcome kinetic limitations. Similar aspects should be considered recording CA curves (explained more accurately in [12]). Depending on the expected chemical reactions at the potentials applied, the period of time required to end up in some kind of chemical equilibrium differs. For NPP samples time scales of $10 - 70\,\mathrm{min}$ were observed. $10\,\mathrm{min}$ for simple double layer charging and more than an hour for potentials according to the oxygen and hydrogen regime (see figure 2.1).

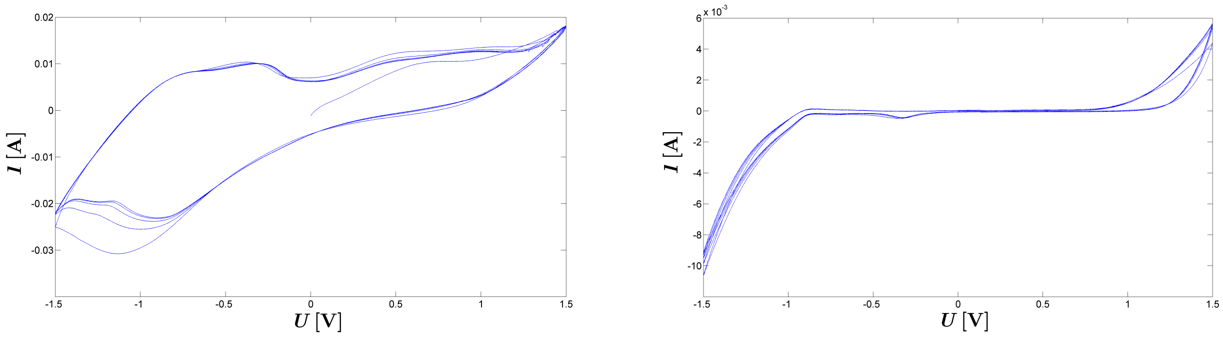

(a) Sample after a first dealloying trial

(b) Pt rod

Figure 3.3: CVs of different platinum samples recorded with the same settings: $U_l = -1500\,\mathrm{mV}$, $U_h = 1500\,\mathrm{mV}$, $v = 100\,\mathrm{mVs}^{-1}$. Because of extremely high overpotentials for the porous sample, no hydrogen or oxygen evolution was observed at such extreme $U_l - U_h$ values, in contrast to the planar platinum rod (1-M KOH electrolyte, potentials measured vs. saturated Ag/AgCl)

3.4 Resistance measurements in dependence of charging

This section shows how voltammetric methods were performed together with resistance measurements. In addition to the procedures, described in the previous subsection, resistance measurements by means of the four-point technique were performed using a *KEITHLEY - 2400 SourceMeter*. A current of $100\,\mathrm{mA}$ was supplied to guarantee accurate resistance measurements. An investigation of the optimum $I_{supplied}$-settings is given in the Master's thesis of Wahl [12]. Figure 3.4 shows the concept combining resistance and potentiostatic measurements. Five wires had to be placed on the sample, four required by the resistance measurement device and one used to connect the potentiostat to the sample. The four-terminal method, described in chapter 2.5, was applied to ensure accurate resistance measurements independent of contact resistance.

As shown in figure 3.4 the WE was positioned approximately equidistant from both sensing wires to minimize potential drops due to geometry as described in the work of Mishra et al. [50]. As mentioned above the nanoporous platinum samples fabricated by means of dealloying, are highly brittle in nature. To connect the wires to these samples a special gadget was designed. At first the five wires were guided close to the surface encased in thin glass pipes, and subsequently each wire was able to be contacted separately on the sample. The sample contacting is shown in figure 3.5b.

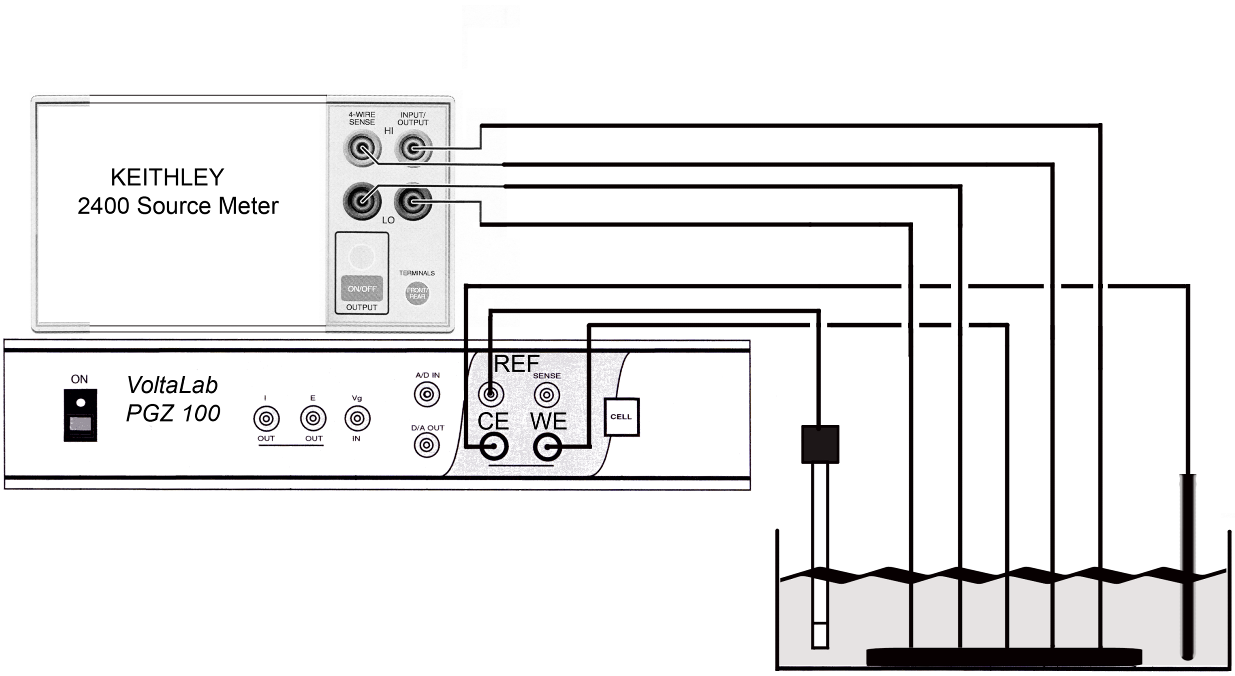

Figure 3.4: Experimental setup for resistance measurements

3.4.1 Interaction of charging and measuring signals

These two different measuring devices, connected to the same conducting sample give rise to interactions. These interactions become obvious from spikes occurring in CVs due to simultaneous (pulsed) resistance measurements as shown in figure 3.6. The size of these peaks alters with a distinct period of time, indicating some kind of measuring time interference. The current supplied by the four point method results in a voltage drop across the whole sample. This additional voltage drop changes the potential at the WE and will be compensated by the control circuit in the potentiostat trying to adjust a determined potential difference between WE and RE. The peaks in the current recorded by the potentiostat may arise because of a

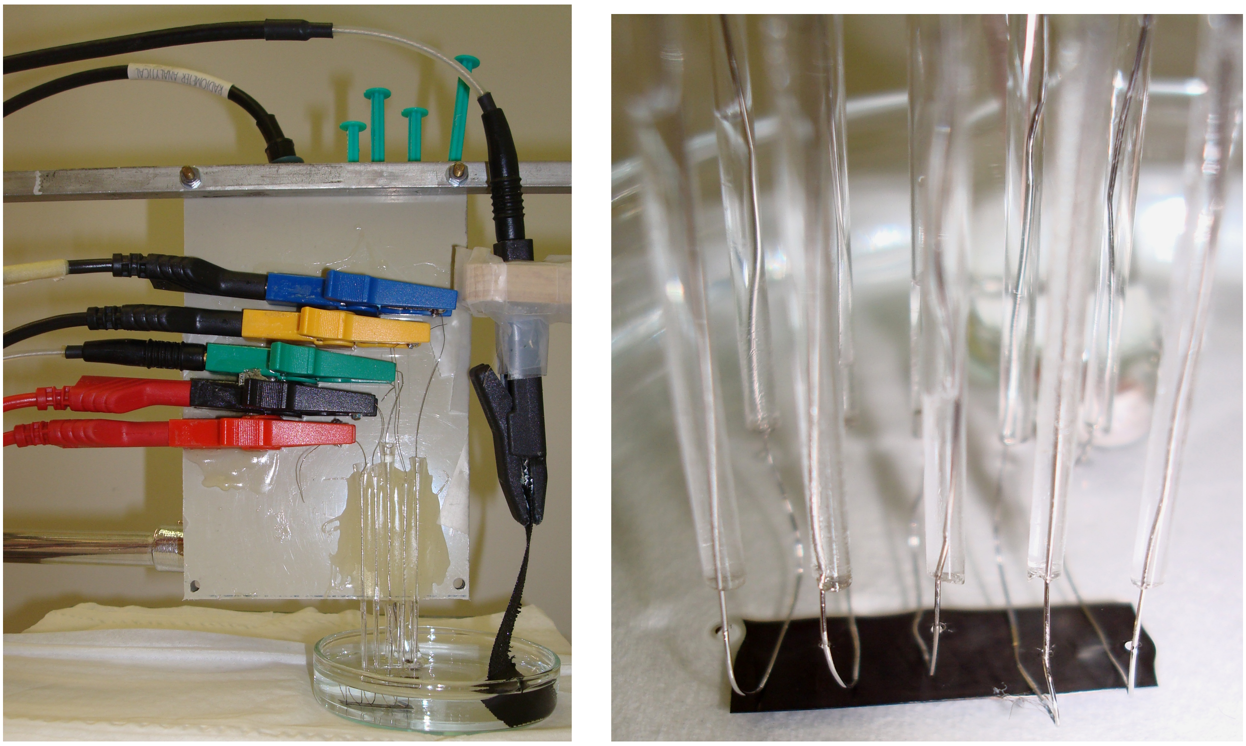

(a) Overview **(b)** Sample contacting

Figure 3.5: Photographs of the experimental set up

finite adjustment time as demonstrated in a simulation using the software *Pspice* shown in the following.

For this simulation an equivalent circuit for a potentiostat using two electrode geometry (absence of a control circuit) was imitated. Certainly this model can not reproduce a proper chemical reaction mechanism and resistance values used in this simulation may differ drastically from reality. The simulation should only explain a possible mechanism of how the measured peaks arise. The model and its results are shown in figure 3.7. In the simulation the voltage applied by *V-potentiostat* was being ramped from 0 mV to 200 mV in 40 s while current pulses of 100 mA were being supplied every 3 seconds due to *I-pulse*. As one can see, additional peaks would occur in this CV.
Another reason, also resulting from delayed balancing potential potentials due to current pulses originating from resistance measurements, may be that different potentials result in different chemical activities at the WE. For instance, a short variation of the applied potential causes additional double layer charging and decharging until the WE potential is balanced again by the control circuit. This might explain peak oscillations also observed in figure 3.6.

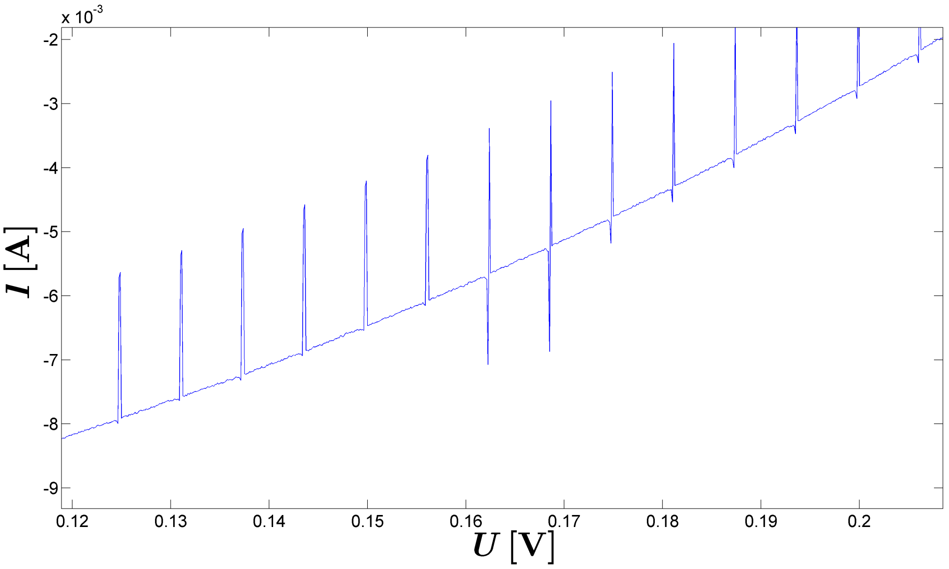

Figure 3.6: Additional peaks in a CV resulting from pulsed resistance masurements

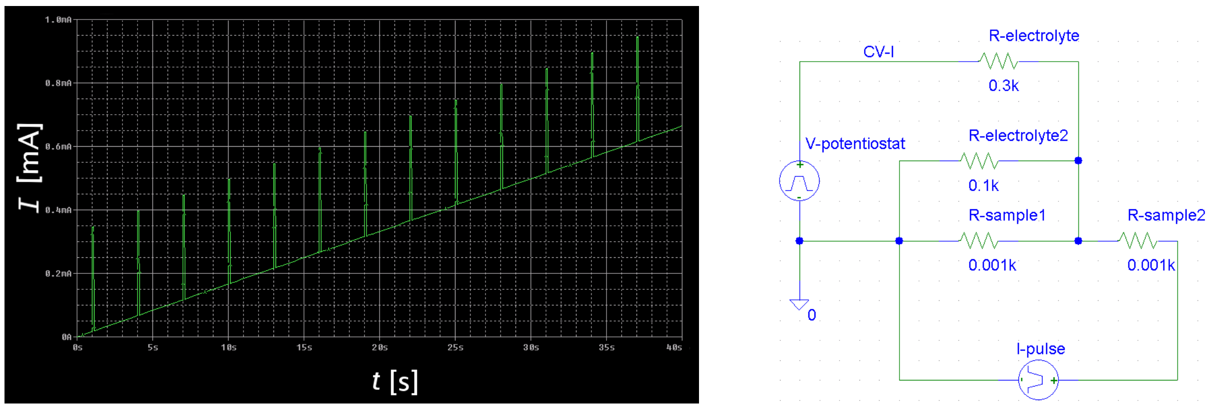
1.0mA
0.8mA
0.6mA
0.4mA
0.2mA
0A
0s
5s
10s
15s
20s
25s
30s
35s
40s
I [mA]
t [s]
CV-I
R-electrolyte
0.3k
V-potentiostat
R-electrolyte2
0.1k
R-sample1
0.001k
R-sample2
0.001k
0
I-pulse

(a) Simulation results: The used equivalent circuit results in observable peaks onto the voltammogram

(b) Equivalent circuit for a potentiostat recording a voltammogram using two electrode geometry

Figure 3.7: *Pspice* simulation exposing an opportunity for peak generation in a CV caused by simultaneous (pulsed) resistance measurements. The resistance $R - electrolyte$ surrogates the (electrolyte) resistance between the sample and the CE. Possible current drops along the sample (surrogated by $R - sample$ $1\&2$) may yield (very low) currents through the electrolyte, which is taken in to account by $R - electrolyte2$.

Chapter 4

Experimental Results

This chapter documents the experimental data obtained in this thesis. Special attention was given to evaluations of the dealloying process to ensure (and describe) the formation of nanoporosity (section 4.1.1). The resistance measurements in dependence of charging are presented in section 4.2. Initial attempts of dealloying by means of ionic liquids are presented in section 4.3 along with proposal for improvement.

4.1 Sample Characterization

The following chapter is dedicated to the sample characterization, especially to the NPP-samples because in contrast to NPP, the characteristics of NPG are well described in literature. X-Ray diffraction (XRD), CV, optical and scanning electron microscopy (SEM) were used to evidence nanoporosity and to estimate the surface area.

4.1.1 Scanning electron microscopy after dealloying

The main reason for doing electron microscopy was to prove the existence of nanoporosity. Expected structure sizes are beneath resolutions of optical microscopy and XRD yield no explicit information on porosity as described in chapter 2.6. The pictures presented in this section were made using a *LEO - 1520* field emission SEM at the Erich Schmid Institute in Leoben.

The evidence of porosity becomes obvious from figure 4.1, which shows a fragment of sample $TUG - NPP_2$, tempered twice at $200\,°C$ for $30\,min$. No porosity can be observed in identically prepared but less tempered samples. This can only be explained in terms of the smaller structure of these samples which could not be resolved by the used magnifications for the reason that nanoporous structures are reported to coarsen, but not to arise due to heat treatment. In chapter 2.6 the development of cracks along grain boundaries during the dealloying

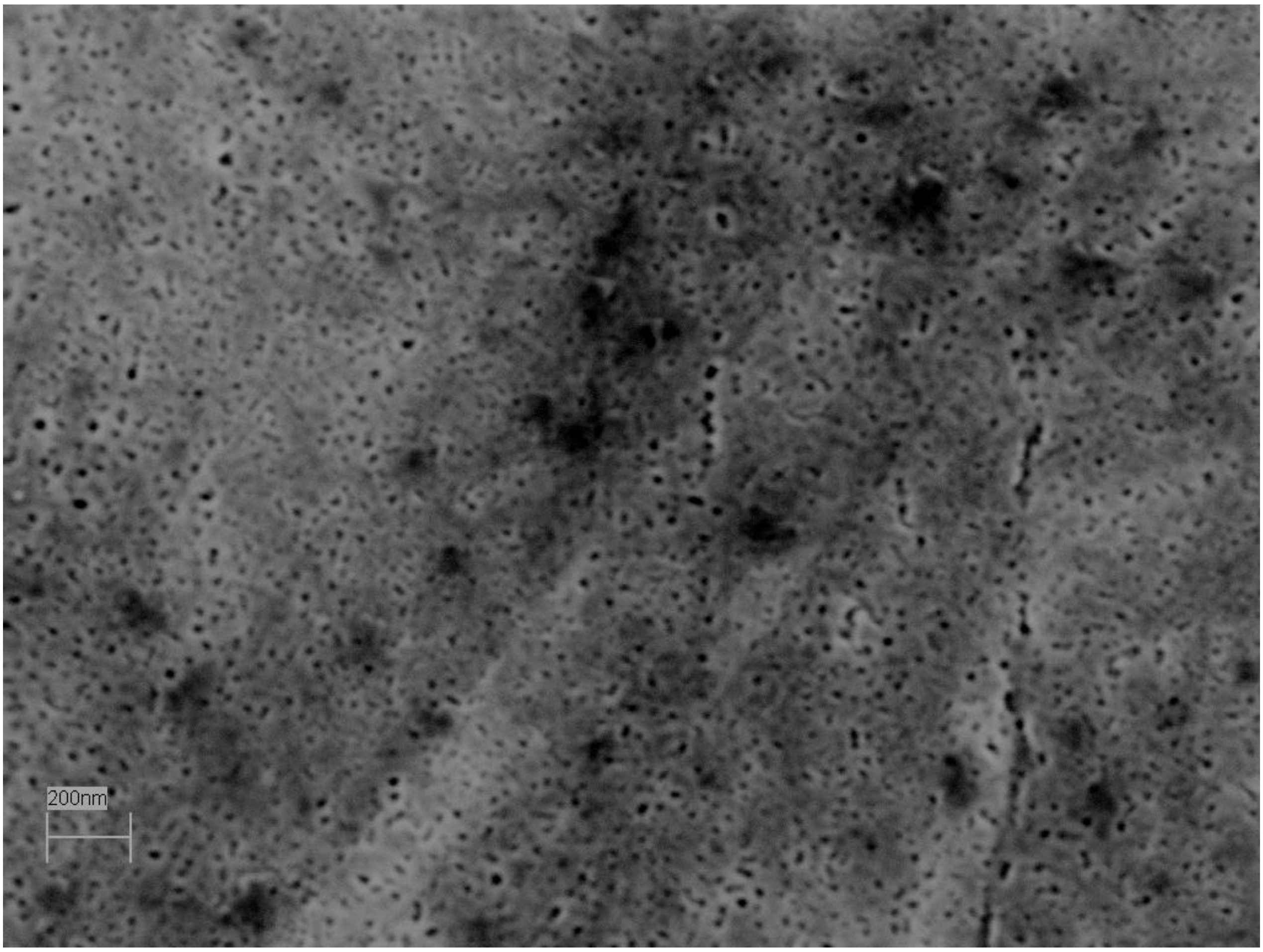

Figure 4.1: Sample $TUG-NPP_2$ fragment, tempered twice at 200 °C for 30 min. Nanoporosity is clearly visible.

process is discussed. Figure 4.2 shows such a typical crack. An accumulation of holes [1] near these cracks could be observed. Such a pit formation was described in the work of Pugh [24] for samples dealloyed slightly below the critical potential E_{crit} (see section 2.6) and ascribed to concentration fluctuations in the starting material. As described in section 2.6 dealloying at potentials below the concentration dependent E_{crit} do not result in nanoporosity. So the structural properties near the cracks may vary from the residual sample. Overviews of the cracks, which are believed to form through preferential attack of grain boundaries in the dealloying process, are given in figure 4.3.

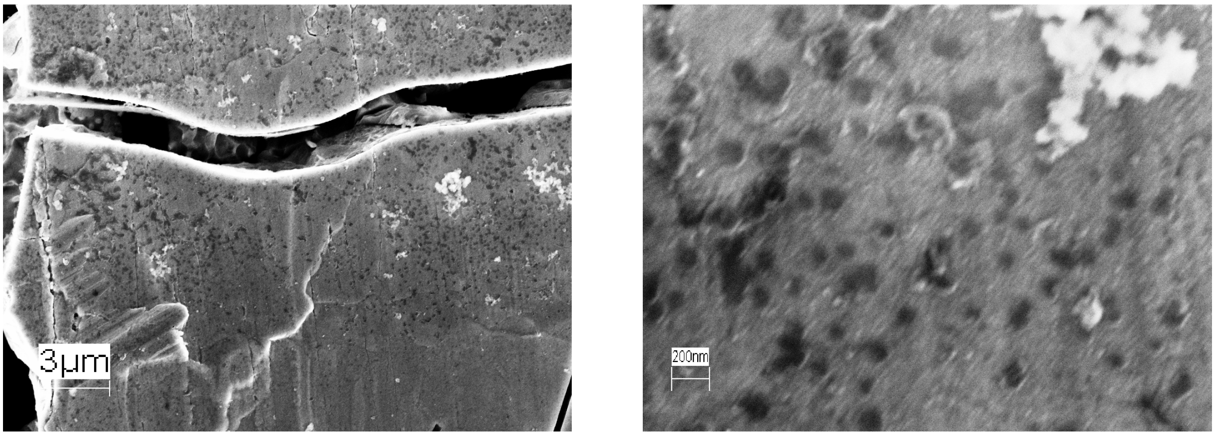

(a) Crack overview **(b)** Single holes beside the crack

Figure 4.2: SEM micrograph of a crack of sample $TUG - NPP_5$, without pre-annealing. Single holes are observed, prevalent beside the cracks.

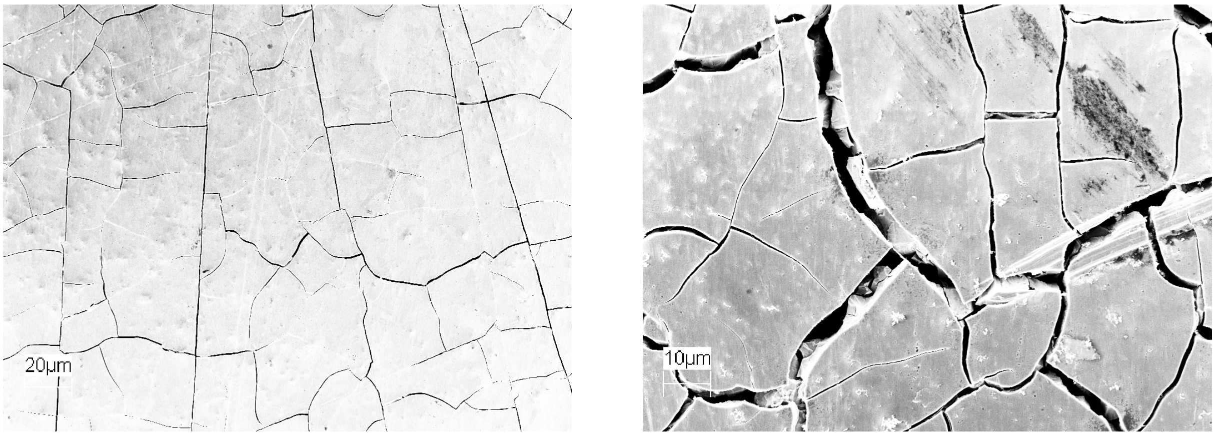

(a) Sample $TUG - NPP_2$ without pre-annealing **(b)** Sample $TUG - NPP_5$ without pre-annealing

Figure 4.3: Crack overview of two different samples

---

[1] The term hole should not be confused with the term pore. The mentioned holes have diameters far beyond that of the pores in these nanoporous materials.

4.1.2 Monitoring the dealloying process

The dealloying current time response will be the topic of this subsection. This current reveals information on reaction or transformation kinetics and dealloying progress. The shape of the dealloying current curve, $I(t)$ after applying the dealloying potential (see figure 4.4), was similar for all samples. After an immediate current decrease the maximum dealloying current was recorded followed by a continuous decrease resulting in an almost constant value which was identified as the end of the dealloying process. This time response may be described by passivation at the beginning, accounting for the current decrease. The subsequent rapid increase in current could be explained by the commencement of preferential grain boundary attack allocating more surface to the immersing electrolyte.
Under the assumption that the recorded dealloying currents result exclusively from a Cu^{++} dissolution, one could compare the charge, determined due to the dealloying current curve, to the percentage of copper dissolved. A complete oxidation of the entire copper out of 1 g $Cu_{75}Pt_{25}$ alloy should result in a charge of ≈ 2002 As. The sample $TUG - NPP_6$ presented in figure 4.4 had a weight of 142.69 mg before dealloying. Hence a complete removal of copper would require a charge of ≈ 286 As which was not obtained. Not even due to further dealloying on the next day of sample $TUG - NPP_6$ which brought additional 3 As. This deviation was an exception and for almost all other samples the expected charge (2002 As/g) was obtained. This does not mean that copper was dissoluted entirely, because at the applied high potentials additional oxygen adsorption and oxidation occurs [51]. This is indicated by the pronounced peak in the prior cathodic sweep, observed in the first CV recorded after dealloying. Figure 4.6 shows such an example.

4.1.3 In situ microscopy during dealloying

To investigate the dealloying process, microscopic pictures were taken while the dealloying process was running. The results are shown in figure 4.5. To obtain this pictures a *dnt - DigiMicro USB Camera* was placed outside the glass containing the electrolyte. Colors should not be seen as representative because the light source had to be changed a few times. Single grains are observable in figure 4.5c (maybe also in figure 4.5b), made one hour after starting the dealloying process. The preferential attack of grain boundaries, which was discussed as causing the dealloying current maximum, was possible certified by the pictures shown here because the grainy structure left to the whole of figure 4.5c may indicate the development of grain boundary grooving.

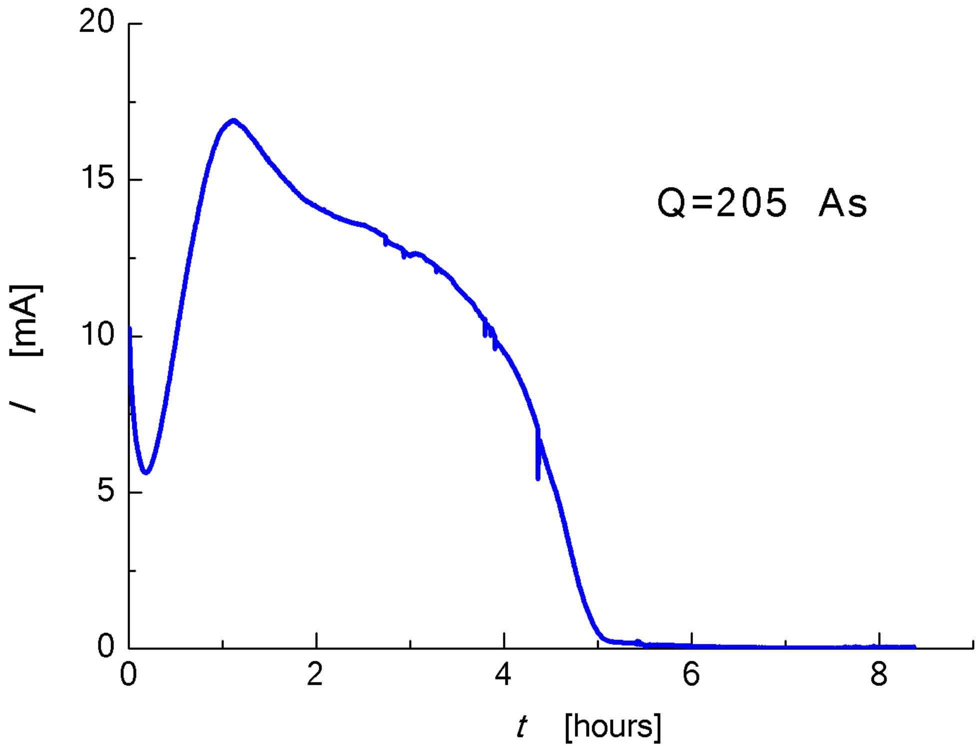

Figure 4.4: $TUG-NPP_6$ dealloying current behaviour. $U_{WE} = 1.575$ mV vs. 1-M Ag/AgCl in 0.5-M H_2SO_4.

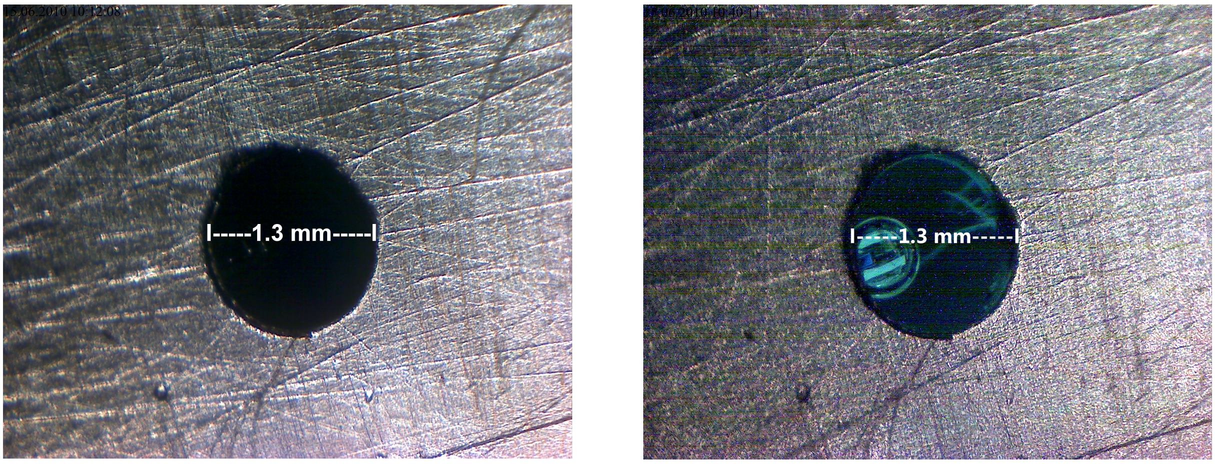
I-----1.3 mm-----I
I-----1.3 mm-----I

(a) Befor dealloying

(b) After 30 min dealloying (after dealloying current maximum)

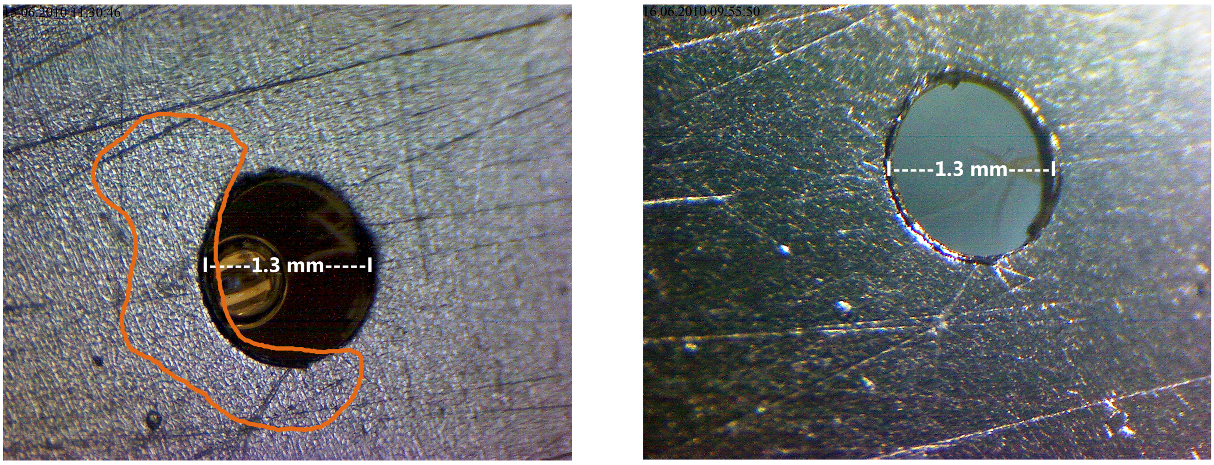
I-----1.3 mm-----I
16.06.2010 09:55:50
I-----1.3 mm-----I

(c) After 60 min. The tagged area resolves a grainy structure.

(d) After dealloying termination on the next day

Figure 4.5: *In situ* microscopy during the dealloying process

4.1.4 CV characterization of nanoporous platinum

This subsection addresses the interpretation of CVs recorded after the dealloying process. Also measured CVs approve the presence of nanoporous platinum structures because of high currents assigned to a high active surface area and characteristics which resemble those expected for pure polycrystalline platinum. Figure 4.6 shows a CV of sample $TUG - NPP_3$ cracked during the resistance measurement.

All the characteristics described in chapter 2.1.2 are reproduced at adequate potentials. It should be mentioned that the reduction peak for the first cathodic sweep at$\approx -500\,$mV looks different from the reduction behavior of the following turns. The appearance at more negative potentials indicates a different reduction process, e.g. due to a different starting surface configuration. The reduced charge, ascribed to the large area under this initial reduction peak (see figure 2.3), differs significantly from that ascribed to the first reduction peak in the subsequent cathodic sweeps, which indicates a chemically irreversible process. A quantitative analysis of these difference, in the case of the samples $KIT - NPP_3$ and $KIT - NPP_4$ (which was tempered at $120\,$°C for $30\,\mathrm{min}$ and appeared more "shiny" afterward), revealed differences in the allocated charge of 250%. This initial oxide layer, revealing different characteristics in a CV, developing during the dealloying process, will be called "primary oxide" from now on.

Conway et al. [52] investigated the formation and reduction of thicker phase, quasi-3-D oxide films, on platinum. The authors resolved two peaks in a CV assigned to oxide reduction which reveals two states in reduction. The first one(called OC1 [52]) looks similar in shape and peak position to the reduction of our primary oxide layer. The second one (called OC2 [52]), is reported to appear at more negative potentials (near or within the hydrogen atom deposition range), and was assigned to the reduction of a bulk oxide layer. This reduction peak was not observed in our CVs.The OC1 peak in the cathodic sweep was assigned to the reduction of a quasi2-d film by Conway [15]. In the same work, an increase in charge associated with OC1 is described if the potential is held constant for a long time at positive potentials (like in the dealloying process) before the cathodic sweep. The author describes a limit of oxide film formation corresponding to the "OC1-state" of $880\,\mu C\mathrm{cm}^{-2}$, corresponding to two equivalent monolayers Pt-O, represented due to "Pt-O-Pt-O" in which Pt is in the +`II` oxidation state.

The comparison of the charge associated with the reduction of our primary oxide revealed a value more than seven times larger compared to that for hydrogen atom desorption in the subsequent anodic sweep, which is expected to have a value of $210\,\mu C\mathrm{cm}^{-2}$ as described in section 2.4.2. However "Pt-O-Pt-O" can not be excluded to be our primary oxide, because of possible changes of the surface area due to its removal, which could explain this conflict.

The oxidation mechanism of platinum in H_2SO_4 presented by Jerkiewicz et al. [16] ends up in an oxide layer of the same composition (Pt_2O_2) [2]. A simplified visual presentation of the revealed platinum-oxide growth mechanism as suggested by Jerkiewicz [16] is shown in latter work in figure 7. The dependence of the position and shape of reduction peak on the timespan during which the "positive" potential was applied before is not discussed by the authors.

---

[2] The oxide layer nominations may differ from [15, 52].

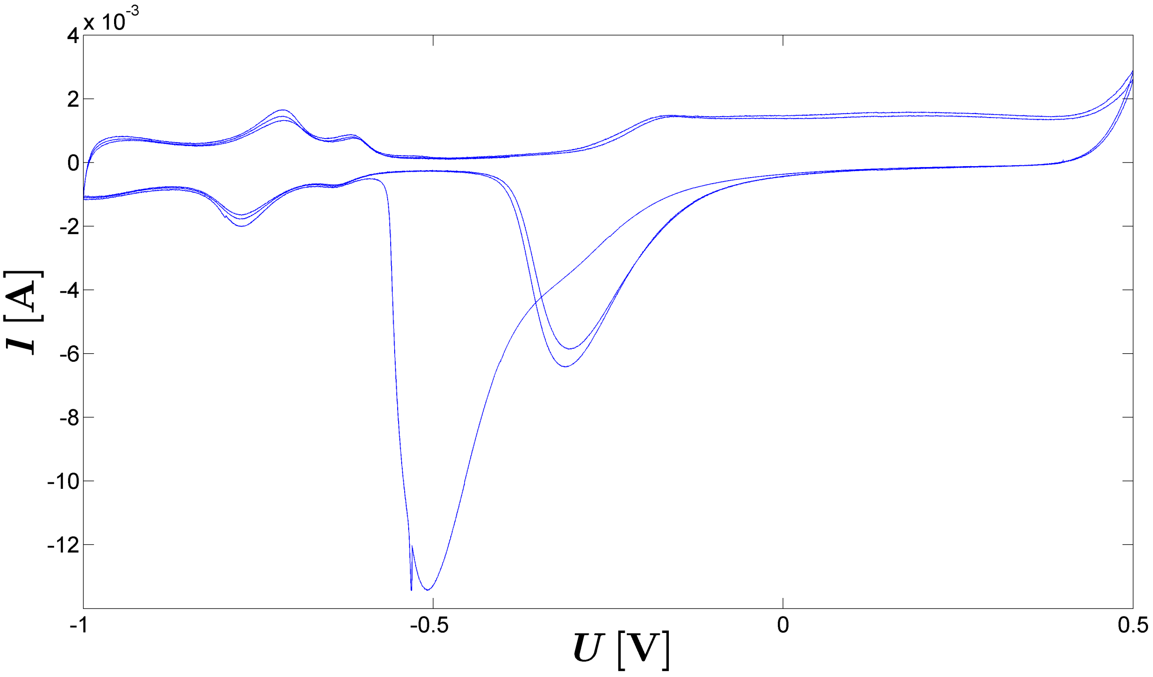

Figure 4.6: Cyclic voltammogram of a $TUG-NPP_3$ sample fragment in 1-M KOH; $v = 0.1\,\mathrm{mVs^{-1}}$, RE=saturated Ag/AgCl.

4.1.5 Electrochemical determination of the surface area

This subsection presents results of the electrochemical determination of the surface area. The two methods which were applied are described in chapter 2.4 and their utilization is described below as examples. Exact settings used may differ from sample to sample but given descriptions enable proper reproductions. The computed surface area values of the investigated samples are listed in table 4.1.

Determination of the surface area using voltammetry for a tempered $TUG-NPP_2$ fragment

How the total differential capacity τC^d was obtained using the method described in section 2.4.1 is demonstrated in figure 4.7. To avoid specific adsorptions, the CVs were performed in the double layer regime ($\approx -580 \leftrightarrow -480\,\mathrm{mV}$ vs. a saturated Ag/AgCl RE in 1-M KOH used here). CVs at different sweep rates $v = 0.5, 1, 3, 5, 7, 10\,\mathrm{mVs^{-1}}$, ten cycles each, were recorded (shown in 4.7a). For each cycle, except the first one, a few (positive) current values around the appointed potential regime's center (colored red in figure 4.7) were used to calculate a mean value. These (mean) current values were plotted versus their corresponding sweep rates to obtain the differential capacity C^d through linear regression, as one can see in figure 4.7b. To obtain the surface, the τC^d value was divided by the differential double layer capacity of $100\,\frac{\mu F}{\mathrm{cm}^2}$ reported in [14].

Determination of the surface area using charging curves for $TUG - NCP_1$

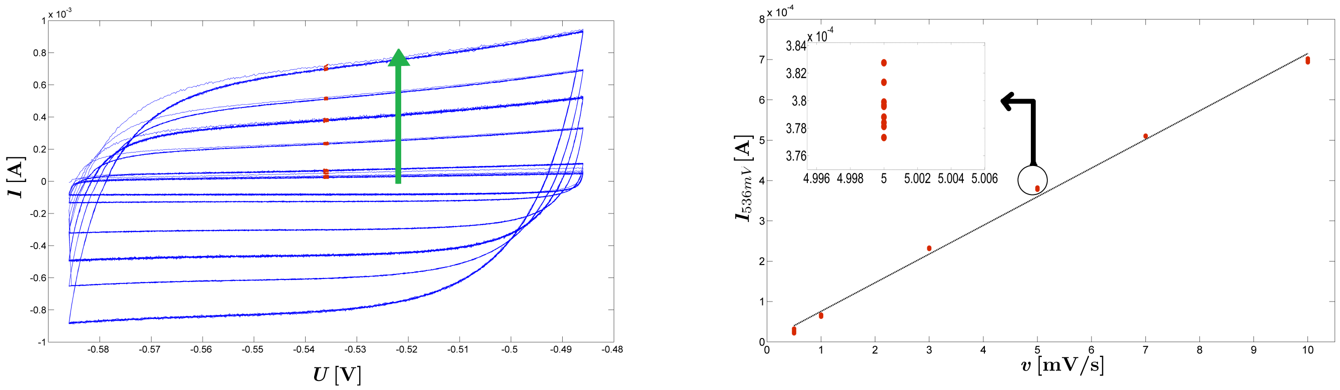

(a) CVs at different sweeprates v. The green arrow points toward of increasing sweeprates.

(b) $I(v)$-plot used to determine τC^d via linear regression. From inset the different (mean) currents values for the nine analyzed cycles using a sweeprate of $v = 5\,\mathrm{mVs}^{-1}$ can be resolved.

Figure 4.7: Differential capacity for tempered $TUG - NPP_2$ fragment. $\tau C^d_{TUG-NPP_2} = 7.104 \cdot 10^{-2}\,\mathrm{F}$.

Figure 4.8 shows the surface determination for the crystalline platinum sample $TUG - NCP_1$ using charging curves described in chapter 2.4.2. It shows how the surface was determined integrating the charge assigned to hydrogen atom desorption ($Q = \frac{1}{v} \cdot \int I(U) \cdot dU$) out of an anodic CV sweep. The integration boundaries (vertical red lines) were chosen more or less arbitrarily, because investigations on optimized experimental conditions, as described in chapter 2.4.2, were limited by experimental limitations. The lower boundary of the double layer charging regime (identified through inspection) served as the upper limit. The lower limit was placed close to the point of intersection of the CV with the dotted line (described in the following). In order to exclude double layer charging, the latter was estimated as follows. The current mean value of a regime which was believed to represent double layer charging only, had been determined (which is represented by the red dotted line) and subtracted before integrating. A charge of $4.485\,\mathrm{As}$ was computed due to this integration and the samples weight was determined to be $\approx 100\,\mathrm{mg}$. The obtained value of $21.4\,\frac{\mathrm{m}^2}{\mathrm{g}}$ for the sample $TUG - NCP_1$[3], listed in table 4.1, is in close agreement with the value of $20\,\frac{\mathrm{m}^2}{\mathrm{g}}$ presented in [9], determined by BET-measurements (see chapter 2.4) executed for equal fabricated samples.

---

[3] $A/m = \frac{\frac{4.485}{2.1}}{100} \approx 21.4\,\frac{\mathrm{m}^2}{\mathrm{g}}$, see chapter 2.4.2.

The differential capacity of the double layer regime of $TUG-NCP_1$ was computed from the measured total differential capacity by means of voltammetry and the surface area determined from the charging curves. The obtained value of $102\,\frac{\mu F}{\mathrm{cm}^2}$ coincides well with the differential capacity for double layer charging used above.

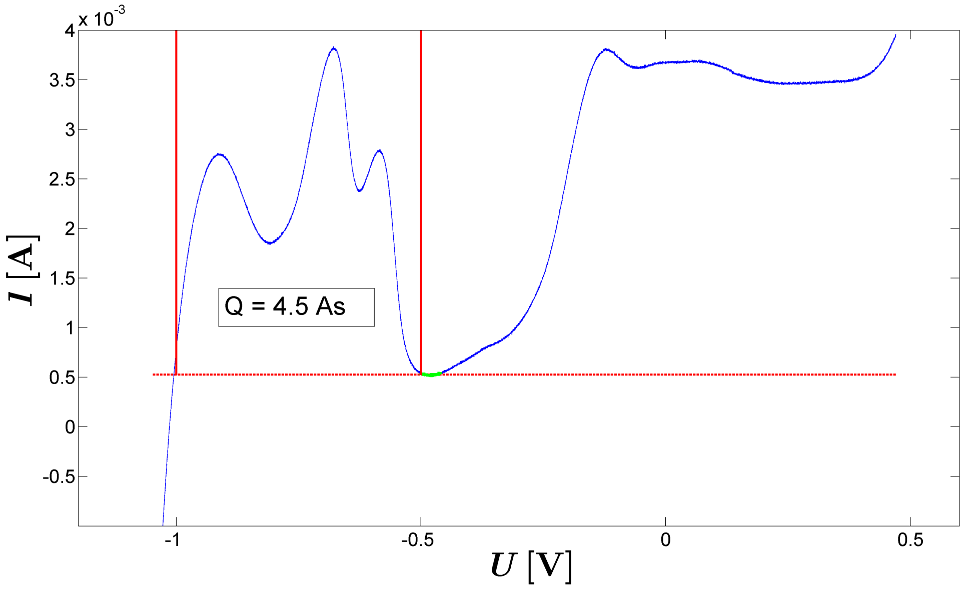

Figure 4.8: Determination of the charge, accociated with oxidation of deposited atomic hydrogen, out of an anodic sweep in a CV. The green data points were assigned to simple double layer charging and used to determine a regression to estimate and subtract double layer charging - red dotted line. Sample $TUG-NCP_1$, $v = 0.2\,\mathrm{mV}$, 1-M KOH served as electrolyte and a saturated Ag/AgCl RE was used.

Table 4.1: Surface areas

	$TUG-NPP_2$	$TUG-NPP_4$	$TUG-NCP_1$	$TUG-NCP_2$	$KIT-NPP_3$	$KIT-NPP_4$
treatment	$200\,°\mathrm{C},\ 60\,\mathrm{min}$	-	-	-	-	-
(fragment) weight $[mg]$	12	19	100	135	-	-
surf. area det. via charging curve$[m^2]$	0.07	0.75	2.14	-	0.79	0.67
surf. area det. via voltammetry$[m^2]$	-	0.98	2.18	2.29	-	-
area mass ratio $[\frac{m^2}{g}]$	5.9	39.5 / 51.6	21.4 / 21.8	17.04	-	-

4.2 Resistance measurements in dependence of electrochemical charging

This section presents the main results of this Master's thesis, the resistance variations in dependence of electrochemical charging and surface reactions. The experimental procedure is described in chapter 3.4. As already mentioned, the samples' brittleness caused technical difficulties (samples $TUG-NPP_{1,4,6,7}$ cracked even before resistance measurements were performed). The major problem was the rupture of samples applying negative potentials. The experimental procedure was changed once in the case of sample $TUG-NPP_4$ which had been preconnected by five platinum wires before the dealloying process, but this specimen also broke when applying negative potentials. A fragment of the cracked sample is shown in figure 4.9. It took a while to realize that the removal of the primary oxide layer (described in chapter 4.1.4), at potentials below $\approx -150\,\mathrm{mV}$ (vs. saturated Ag/AgCl in 1-M KOH), caused the breaking of the sample. The experimental results are presented in chronological order.

The measurements presented in this section were recorded in 1-M KOH when not described otherwise. All the potential data were recorded using a saturated Ag/AgCl referenz electrode ($U \equiv U$ vs. saturated Ag/AgCl). For the calculation of relative resistance changes of the $TUG-NPP$ samples, $(R-R_0)/R_0 = \Delta R/R_0$, R_0 was always chosen as the initial resistance value before the beginning of chemical treatments, i.e first recordings using the potentiostat. The origin of the additional (sharp) peaks in the recorded CVs is discussed in chapter 3.4.1. The charge was always calculated by integrating the current recorded by the potentiostat $Q(t) = \int_{t_0}^{t} I dt$. Here t_0 labels the time at which a sequence (CVs, CAs...) was started. Differences in the starting potential U_{start} and the circumstance that net charging was often observed to be non zero during single cycles of a CV, (e.g. due to cumulative charging during successive cycling) does not allow a quantitative comparison of absolute charge values.

A list of measured resistance changes and basic information of its charging behavior is presented in table 4.2. The subsequent subsections present a more comprehensive description of obtained results for each sample, after a short summary of expected chemical processes in the applied potential ranges, chemical pre-treatment and general sample features.

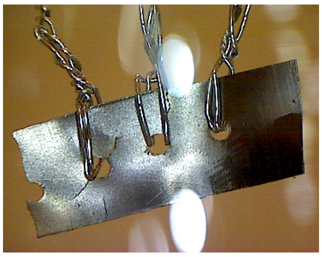

Figure 4.9: Sample cracked during the measurement

Table 4.2: Summary of results in resistance variations on nanostructured platinum samples in dependence of charging

Sample $TUG-NPP_2$

<table>
<tr><th>$\frac{\Delta R}{R_0}$</th><th>figure</th><th>$\frac{\Delta R}{R_0 \cdot \Delta Q}$</th><th>figure(s)</th><th>charging</th><th>potentials</th></tr>
<tr><td>14 %</td><td>4.11a</td><td></td><td></td><td>chemisorption*</td><td>$U_l = -500\,\mathrm{mV}; U_h = 300\,\mathrm{mV}; v = 5\,\mathrm{mVs}^{-1}$</td></tr>
<tr><td colspan="6">• Reversible changes of $\frac{\Delta R}{R_0} = 14\,\frac{\%}{\mathrm{As}}$ were obtained in case of the first CV
• negative charging led to a decrease in resistance in case of the first CV</td></tr>
<tr><td>40 %</td><td>4.12</td><td>$1.29\,\frac{\%}{\mathrm{As}}$</td><td>4.12</td><td>chemisorption</td><td>$U_{start} = 300\,\mathrm{mV}; U_h = -486\,\mathrm{mV}; U_l = -586\,\mathrm{mV}; v = 1\,\mathrm{mVs}^{-1}$</td></tr>
<tr><td colspan="6">• The drastic decrease in resistance of $\frac{\Delta R}{R_0} = 40\,\frac{\%}{\mathrm{As}}$ resulted from reduction of the primary oxide</td></tr>
</table>

Sample $TUG-NPP_3$

<table>
<tr><th>$\frac{\Delta R}{R_0}$</th><th>figure</th><th>$\frac{\Delta R}{R_0 \cdot \Delta Q}$</th><th>figure</th><th>charging</th><th>potentials</th></tr>
<tr><td>10 %</td><td>4.11b</td><td></td><td></td><td>chemisorption*</td><td>$U_l = -500\,\mathrm{mV}; U_h = 300\,\mathrm{mV}; v = 5\,\mathrm{mVs}^{-1}$</td></tr>
<tr><td colspan="6">• Reversible changes of $\frac{\Delta R}{R_0} = 10\,\frac{\%}{\mathrm{As}}$ were obtained in case of the first CV
• negative charging led to a decrease in resistance in case of the first CV</td></tr>
<tr><td>30 %</td><td>4.13</td><td>$1.57\,\frac{\%}{\mathrm{As}}$</td><td>4.13b</td><td>chemisorption</td><td>$CA : U_{prior} = 300\,\mathrm{mV}, U = 586\,\mathrm{mV}$</td></tr>
<tr><td colspan="6">• The drastic decrease in resistance of $\frac{\Delta R}{R_0} = 30\,\frac{\%}{\mathrm{As}}$ resulted from reduction of the primary oxide</td></tr>
</table>

Sample $TUG-NPP_5$

<table>
<tr><th>$\frac{\Delta R}{R_0}$</th><th>figure</th><th>$\frac{\Delta R}{R_0 \cdot \Delta Q}$</th><th>figure</th><th>charging</th><th>potentials</th></tr>
<tr><td>8 %</td><td>4.14, (4^{th} cycle)</td><td>$16.07\,\frac{\%}{\mathrm{As}}\star$</td><td>4.15b</td><td>pseudo cap.</td><td>$U_l = 0\,\mathrm{mV}; U_h = 400\,\mathrm{mV}; v = 5\,\mathrm{mVs}^{-1}$</td></tr>
<tr><td colspan="6">•$\frac{\Delta R}{R_0}$ increases with initial cycling
• For each cycle $\frac{\Delta R}{R_0}$ and hence R reaches its minimum value with maximum negative charging
• With further cycling a relative minimum of $\frac{\Delta R}{R_0}$ occurs for positive charging. The R-minimum for positive charging increases and that for negative charging decreases upon further cycling.</td></tr>
<tr><td>3 %</td><td>4.16</td><td>altering</td><td>4.16</td><td>pseudo cap.</td><td>$U_l = 0\,\mathrm{mV}; U_h = 400\,\mathrm{mV}; v = 5\,\mathrm{mVs}^{-1}$</td></tr>
<tr><td colspan="6">• After numerous cycles (20 in this CV), the $\Delta R(Q)$ dependence inversed in comparison to initial cycling
• $\frac{\Delta R}{R_0 \cdot \Delta Q} = 3\,\%$ with minimum for positive charging, i.e. e^--deficiency</td></tr>
<tr><td>30 %</td><td>4.17a</td><td>$15.12\,\frac{\%}{\mathrm{As}}\star$</td><td>4.17</td><td>pseudo cap.</td><td>$U_l = -150 - 0\,\mathrm{mV}; U_h = 400\,\mathrm{mV}; v = 5\,\mathrm{mVs}^{-1}$</td></tr>
<tr><td colspan="6">• Similar to figures 4.14 and 4.16, the initial R minimum with maximum negative charging decreases upon further cycling and becomes dominant with positive charging</td></tr>
</table>

Sample $TUG - NPP_8$

$\frac{\Delta R}{R_0}$	**figure**	$\frac{\Delta R}{R_0 \cdot \Delta Q}$	**figure**	**charging**	**potentials**
$4\,\%$	4.18	altering	4.18	pseudo cap.	$U_l = 0\,\mathrm{mV}; U_h = 450\,\mathrm{mV}; v = 1\,\mathrm{mVs}^{-1}$
• Characteristic of this sample is the appearance of a faint local minimum for maximum negative voltage, i.e, negative charging • Predominately R **decreased** with **positive** charging					
$1 - 4\,\%$	4.18	altering	4.18	pseudo cap.	$U_l = 0\,\mathrm{mV}; U_h = 100 - 450\,\mathrm{mV}; v = 1\,\mathrm{mVs}^{-1}$
• $\frac{\Delta R}{R_0 \cdot \Delta Q}$ changed the sign upon extending the applied potentials ranges from $\frac{\Delta R}{R_0} = 1\,\%; \frac{\Delta R}{R_0 \cdot \Delta Q}$ =positive for $U_h = 100$, to $\frac{\Delta R}{R_0} = 4\,\%; \frac{\Delta R}{R_0 \cdot \Delta Q}$ =predominantely negative for $U_h = 450$					

Sample $TUG - NCP_1$

$\frac{\Delta R}{R_0}$	**figure**	$\frac{\Delta R}{R_0 \cdot \Delta Q}$	**figure**	**charging**	**potentials**
$20\,\%$	4.22	$1.4\,\frac{\%}{\mathrm{As}}$	4.23	chemisorption	$U_l = -1030\,\mathrm{mV}; U_h = 440\,\mathrm{mV}; v = 0.2\,\mathrm{mVs}^{-1}$
• In the wide investigated potential regime, the general resistance behavior is in agreement with the measurements of Sagmeister [9] • $\frac{\Delta R}{R_0 \cdot \Delta Q}$ was almost constant in the investigated potential regime					

Sample $TUG - NCP_2$

ΔR	**figure**	$\frac{\Delta R}{R_0 \cdot \Delta Q}$	**figure**	**charging**	**potentials**
$0.5\,m\Omega$	4.24	$1.35\,\frac{\%}{\mathrm{As}}$	4.25	pseudo cap.	CAs; steps of $50\,\mathrm{mV}$, for 10 min., between $0 - 450\,\mathrm{mV}$
• In contrast to the NPP-samples, the sign of $\frac{\Delta R}{R_0 \cdot \Delta Q}$ remained positive during pseudo capacitive charging					

$*$...Sweep rate v was to fast to reach equilibrium conditions.

$\star$...Not in the whole investigated potential window. Even its sign changed.

4.2.1 Samples $TUG-NPP_2$ and $TUG-NPP_3$

After the dealloying process the primary oxide is still present on the sample surface (see subsection 4.1.4). The oxide was reduced at potentials below $\approx -150\,\mathrm{mV}$*. The CVs presented here were all recorded using fast sweep rates. Because of this, the CVs do not show characteristic peaks and chemical processes overlap. Both samples cracked upon applying low potentials.*

The first sequence was the same one for both samples, and results are shown in the figures 4.10-4.11. The CVs look very similar and the observed resistance changes, $10-14\%$, are of similar magnitude. As already mentioned, applied negative potentials initiated the reduction of the primary oxide layer. Hence the sequences analyzed in figures 4.12-4.13, resulted in complete reduction of the primary oxide which ended up in the destruction of

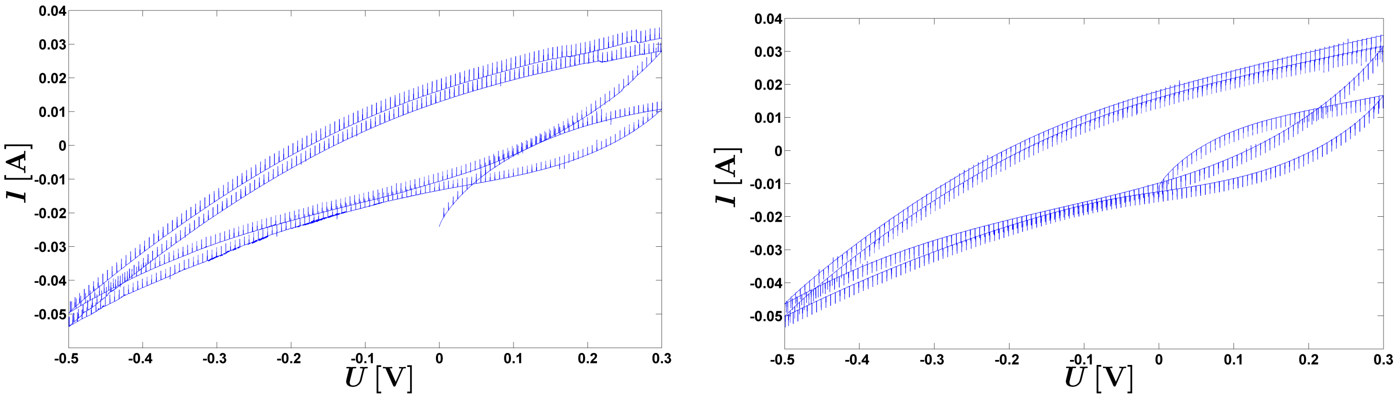

(a) Sample $TUG-NPP_2$ **(b)** Sample $TUG-NPP_3$

Figure 4.10: First CV of the samples $TUG-NPP_{2-3}$, both recorded using equal settings: $U_{start}=0\,\mathrm{mV}$, $U_l=-500\,\mathrm{mV}$, $U_h=300$, $v=5\,\mathrm{mVs^{-1}}$.

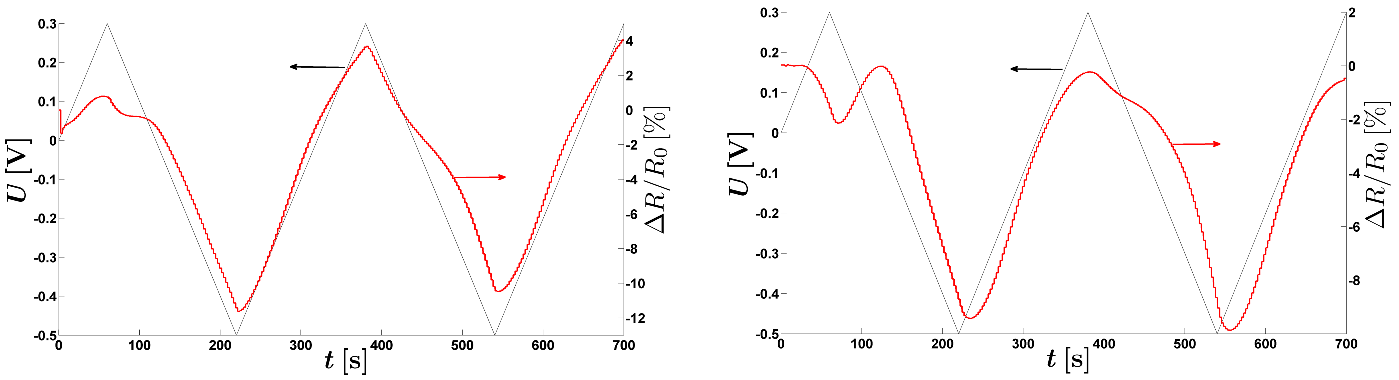

(a) Sample $TUG-NPP_2$, $R_0=1.965\ \Omega$, $\frac{\Delta R}{R_0}\approx 14\ \%$ **(b)** Sample $TUG-NPP_3$, $R_0=1.827\ \Omega$, $\frac{\Delta R}{R_0}\approx 10\ \%$

Figure 4.11: Resistance changes recorded during the first CV (see caption of figure 4.10

the sample. In case of sample $TUG-NPP_2$ the first CV, which stopped at $300\,\mathrm{mV}$, was followed by a CV starting at this value $U_{start}=300\,\mathrm{mV}$ sweeping to $U_l=-586\,\mathrm{mV}$ and cycling between this potential and $U_h=-486\,\mathrm{mV}$. The decrease in resistance due to the primary oxide removal during the described CV sequence is analyzed in figure 4.12. In the case of sample $TUG-NPP_3$, the primary oxide was removed similar. After the first CV was finished, the negative potential $U=-586\,\mathrm{mV}$ was applied immediately. The decrease in resistance during the described CA sequence is analyzed in figure 4.13 [4]. Both investigated $\frac{\Delta R}{R_0\cdot\Delta Q}$ values (1.57 and $1.29\,\frac{\%}{\mathrm{As}}$) are in acceptable agreement. In figure 4.13b the slope of section `I` was used because charging in section `III` is predominately capacitive, which is discussed in chapter 5.1 to induce higher variations in resistance. The plateau in section `II` may be assigned to crack initiations.

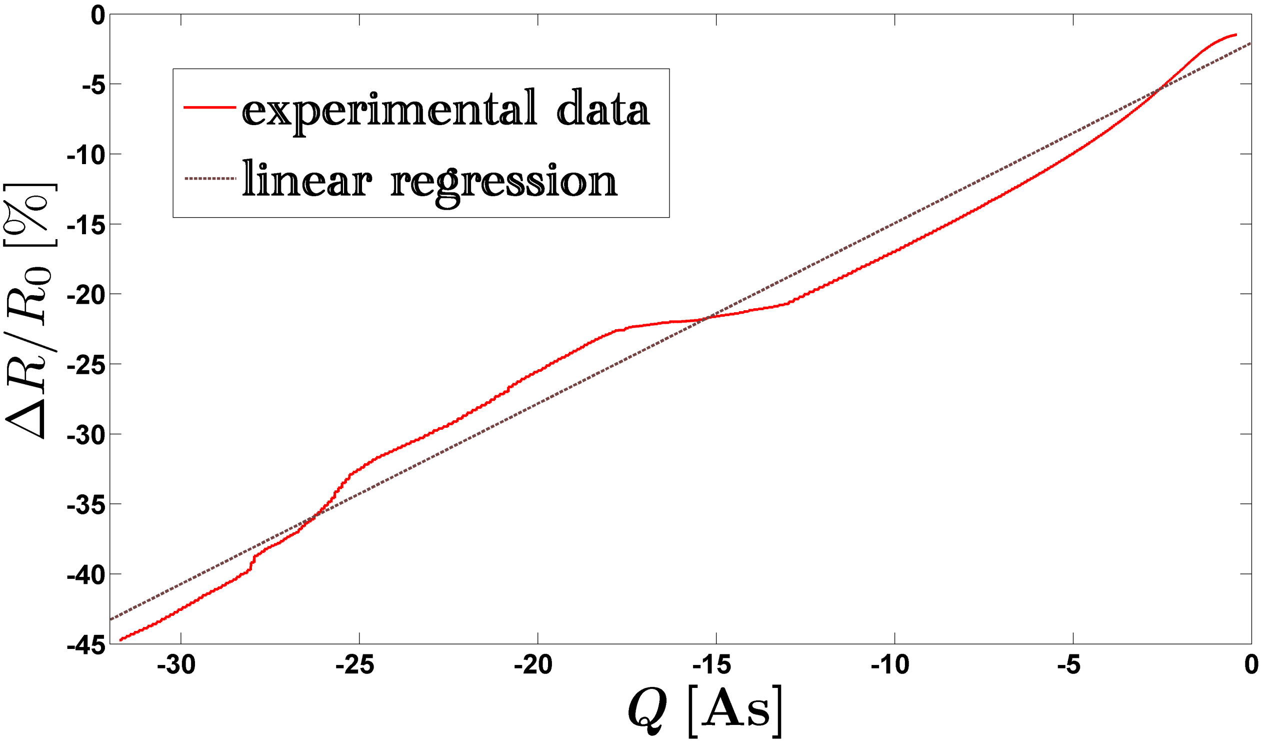

Figure 4.12: Sample $TUG-NPP_2$, $R_0=1.965\ \Omega$: Relation between charge and resistance during a CV, starting from $U_{start}=300\,\mathrm{mV}$ reaching the potentials $U_l=-586\,\mathrm{mV}$ and $U_h=-486\,\mathrm{mV}$ for successive cycling ($v=1\,\mathrm{mVs^{-1}}$) .The oxide layer is reduced during this sequence. The slope of the fit is $\approx 1.287\,\frac{\%}{\mathrm{As}}$.

4.2.2 Sample $TUG-NPP_5$

For the sample $TUG-NPP_5$ *the initial situation was the same as that described in the previous subsection. Reduction of the oxide layer, arising during the dealloying process, was now exposed to result in sample cracking. To avoid this, operating potentials were limited to*

---

[4] An immediate drop in resistance ($0\rightarrow-10\ \%$) in the first second of the CA is not apparent from this figure

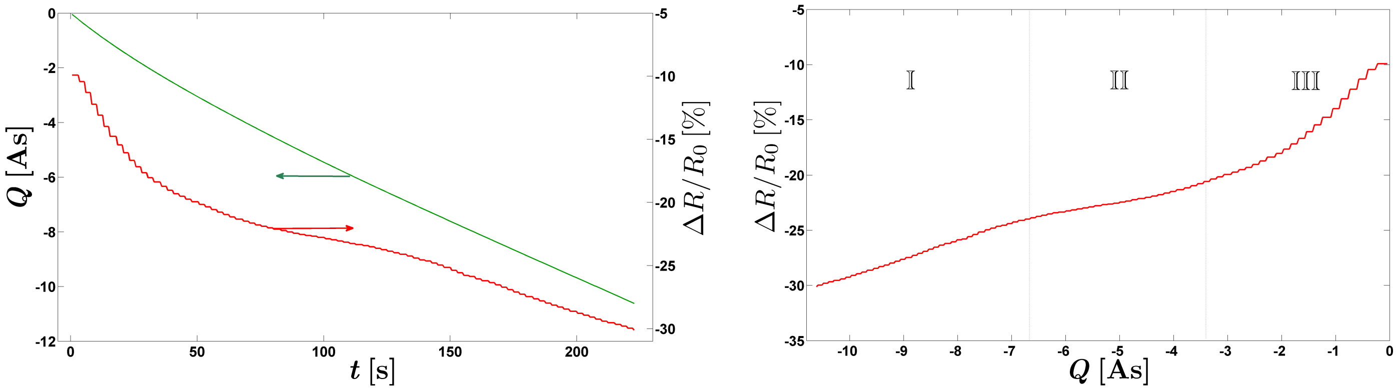

(a) Time behavior of charging and resistance

(b) Relation between charge and resistance. Three different behaviors are observed. The slope in section I is $\approx 1.5663\,\frac{\%}{\text{As}}$

Figure 4.13: Sample $TUG-NPP_3$, $R_0 = 1.827\,\Omega$: CA at a potential of $-586\,$mV. At this potential reduction of the primary oxide layer occurs.

“positive” potentials ($> -100\,$mV) henceforward.

Analysis of the first CV of $TUG-NPP_5$, applying potentials leading only to pseudo capacitive charging, is shown in the figures 4.14-4.15. The figures reveal a sign inversion in the resistance which is in contrast to the behavior of charging. No peaks can be resolved in the CV assigned to electrochemical processes at the surface that might account for a negative charging coefficient. Successive measurements were designed for the investigation and verification of this remarkable behavior.

The subsequent sequence, using the same settings as the first one, revealed the same behavior as shown in the figures 4.16. The resistance changes ended up in additional (now absolute) minimum values at the highest potential values U_h of the CV, but the (now local) minimum values coincide with the charge minimum as expected. The remarkable fact that the described additional local minimum became the major effect during continuous cycling (compare figure 4.15 to 4.16). This evolution in time was reproducible as documented by figure B.2. Figure 4.17 shows further analysis of the latter figure. After the first twelve cycles, U_l was successively decreased in the last four cycles till $-150\,$mV. ϱ was observed to remain almost constant in the potential range of $-150 \leftrightarrow 200\,$mV.

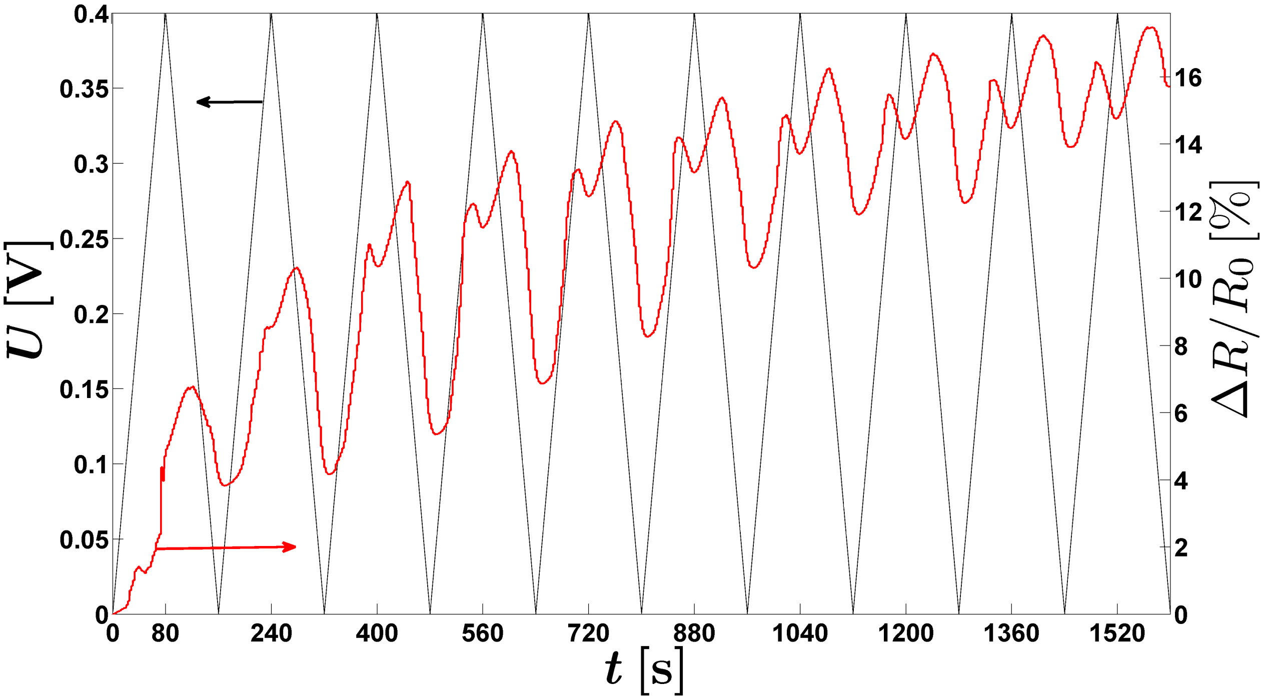

(a) Resistance and voltage time dependence

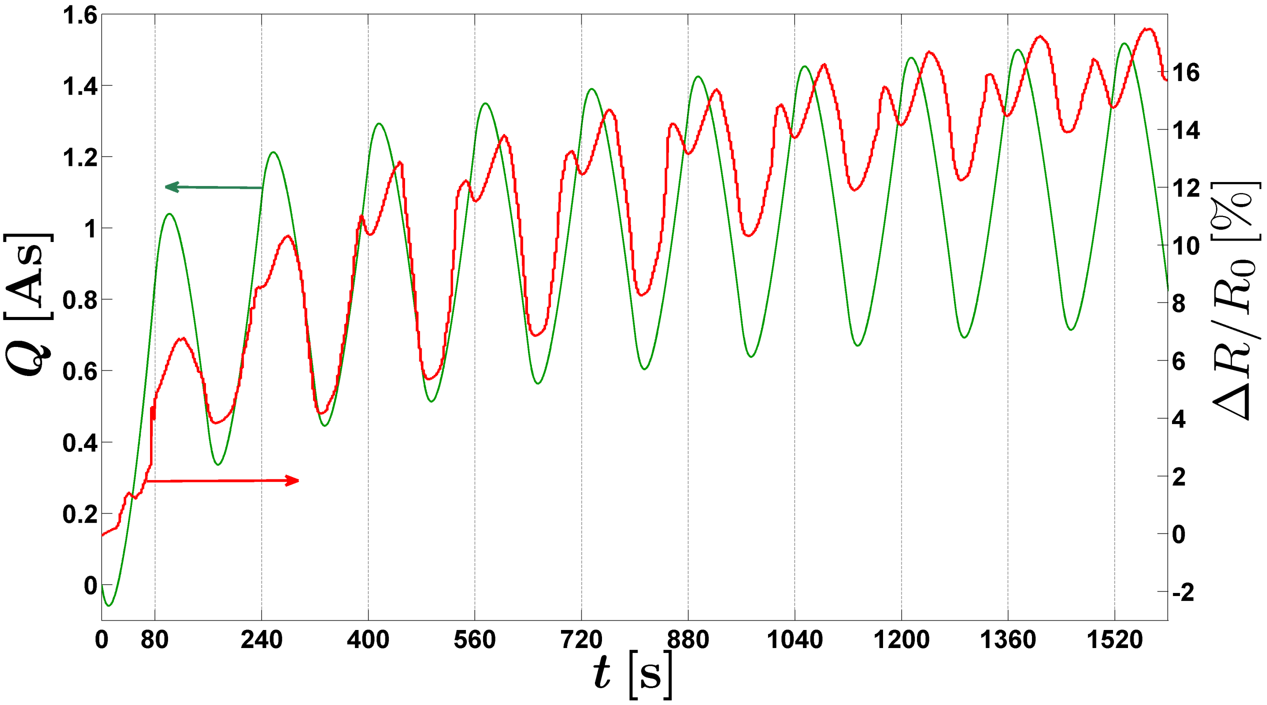

(b) Resistance and charging time dependence. The vertical lines mark the times at which the potential reached its maximum value ($U_h = 400\,\mathrm{mV}$).

Figure 4.14: Sample $TUG - NPP_5$, $R_0 = 1.339\ \Omega$. Evaluation of the resistance time behavior during the first CV of sample $TUG - NPP_5$, CV details and further evaluation are shown in figure 4.15a.

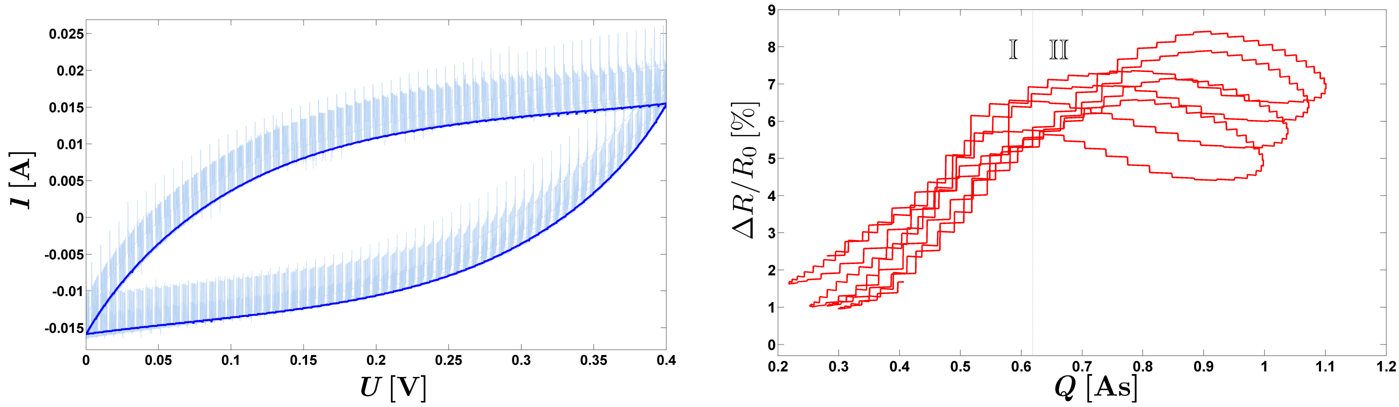

(a) CV($U_{start} = U_l = 0\,\mathrm{mV}$ and $U_h = 400\,\mathrm{mV}$, $v = 5\,\mathrm{mVs^{-1}}$). The dark blue line designates the 7^{th} cycle without the additional peaks resulting from the resistance measurement, see chapter 3.4.1. No peak could be resolved, but integration of the CV lead to a positive total charge, green line in figure 4.14.

(b) Correlation of the resistance changes with the charge for the last four cycles of the first CV. The drift of the charge and resistance with time, was subtracted for this plot, using linear regression. The slope in section I is $\approx 16.07\,\frac{\%}{\mathrm{As}}$.

Figure 4.15: Sample $TUG - NPP_5$, further analysis of figure 4.14

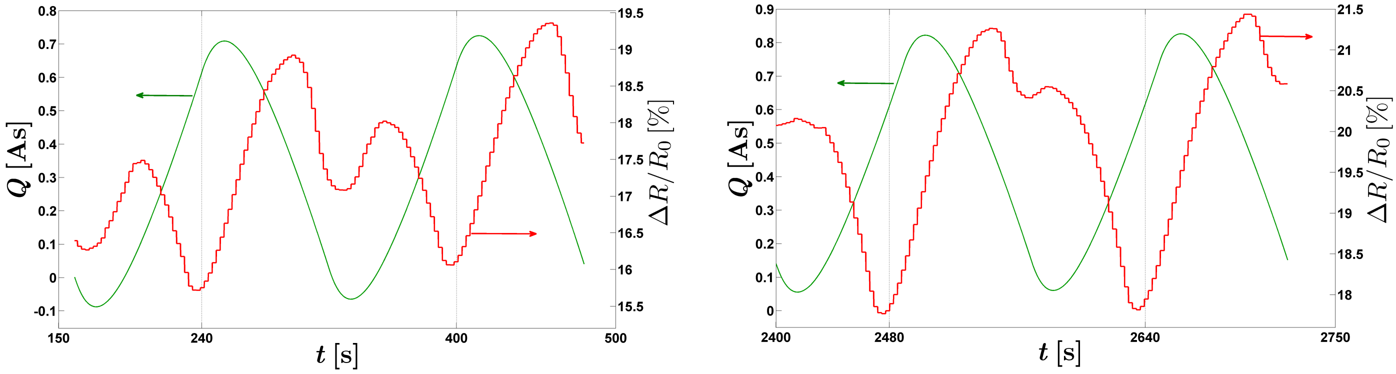

(a) 2^{nd} and 3^{rd} cycle

(b) 16^{th} and 17^{th} cycle

Figure 4.16: Sample $TUG - NPP_5$, $R_0 = 1.339\ \Omega$. Extract from the second CV, 20 cycles recorded with the same settings as before, see caption in figure 4.15a. The absolute changes in resistance reduced to $\frac{\Delta R}{R_0} \approx 3\%$. The complete plot is shown in the appendix figure B.1.

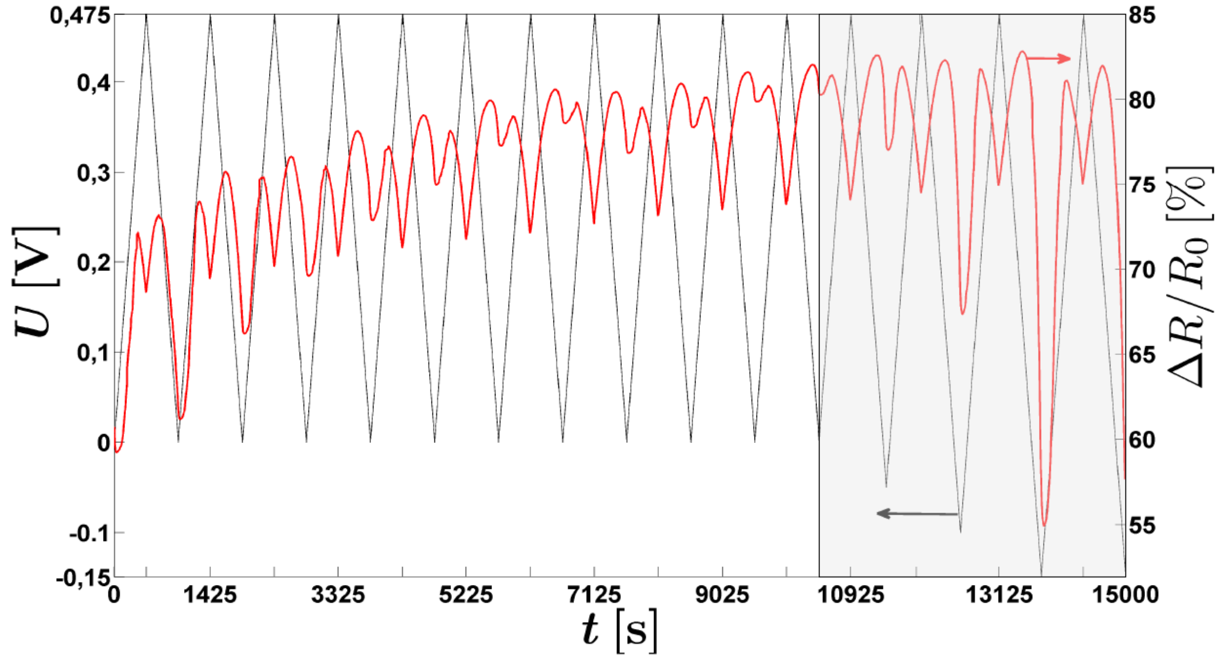

(a) Resistance and voltage time dependence. The marked section was used for the analyses shown in figure 4.17b.

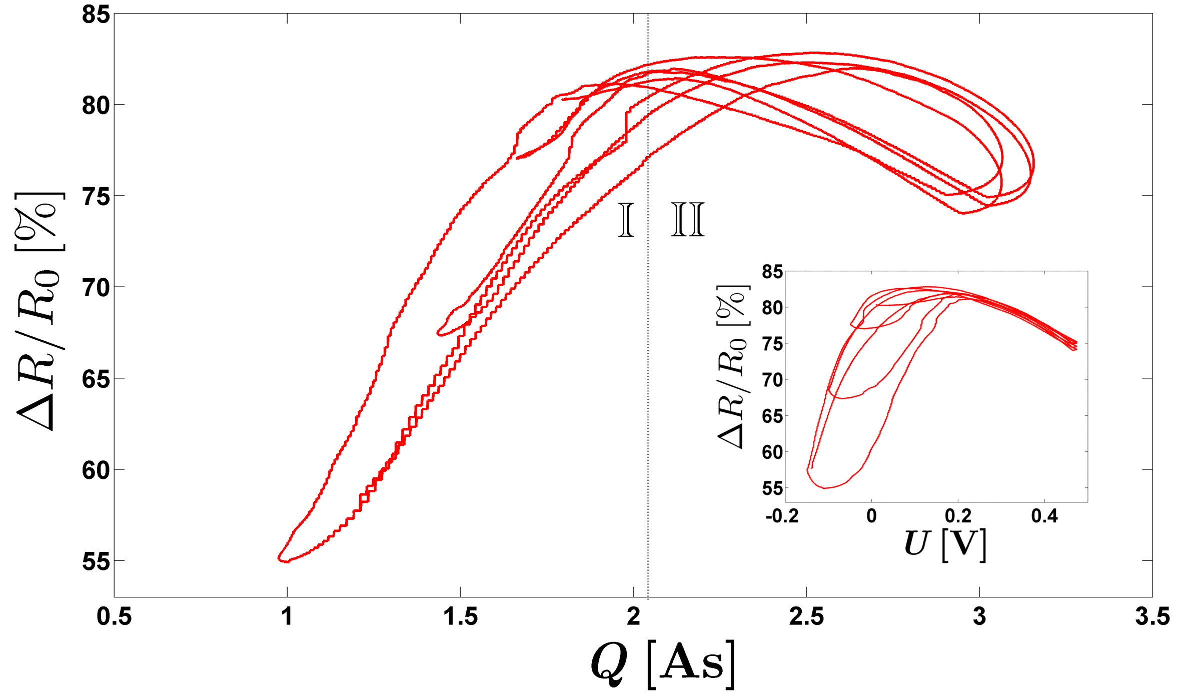

(b) Resistance dependence with charging. The slope in section `I` is $\approx 15.12\,\frac{\%}{\text{As}}$. The linear correlation between the resistance and the potential in section `II` ($\approx 0.20 - 0.45\,\text{V}$) becomes obvious from the insert.

Figure 4.17: $TUG{-}NPP_5$, $R_0 = 1.339\,\Omega$, CV with decreasing U_l value ($U_h = 475\,\text{mV}$, $v = 1\,\text{mVs}^{-1}$ and $U_l = 0,\ -50,\ -100,\ -150\,\text{mV}$). The charge time dependence during this CV is shown in the appendix, figure B.2. Before the generation of plot **b** the constant drift in charge (see figure B.2 in the appendix) was subtracted, using the maximum charge values of the last four cycles to determine a linear regression.

4.2.3 Sample $TUG - NPP_8$

Also for the sample $TUG - NPP_8$ potential settings were chosen that avoided the attack (desorption) of the primary oxide layer. So again, one has to keep in mind the presence of an oxide structure for all the presented measurements. In the end, the author tried stripping off the primary oxide very slowly (timescale of about a week). A major part of the sample remained without major cracks, but the required recontacting of the sensing wires failed because of the extreme sample brittleness after this process. Obviously the oxide layer arising during the dealloying process contributes to the mechanical stability of the sample.

Again the resistance behavior during pseudocapacitive charging was investigated. Figure 4.18-4.19 show the results of one of the first CVs recorded. Again an additional minimum in resistance change was observed and the general trend is opposite to charging, i.e $\varrho < 0$. The additional small local minimum in resistance change was always measured at the lowest potentials applied. Once again, no special characteristics can be obtained from the CV explaining this behavior.

Figure 4.20 exposes the opposite behavior of the resistance change and potential (and charge, which is nearly in phase with the potential) time response, which arises with higher potentials applied. The resistance change of the first cycle presented ($U_l = 0\,\mathrm{mV}$ and $U_h = 100\,\mathrm{mV}$) is synchronous to charging, but upon reaching higher U_h values a behavior like that presented in figure 4.18 emerges. For investigations on the influence of another electrolyte, resistance changes at potentials assigned to pseudo capacitive charging have been recorded in 1-M KCl as well. Excerpts of the time dependence of charge and resistance changes for both electrolytes are presented in the appendix, figure B.3. Further analysis of the charge response due to charging is shown in figure 4.21. In KCl the additional minimum in resistance variation vanished and exhibit opposed behavior between resistance change and charge almost over the whole potential (and charge) regime. Also the CV recorded in KCl revealed no special characteristics (see figure B.4). In case of this (final) sample, it was attempted to remove the primary oxide very slowly (in the time frame of one week) by means of a sequence in which the applied potential is continuously swept to more negative values. After half of the time a bigger part of the surface oxide had been removed and the sample was still operative and no macroscopic cracks were observed. At this point the sequence to reduce the oxide layer entirely was interrupted, and the measurements to compare the influence of different electrolytes (figures 4.21, B.3, B.4) were performed. The comparison figure 4.18 with figure B.3b points out that the oxide layer clearly effects the resistance behavior.

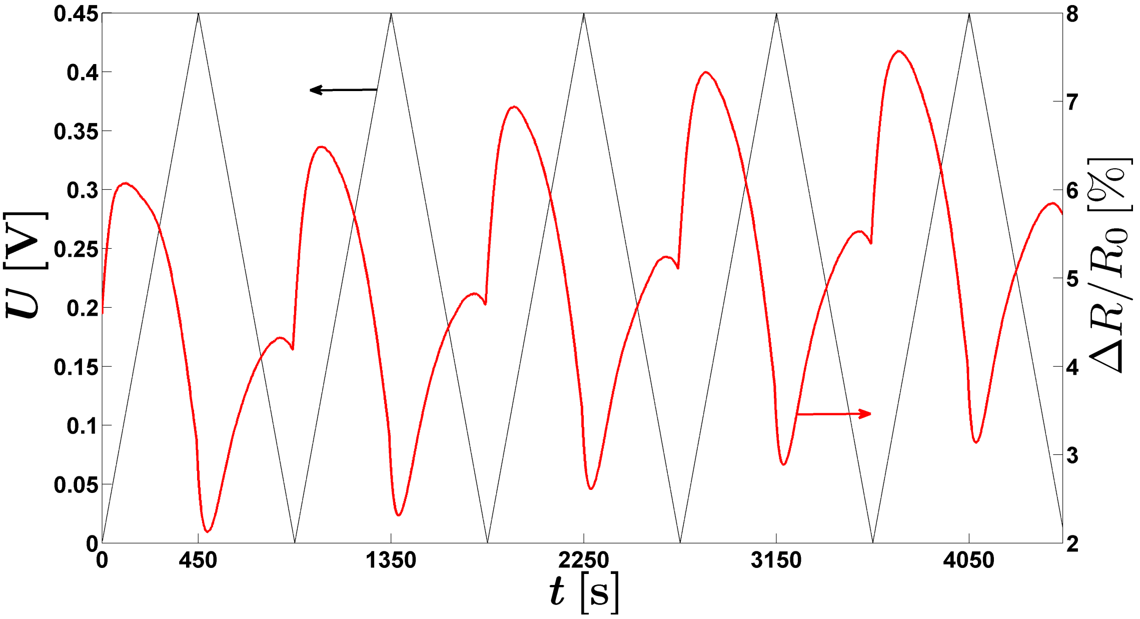

(a) Resistance and voltage time dependence

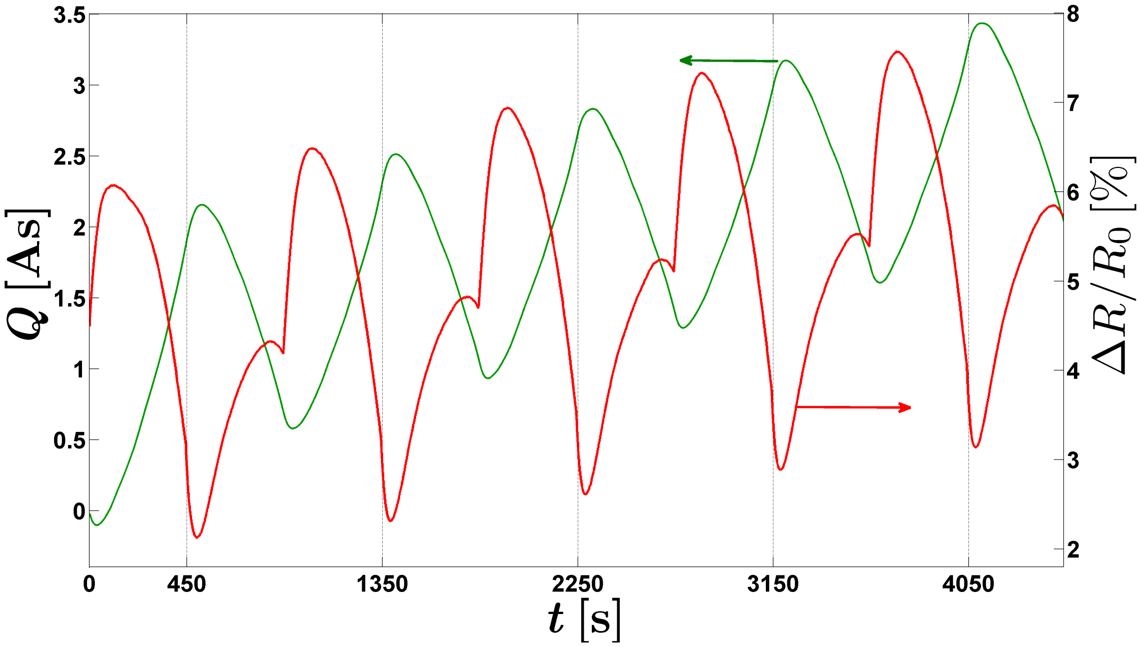

(b) Resistance and voltage time dependence

Figure 4.18: $TUG-NPP_8$, $R_0 = 2.024\,\Omega$. Charge and resistance behavior during one of the first CVs, details in the caption of figure 4.19. The vertical lines mark the times at which the potential reached its maximum value U_h

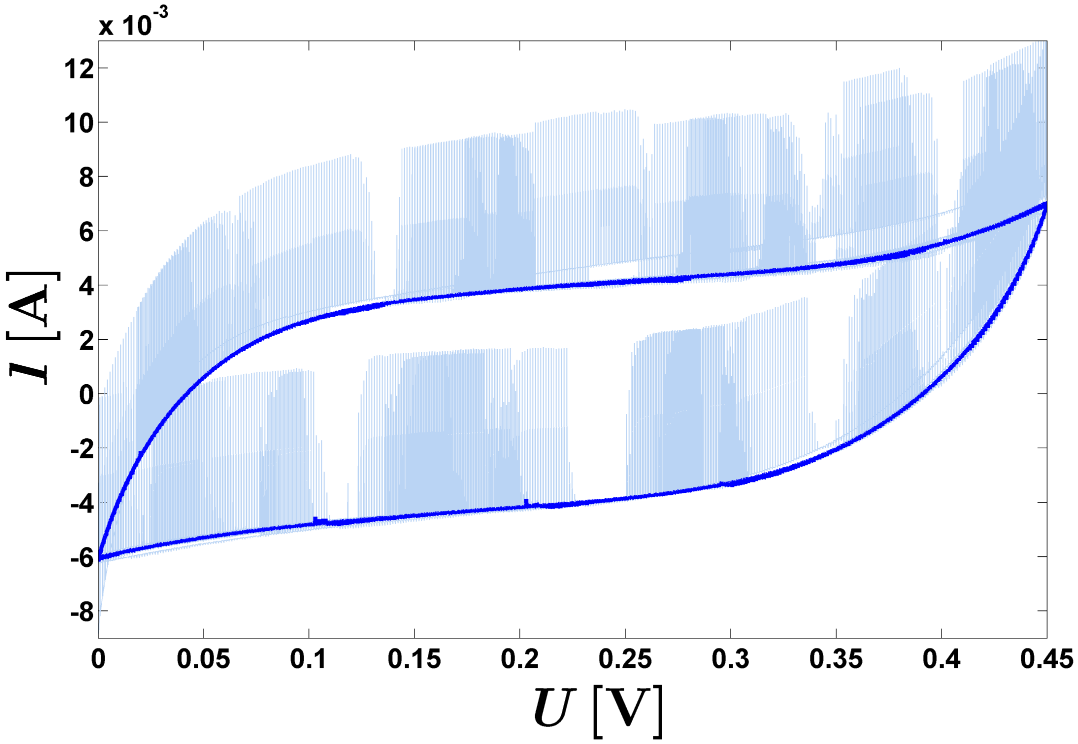

Figure 4.19: $TUG - NPP_8$, one of the first CVs, ($U_{start} = U_l = 0\,\mathrm{mV}$ and $U_h = 450\,\mathrm{mV}$, $v = 1\,\mathrm{mVs}^{-1}$). The dark blue line designates the 8^{th} cycle without the additional peaks resulting from the resistance measurement. Again, no peaks were observed that may explain the sign inversion of resistance changes.

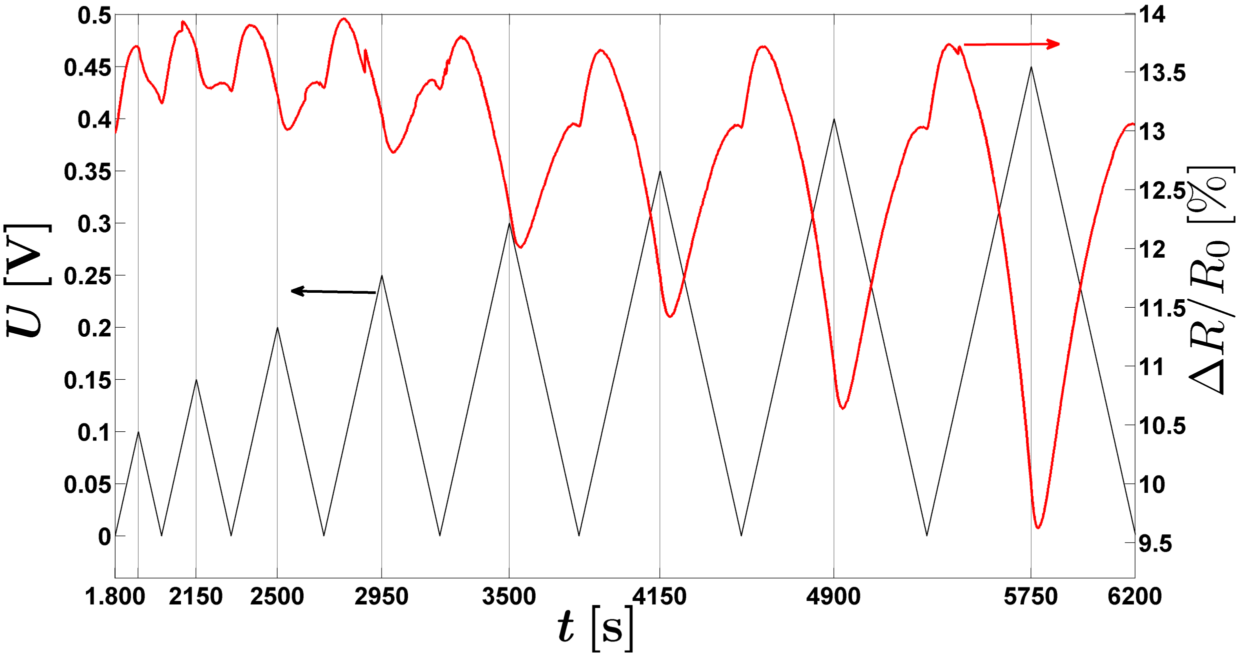

Figure 4.20: $TUG - NPP_8$, $R_0 = 2.024\ \Omega$. Sequence 12: CVs with increasing U_h values ($U_{start} = U_h = 0\,\mathrm{mV}$ $v = 1\,\mathrm{mVs}^{-1}$ and $U_h = 100, 150, 250, 300, 350, 400, 450\,\mathrm{mV}$). The vertical lines mark the times at which the potential reached its maximum value U_l to separate the cycles.

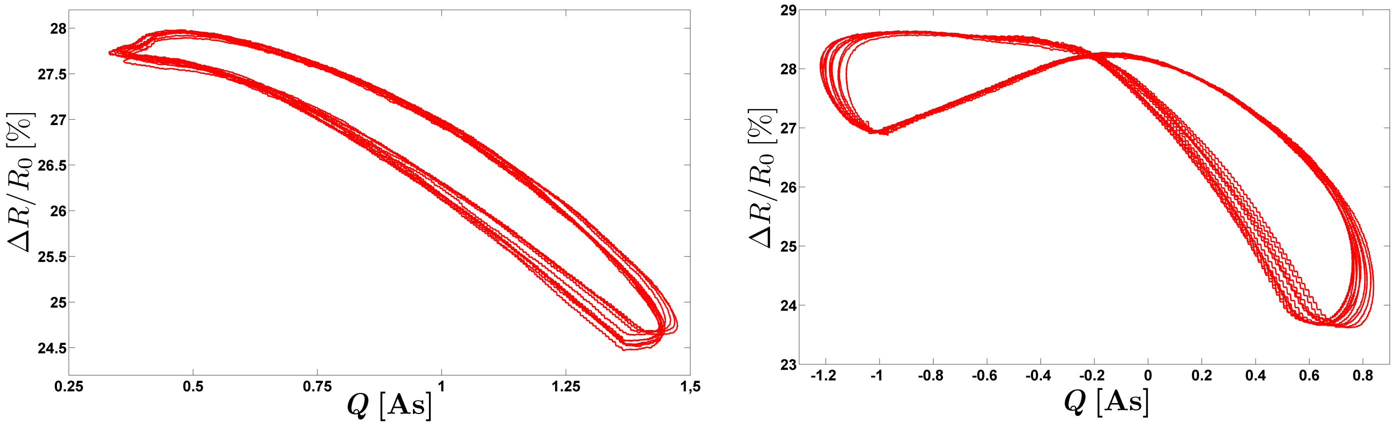

(a) Electrolyte 1-M KCL, pH=7. CV settings: $U_{start} = U_l = 340\,\mathrm{mV}$ and $U_h = 863$ mV, 15 cycles using $v = 1\,\mathrm{mVs}^{-1}$.

(b) Electrolyte 1-M KOH (as usual), pH=14. CV settings: $U_{start} = U_l = -100\,\mathrm{mV}$ and $U_h = 445$, $v = 1\,\mathrm{mVs}^{-1}$, 15 cycles using $v = 1\,\mathrm{mVs}^{-1}$.

Figure 4.21: $TUG - NPP_8$, $R_0 = 2.024\,\Omega$. Comparison of the resistance change with charging for different electrolytes during a CV. The plots were generated from the last eleven cycles. Exerpts of the corresponding time response are shown in the appendix, figure B.3.

4.2.4 Sample $TUG - NCP_1$

The preparation of sample $TUG - NCP_1$ and difficulties caused by limited contact with the sample, are described in chapter 3.2. A resistance correction to compensate for additional effects on the measured resistance caused by the current running through the potentiostat became necessary. This correction is derived and discussed in the appendix, section B.3. A basic difference from the $TUG - NPP$ samples is the absence of a primary oxide layer and that samples remained stable over the whole potential window of the aqueous electrolyte. No drift in resistance was observed during the investigations and the value R_0 was chosen as the initial value after fabrication. The measurements presented here are similar to those presented in the work of Sagmeister [9] and only differ somewhat in the applied potentials.

The nanocrystalline samples were primarily prepared for the purpose of comparing with the measurements presented in the last two subsections. Because the nanocrystalline samples were stable at all investigated potentials, recording the resistance during a CV in the complete potential window of the aqueous electrolyte became feasible. The results are shown in the figures 4.22-4.23. Unfortunately, the connection of the sample $TUG - NCP_1$ was destroyed before investigating the resistance changes in the pseudo capacitance charging regime. This kind of measurement was performed with sample $TUG - NCP_2$.

From the slope in figure 4.23 and a normalization by the sample surface area (see table 4.1) yields a charging coefficient of $\varrho = 3\ \frac{\%\ m^2}{As}$.

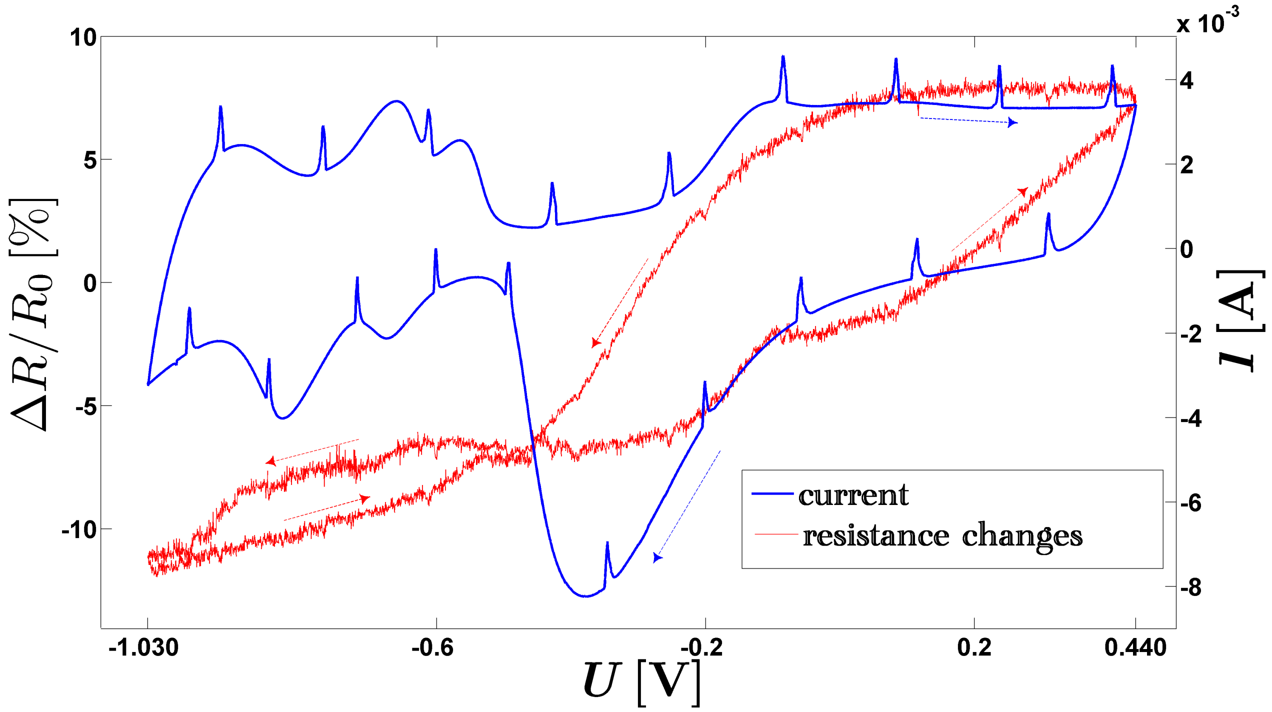

Figure 4.22: $TUG-NCP_1$, $R_0 = 0.00561\ \Omega$, resistance measurements during the 3^{rd} cycle of a CV ($U_l = -1030\,\mathrm{mV}$ and $U_h = 440\ \mathrm{mV}$, $v = 0.2\,\mathrm{mVs}^{-1}$)

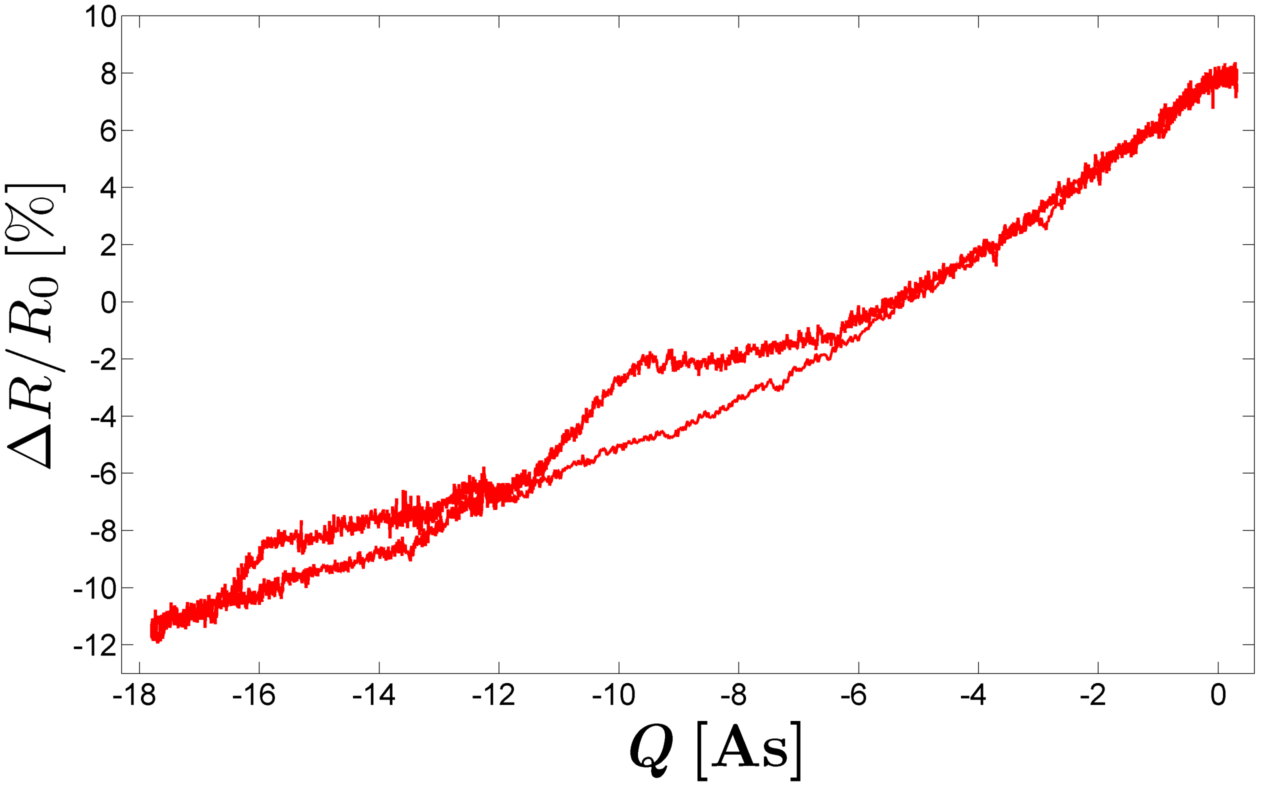

Figure 4.23: $TUG-NCP_1$, further analysis of figure 4.22. The slope in the regime assigned to oxide formation and its reduction ($-10 \leftrightarrow 0\,\mathrm{As}$) is $\approx 1.4\ \frac{\%}{As}$.

4.2.5 Sample $TUG - NCP_2$

For the sample $TUG - NCP_2$ the initial situation was the same as for $TUG - NCP_1$. To enable measurements comparable to what was done for the samples $TUG - NPP_5$ and $TUG - NPP_8$, the sample $TUG - NCP_2$ was oxidized applying potentials of $450\,\mathrm{mV}$ for several hours. As in the case of sample $TUG - NPP_5$ and $TUG - NPP_8$, the measurements presented here were all recorded avoiding potential regimes associated with reduction of this oxide layer. It should be mentioned that subsequent reduction of this oxide layer during a CV, did not exhibit a larger area or a more negative potential value of the first reduction peak compared to the following. This was different for the dealloyed samples (see section 4.1.4).

Charging of the specimen was performed by multistep CA measurements. The voltage applied to the WE was incremented in steps of $50\,\mathrm{mV}$ at intervals of $10\,\mathrm{min}$. Taking into account only resistance values recorded at the end of a CA, because of low currents expected there, should minimize additional effects on the resistance measurement. Figure 4.24 shows the time dependence of the resistance and potentials applied. The relationship between charge and resistance seems to be a linear one, as shown in figure 4.25.
The behavior of the dark red line in figure 4.24 could not be explained by misleading current effects (see section B.3 in the appendix), because the change in the charging current direction after reaching the highest potential applied did not result in an immediate change of the resistance (as in the case of the bright red curve, displaying the continuously measured resistance values, which are obviously affected by the sample charging current just after a change in the applied potential). Figure 4.25 was obtained taking into account only the dark red dots of figure 4.24 after correcting them using the mentioned resistance correction for the $TUG - NCP$-samples. However, the correction did not significantly affect the resistance values, because of the low charging currents flowing when they were recorded.

For the nanocrystalline sample, even if an oxide layer was present, no sign inversion of the charging coefficient ϱ was observed and the sign of ϱ was revealed to be in line with measurements on NPG by Wahl et al. [12]. This indicates that the sign inversion of ϱ observed for the $TUG - NPP_{5\&8}$ originates from characteristic features of the dealloyed samples.

To compare the data of sample $TUG - NCP_2$ with those obtained for the sample $TUG - NCP_1$, the slope of $\frac{\Delta R}{R_0}$ vs. $\Delta Q \approx 0.9\,\frac{\%}{As}$, was determined from figure 4.25. To derive the percentage in resistance change, a value of $R_0 = 0.0078\,\Omega$ was used which was the sample resistance right after fabrication (as done in case of sample $TUG - NCP_1$).

The transfered charge was derived directly from the current versus time behavior. It should be noted here that in literature a constant background current, present in the amperometric data, is usually subtracted if sample charging is performed by means of multistep CA measurements [9, 12, 1, 50]. The subtraction of appearing background currents is described explicitly in the Maser's thesis of Wahl [12]. Nevertheless, as far as the author knows, a good explana-

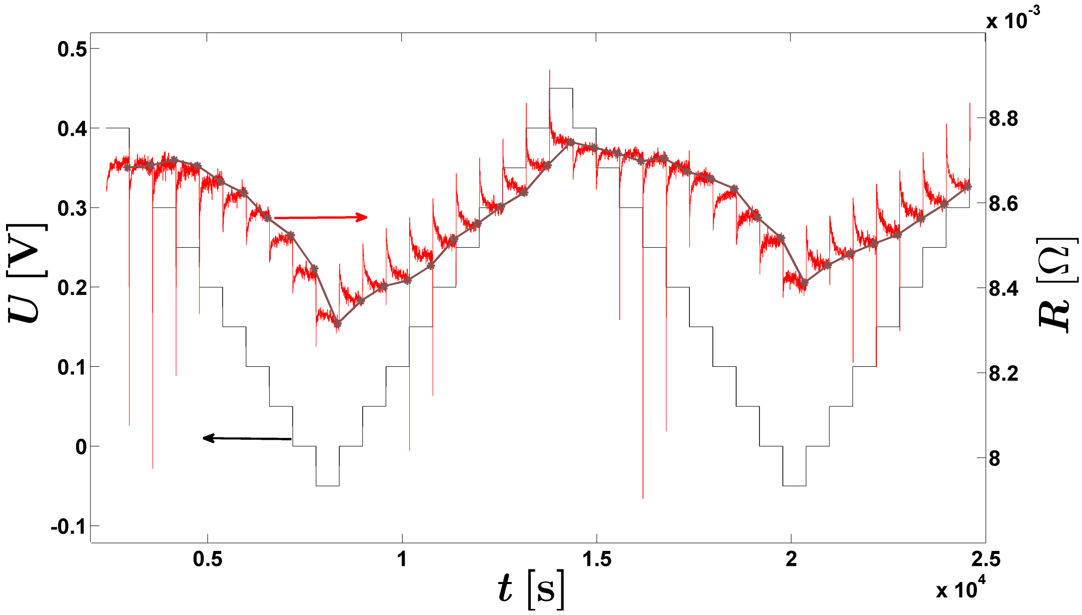

Figure 4.24: Sample $TUG - NCP_2$, time dependence of the resistance at different potentials successively applied with potential steps of $50\,\mathrm{mV}$ after ten minutes. High currents perturb correct resistance measurements, which is apparent from the spikes in resistance observed at high current values after switching the voltage. The dark red dots mark resistance measurements at the end of each CA and should be regarded as the main result of this sequence.

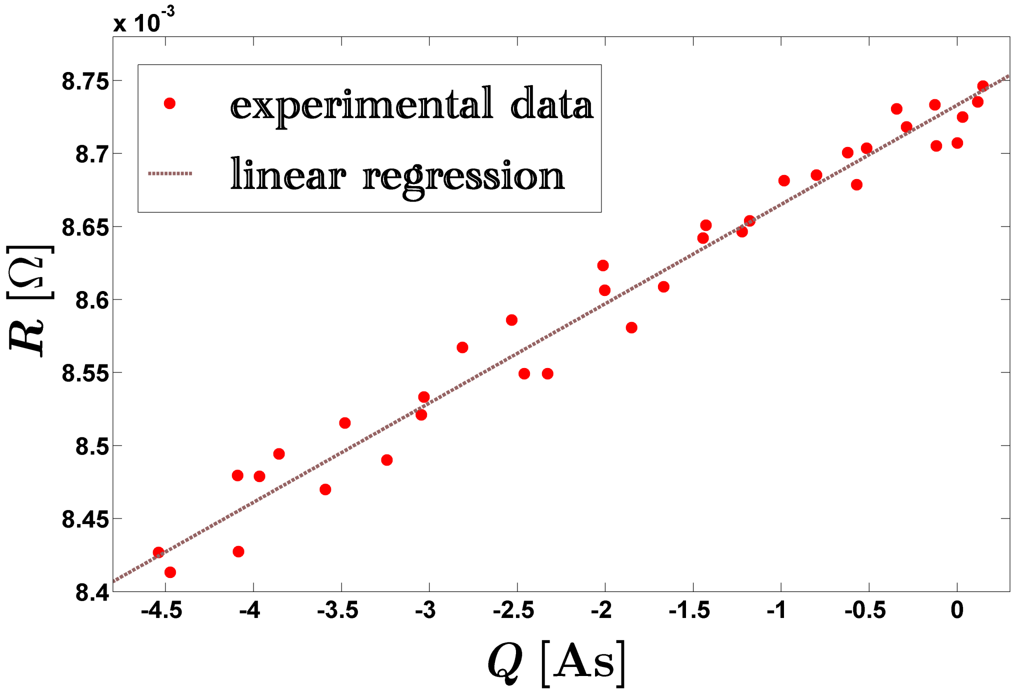

Figure 4.25: Sample $TUG - NCP_2$, further evaluation of figure 4.24, relating corrected resistance data with the recorded charge.

tion of their origin has not been given so far. The analysis of the presented charging values using this background subtraction yields scattered R(Q) data. This may be attributed to the shorter CA times compared to literature because in this case the constant background subtraction appears to be inappropriate[5]. Analysis of sample charging using this subtraction of a background current as done by Wahl [12] yields lower variations in charge ($\Delta Q \approx 33\%$ lower). Hence such an evaluation would result in a $\frac{\Delta R}{R_0}$ vs. ΔQ slope of $\approx 1.35\ \frac{\%}{As}$.
A normalization by the sample's surface area (see table 4.1) yields a charging coefficient of $\varrho = 2 - 3\ \frac{\%\ m^2}{As}$.

4.3 Initial studies with ionic liquids

This section reports on initial attempts using ionic liquids (ILs) as electrolytes. Discussion and conclusions of a first dealloying experiment in an IL are presented.
All the measurements during this thesis were performed in aqueous liquids, whereas ionic liquids are melted salts. Usually the therm ionic liquids is used, if their melting point lies below 100°C. High thermal stability, good ionic conductivity, low vapor pressure and a wide electrochemical window, spanning up to 6 V in some cases [53], are interesting properties enabling new kinds of measurements. Until now, just a little experience in fabrication and investigation of nanoporous samples in ionic liquids exists. The generation of nanoporous gold and platinum [26, 54] and other metals [55, 56] in IL has already been reported. All of them were fabricated employing related techniques described below. At first Zn was electrodeposited on a pure polished metal surface in an IL, in general 1-ethyl-3-methyl chloride zinc chloride($EMIC - ZnCl_2$), using a Zn-counter electrode at temperatures in the range of 120-150°C (the successive constitution of an alloy was shown by X-ray diffraction, cyclic- and linear stripping voltammetry). Through a subsequent dealloying step in the same IL, the nanoporous structure was obtained. Zinc(II) species consumed during the electrodeposition could be recovered during the dealloying step and therefore the IL was reusable [57]. The fabrication of entirely dealloyed samples, large enough for resistivity measurements using our experimental setup (see section 3.4), seems to be awkward applying the method described above. Hence an experiment of dealloying our $Cu_{75}Pt_{25}$ starting alloy (see section 3.1.1) in an IL was executed. The goal was to expose arising difficulties, evaluate opportunities and to design equipment and hardware for further experiments intended in ILs. Dealloying in a aqueous liquid and subsequent chemical measurements in an IL are not favourable because of moisture remaining in the porous system.

---

[5] The subtracted background currents are determined from the current value at the end of a single CA curve. Only after a sufficient period of time, these currents are no longer assigned to chemical reactions or double layer charging.

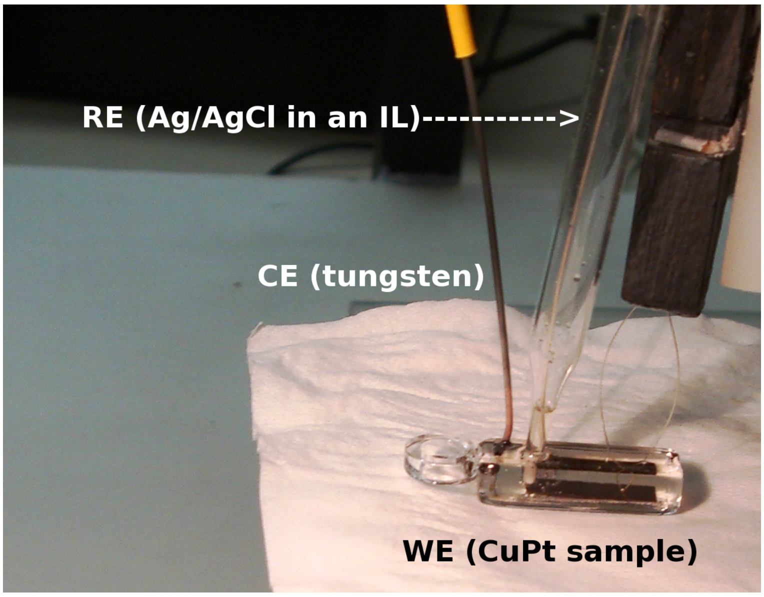

Figure 4.26: Experimental setup to dissolute Cu out of a $Cu_{75}Pt_{25}$ starting alloy in an ionic liquid

4.3.1 Dealloying procedure in an ionic liquid

The experimental procedure of our first dealloying trial in an ionic liquid is resumed here. We performed the dealloying experiment under normal environmental conditions using 1-ethyl-3-methylimidazolium tetrafluorborate ($EMID-BF_4$) from the company "io-li-tec" as electrolyte. Figure 4.26 shows the experimental setup. The immersed $Cu_{75}Pt_{25}$ starting alloy was connected through a platinum wire, a tungsten rod was used as counter electrode and an Ag/AgCl (in an IL) served as reference electrode. The equipment applied to control voltages and record currents was the same as in the previous dealloying experiments.

4.3.2 Evaluation of the experiment and perspectives for improvement

The failure of our dealloying trial should be revealed first. This subsection deals with the description and evaluation of the experiment and a proposal to upgrade our experimental design.

In contrast to aqueous electrolytes a significant current flow from the working electrode ($Cu_{75}Pt_{25}$-Sample) to the counter electrode (tungsten rod) was only obtained applying extremely high potentials (≈ 4 V vs. 1-M Ag/AgCl). Furthermore the IL continuously changed its color from transparent to brown during the measurements (see figure 4.27), indicating a modification of the IL. Because of the evident damage of the IL, which resulted in uncontrollable chemical processes, the experiment was aborted. In figure 4.27b one can clearly distinguish the emerged, obviously heavier, brown phase from the still transparent IL. Figure 4.29a

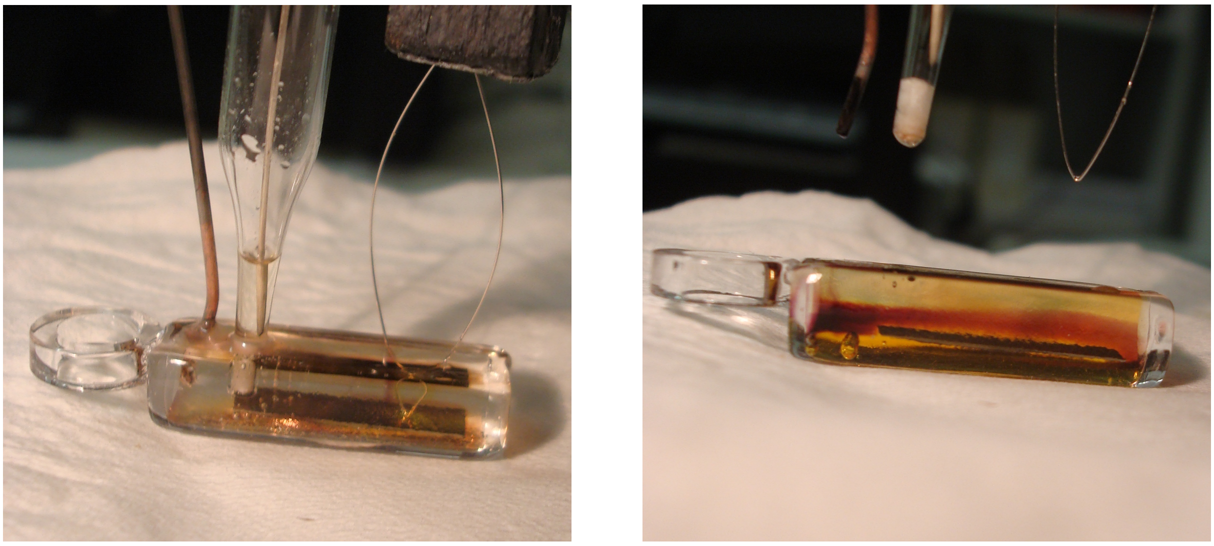

(a) sample after 30 min at 4 V vs. $Ag/AgCl(in\ an\ IL)$

(b) IL after the aborted experiment

Figure 4.27: IL modification with time

shows the sample after the followed cleaning process. Because of a change in the specimen's color (see figure 4.29a) a transition of the surface could not be excluded. The XRD pattern 4.28 showed neither peak broadening, which indicates transitions to smaller coherent scattering domains as expected for nanoporous structures, nor a shift in the peak positions, which occurs if the copper ratio alters. The behavior under the optical microscope[6], see figure 4.29b, showed that the color change resulted from an additional new surface phase. Nevertheless during the cleaning process the dissolver changed its color to green while rinsing the sample. As a consequence of this, it was concluded that some copper was removed from the alloy. An inhibited diffusion process away from the working electrode might explain that the described color change only occurred while rinsing the sample and not while rinsing the counter and reference electrode or the basin. Copper was also not expected to be an ingredient of the generated brown phase for two reasons. First, because its color did not change during the cleaning process. Secondly because the "dealloying-current" stayed constant, even when the arising brown phase arrived at the counter electrode. At the applied voltages copper ions would have been reduced at the counter electrode facilitating a higher current.

The failure of the dealloying experiment probably is due to the following reasons [58].

- The dissolved copper could not penetrate into the electrolyte, e.g because of the formation of a neutral complex.
- In the dealloying process, not only a proper reaction pathway for the oxidation of the less noble metal at the working electrode is required. There must also be a possibility

---

[6] Focusing on the "blue phase" and the blank alloy at the same time was not possible.

for a reduction reaction at the counter electrode from the very beginning. Presumably the brown phase originates from the destruction of the IL acting as an oxidant.

An experimental design to overcome the emerged obstacles will be proposed. The focus during development had especially been on the dealloying of copper from platinum, but the presented appliance could either be used for dealloying other alloys or successive measurements in an IL. The draft given in figure 4.30 and the proposed chemistry was developed under supervision of S. Landgraf. In the proposed set up the oxidation and the related reduction process are carried out in different electrolytes, separated through a teflon frit with pores in the range of 5 µm enabling ion exchange. The right basin is designed for the IL, containing the immersed sample and the reference electrode. It is smaller to conserve IL. Nevertheless, the IL should be replaced after the dealloying for successive measurements. The left basin, where the counter electrode is placed, could also contain an organic liquid with a conducting salt. Its cation will be deposited at the counter electrode which provides a proper reduction process. The salt should be available in a proper concentration (depending on the amount of copper in the sample) ensuring a continuous reduction. Owing to the availability that organic liquids sustain high temperatures ($> 100\,°C$), dealloying could be carried out at much higher temperatures than now with out complex equipment. This might be desirable for the dealloying process if the more noble compound has a low surface mobility, like platinum.

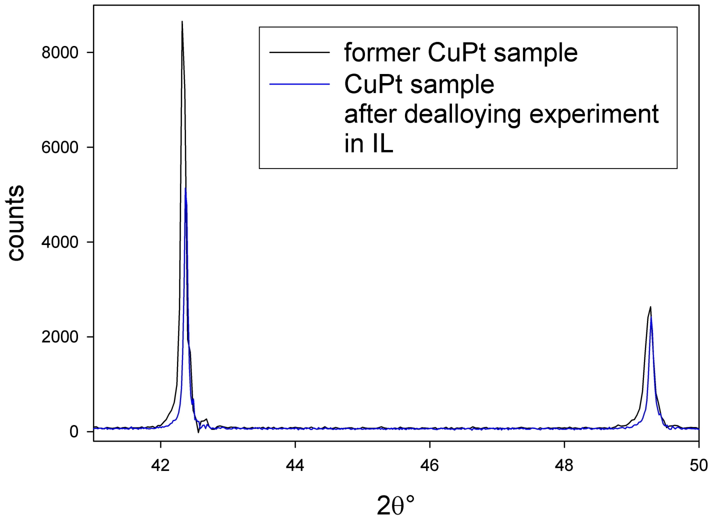

Figure 4.28: XRD analysis. Primary material versus the sample after the experiment: No change in the peak position and no peak broadening becomes obvious

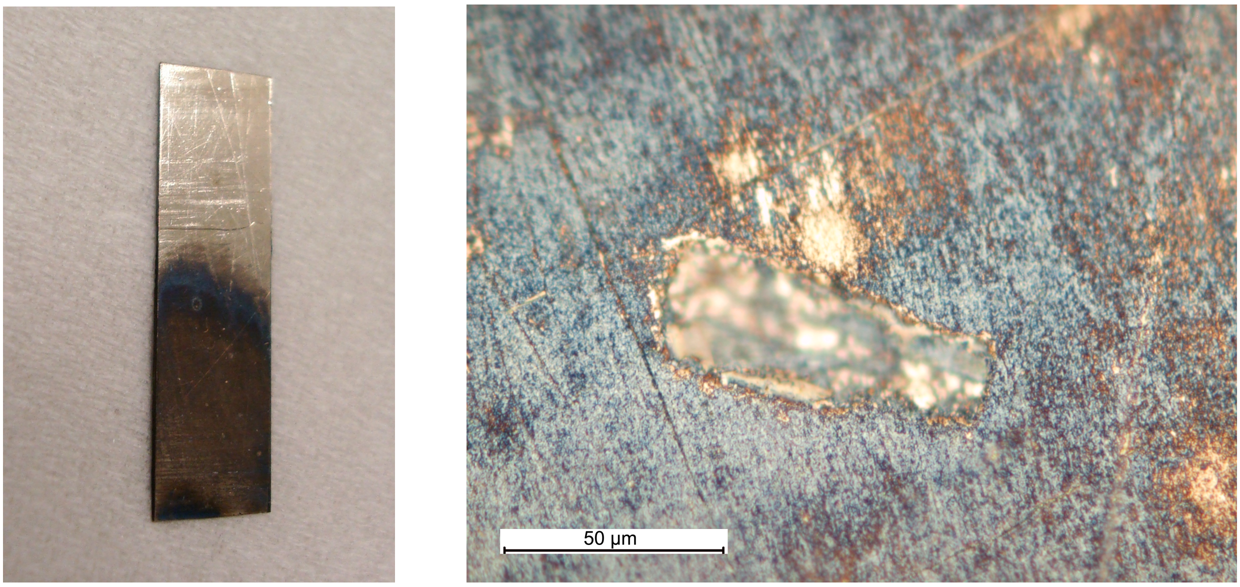

(a) Sample overview **(b)** Microscope picture of the colored sample part

Figure 4.29: Sample after the aborted dealloying experiment in an IL

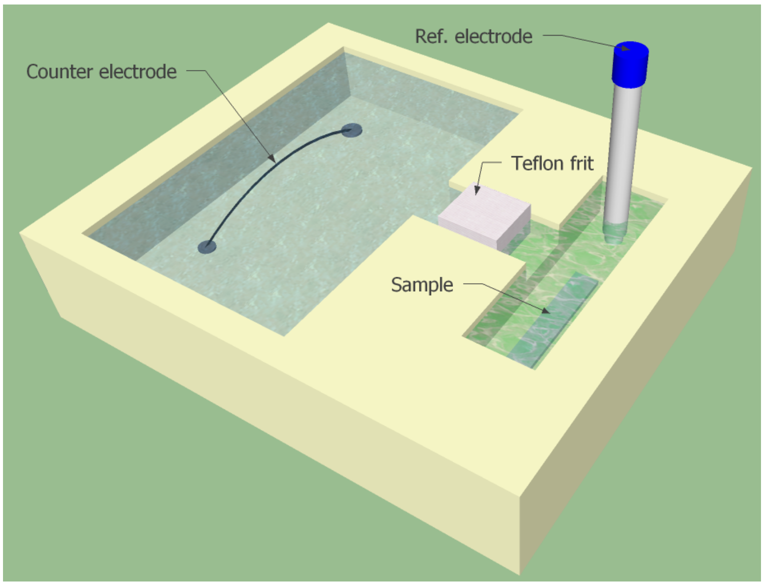
Ref. electrode
Counter electrode
Teflon frit
Sample

Figure 4.30: Draft of a possible experimental setup, designed for dealloying in an IL [58].

Chapter 5

Discussion

In this chapter the interesting results of the previous chapter are discussed. Especially the resistance measurements of chapter 4.2 are evaluated extensively in view of the remarkable effect of (unexpected) sign inversion in the resistance vs. charging behavior. The observed resistance changes are compared to literature, in particular to the works of Sagmeister et al. [9, 2], to answer questions regarding the difference between nanocrystalline and nanoporous samples.

Initial studies of the magnetic moment of NPP in dependence of charging are presented in the appendix in chapter A. Interpretation of sample characterization measurements is carried out in the corresponding sections and subsections and is not an issue in this chapter.

5.1 Resistance measurements in dependence of electrochemical charging

5.1.1 Nanocrystalline platinum

Resistance changes of the sample $TUG - NCP_1$ could be measured applying the whole potential range possible in aqueous electrolytes as presented in figures 4.22 and 4.23. Plotting the resistance change versus the charge during the CV revealed a reversible, nearly linear behavior. The charge coefficient ϱ remained positive during the entire measurement. To compare the charging coefficients with results presented by Sagmeister [9] the *core-shell-model* has to be introduced here.

The idea is that charging only affects the charge density in a space-charge-region (see chapter 2.7.1) of thickness δ. Its principle is shown in the draft given in figure 5.1. To elucidate the charge response of the resistance, Sagmeister calculated the accumulated charge (during

CA curves) per atom located in the space-charge-region using

$$\Delta q_{scr} = \frac{\Delta Q M_{mol}}{\omega N_A m_{sample}} , \tag{5.1}$$

where ω is the percentage of affected material (as derived in 2.7.1 for cylindrical geometries), N_A the Avogadro constant, M_{mol} the molar mass (in this case of platinum), the recorded total charge ΔQ and the sample mass m_{sample}.

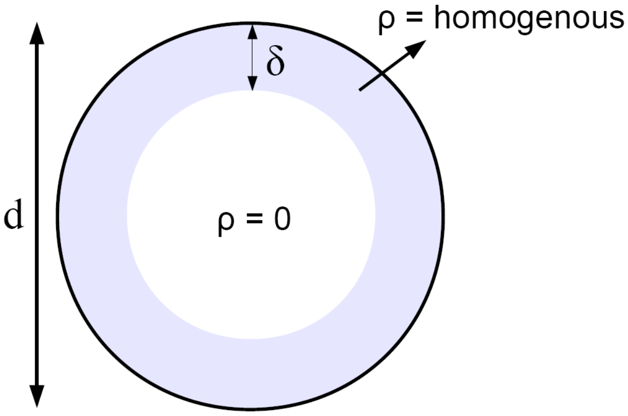

Figure 5.1: Principle of the *core-shell-model* described in [7]. Charging is assumed to affect only the charge density ρ in the outer shell. ρ remains constant inside the inner shell of $(d - \delta)$ in diameter.

Regarding the oxidation and reduction regime of the oxide layer in figure 4.23 ($-10 \leftrightarrow 0\,\mathrm{As}$)[1], evaluation of the $\frac{\Delta R}{R_0}$ vs. Δq_{scr} slope using the same value for ω as done in [9][2], revealed a value of $11.06\ \frac{\%}{e^-/atom}$, which is in very close agreement with the value extracted from the Master's thesis of Sagmeister [9] ($\approx 11.08\ \frac{\%}{e^-/atom}$).

Resistance measurements performed during a CV, cycling over similar potential regimes, are presented by Fujihira and Kuwana [47] for platinum thin-films. Observed resistance characteristics like little conductance changes as the potential scan is continued into the second wave of hydrogen adsorbtion (compared to the first wave), which was discussed in terms of a slight change in specularity parameter p (see equation 2.13b), could not be resolved. Perhaps limited experimental accuracy could be seen as a reason for inconsistent results. One has to remember that measurements presented in figures 4.22 and 4.23 were recorded during a whole day. Despite the fact that resistance data could only be recorded during one complete cycle at once and resistance corrections are not expected to be free from errors (see appendix, section B.3), the evaporating electrolyte may caused changes in the ionic strength. Nevertheless, the shape of the resistance changes in the oxidation regime look similar to the results in [47].

---

[1] Sagmeister just performed measurements according to this regime, also using 1-M KOH.

[2] This is reasonable because of an equal sample fabrication and very similar surface areas (see table 4.1).

The rapid increase in resistance at the commencement of the oxidation regime assigned to anion adsorption was also observed in [9], where KOH is used too [3], but not in [47] where H_2SO_4 was applied. According to Tucceri [8], it was suggested by Mansurov et al. [59] that for relatively weak adsorption of SO_4^{-2} ions, the resistance change of platinum films is mainly determined by the change of the free surface charge, while in the case of strong adsorption the increase in resistance is due to the fixation and scattering of conducting electrons, the change of thickness of the conduction layer and other effects.

The discussion in the works of Sagmeister [9, 2] presents a quantitative analysis of resistance changes only for capacitive double layer charging charging. For the sake of comparison the oxidized NPP-samples, capacitive charging of NCP-samples were investigated only in the pseudo-capacitive regime, i.e solely capacitive charging upon an oxide layer. Pseudo-capacitive charging was investigated in the case of sample $TUG - NCP_2$ and the results are presented in chapter 4.2.5. In the pseudocapacitive regime the charging coefficient ($\varrho = 2 - 3 \ \frac{\% \, m^2}{As}$) was observed to be two times smaller than that in the double layer regime [2][4] ($\varrho = 5 \ \frac{\% \, m^2}{As}$). This is in agreement with findings for NPG where the charging coefficient is reported to be about $50 \ \%$ larger for simple double layer than in case of pseudo capacitive charging [1].
According to [2] the interpretation of the double layer regime is the following:
the R increase upon positive charging is in qualitative agreement with the free electron model ($\sigma \ \propto \ n$), but the absolute changes of the resistance ΔR are much too high. The phonon-induced scattering of the s-band electrons, which are mainly responsible for the electron transport, into empty states of the d-band yields a major contribution of the electrical resistance. Upon positive charging the density of states at the Fermi-level $D(E_F)$ increases (and hence $N_d(E_F)$, see chapter 2.7.1) and, therefore, the scattering of s-band electrons into holes of the d-band increases. The change in charge-induced ΔR due to modification of s→d-band scattering is in qualitative agreement with the observed variation of $\frac{\Delta R}{R}$ with Q. A quantitative consideration in the framework of a rigid band model shows however that a six times higher ΔR would be expected. Possible explanations for this divergence are deviations from the rigid band model and the fact that grain boundary scattering, which plays a major role in the resistance too, especially in the case of nanocrystalline samples is not sensitive to charging. The effect of charge-induced strain on the charge-induced resistance variation appears to be small.
The difference in the charging coefficients of simple double layer and pseudo capacitive charging may originate from the variation of scattering at the crystal-electrolyte interface

---

[3] In fact it was observed only in 1-M KCL mixed with 0.01-M KOH ($pH \ = \ 12$). In case of 1-M KOH the used method (CA curves were recorded using stepwise increasing potentials with an increment of 100 mV) could not resolve such a characteristic.

[4] Because both samples were fabricated using the same material (see chapter 3.2), the samples should have the same c_{size} and a comparison using equation 2.16 should reveal the same result.

upon charging.

5.1.2 Nanoporous platinum

The removing of the oxide layer arising during the dealloying process, i.e the primary oxide, led to sample destruction. Hence reversible cycling of the applied potential was restricted to the pseudo capacitive regime.

Upon initial cycling with small ΔU a positive charging coefficient occurs, which is in agreement with the trend of charging observed for the nanocrystalline samples. A quantitative comparison of the charging coefficient ϱ in the pseudo capacitive regime with that of nanocrystalline platinum (sample $TUG-NCP_2$) is difficult because of the lack in knowledge of the surface area of the nanoporous samples. From the alloy weight before the dealloying process and the assumption that dealloying halves the sample weight, which will be described in section A.4, the weight of a $TUG-NPP$-sample is estimated at 70 mg. From the specific surface area ($39.5-51.6\ \frac{m^2}{g}$, see table 4.1) and the $\frac{\Delta R}{R_0}$ vs. ΔQ slopes of sample $TUG-NPP_5$, ($15.12-16.07\ \frac{\%}{As}$, see figures 4.15b and 4.17b) a charging coefficient of $\varrho = 42-56\ \frac{\%\ m^2}{As}$ is derived.

This value is far above that measured for our nanocrystalline sample $TUG-NCP_2$ ($\varrho = 2-3\ \frac{\%\ m^2}{As}$) or nanoporous gold ($\varrho = 14\ \frac{\%\ m^2}{As}$). The latter value is elucidated from the data of Wahl et al. [1] for pseudocapacitive chrging. As extensively discussed in chapter 2.8 these values ϱ can not be compared straightforwardly. Despite the larger value ϱ of our NPP-samples the charging coefficient $\varrho_{size.ind}$ (see equation 2.16) may not differ as significantly from that of our NCP-samples, because of a much smaller c_{size} in the case of the nanoporous samples (or a greater c_{size} in the case of the nanocrystalline samples) [5]. The structure sizes of the compared NPP and NPG samples should be comparable, and hence their values of c_{size}. Although the reference resistance R_0 is much higher in case of the investigated NPP samples, because of the rutted sample structure attributed to multiple cracks, the determined charging coefficient ϱ (and $\varrho_{size.ind.}$) of nanoporous platinum is higher than in case NPG. This suggests that capacitive charging has a higher influence on the resistivity of platinum than of gold. This would confirm the model that the resistivity of platinum is more sensitive to charging because of modification in the scattering rate of conduction electrons into empty states of the d-band. Nevertheless one has to keep in mind that many assumptions had to be made to compare the charging values ϱ & $\varrho_{size.ind}$.

Upon numerous cyclings or an increase of the applied voltage U to more positive potentials, a sign inversion of the charging coefficient ϱ occurred. Positive charging resulted in a decrease of resistance, which is in contradiction to the theoretical aspects presented above.

---

[5] The structure sizes of the nanoporous samples are expected to be smaller than those of the prepared nanocrystalline samples.

The sign inversion in ϱ may result from an effect which is superimposed to the positive charging coefficient and which finally becomes dominant, giving rise to an overall sign inversion. The positive coefficient could be obtained again upon reducing U_h. No characteristics in the CV are observed that would indicate an influence of electrochemical reaction at the surface. Because of drastic differences in the resistance behavior between both samples for which the pseudo capacitive regime was investigated $TUG - NPP_{5\&8}$, quantitative values of the negative charging coefficient are hard to compare but are of the same order of magnitude as the positive ϱ values. It has to be noted again that a negative charging coefficient did not occur for nanocrystalline platinum samples. The following three scenarios may be taken into consideration to explain the appearance of a negative charging coefficient in the case of NPP-samples.

Scenario 1: Cu^{++} redeposition

A remaining copper content in the dealloyed samples, and hence the solution, is a major difference from the NCP-samples. In the applied potential regimes ($0 \leftrightarrow 450\,$mV vs. saturated Ag/AgCl RE, in 1-M KOH) copper stripping and redeposition can not be excluded [58]. Small amounts of copper stripped from the surface may influence the resistance, but could remain unexposed in the CV[6].

The dissolution of copper would occur at more positive, the redeposition at less positive potentials. According to Fujihira and Kuwana [47], it is clear that deposition of a Cu monolayer on Pt decreases the resistance of Pt film. Hence copper stripping at positive potentials is expected to increase the resistance. Because the reported resistance dependency on copper stripping/deposition is clearly contradictory to the observed ϱ sign inversion *scenario 1* is untenable and copper redeposition may not account for a negative values of ϱ.

Scenario 2: Decrease of the DOS at the Fermi level upon stron positive charging

From the peak structure of the energy dependence of the DOS (see figure 2.8), and the model of how $N_d(E_F)$ affects the resistance (see equation 2.12), the resistance is expected to decrease again if the Fermi level falls below the first maximum at $\approx 0.639\ Rydberg$. Experiments in this direction were performed by means of alloying palladium with rhodium. Doping with an element with fewer d-electrons [61] gives rise to the d-band filling.

From figure 2.8 the area between the Fermi level and this first peak (on the left side) was estimated:

$$A_{DOS-Pt} \approx 0.236\,\frac{states}{atom}. \tag{5.2}$$

Assuming the validity of the *core-shell-model* and a rigid band model, the charge required to fill this area is estimated as follows. Under the assumption that the space-charge-region comprises the entire sample, ($\omega = 1$, see chapter 2.7.1), a sample mass of $m_{sample} = 70\,$mg equation 5.1 leads to a value of

---

[6] The characteristics of copper (re-)deposition on nanostructured Pt are reported to differ drastically from those of planar surfaces [60].

$$\Delta Q_{NPP-sample} = A_{DOS-Pt} \cdot (-e) \cdot \frac{\omega \cdot m_{sample} \cdot N_A}{M_{mol-Pt}} \approx 8.18\,\mathrm{As}, \tag{5.3}$$

where e is the elementary charge. Recorded charge differences in the pseudo capacitive charging regime were about four times smaller [7]. A value of $\omega = 1$ may be valued far too high [43]. Calculations with a more realistic value of $\omega = 0.25$ might explain a sign inversion of ϱ according to this scenario. Anyhow, the fact that only minor variations in charge lead to the sign inversion of ϱ in case of the sample $TUG - NPP_8$ militates against scenario 2.
Notwithstanding this interesting idea cannot be ruled out, since the energy dependence of the DOS near the surface of NPP is unknown

Model 3: Length contractions on platinum with adsorbed oxygen species
It is reported in literature that the presence of an oxide yield to a sign-inverted surface stress-charge response for NPG [25] and NCP [5] [8]. At more positive potentials (positive charging) the specimens are reported to shrink in length l, which might yield a resistance decrease. It must be questioned why this should not yield a decrease in resistance in the case of the nanocrystalline samples?
According to Seeger and Schottky the electrical resistance of grain boundaries is associated with the free volume of the grain boundaries [62]. Therefore, in general, a decrease in resistance may be expected in highly disordered structures, like NPP, upon reduction of the specific free volume of the disordered structures.
One has to keep in mind the highly brittle, rutted sample structure. If the variations in length [9] cause additional reversible crack breaking/closure, this could account for the sign inversion in ϱ too. Vismanath et al. [5] reported alterations in length of $\approx 2 \cdot 10^{-2}\,\%$ obtained in the pseudo capacitive chargin regime. In terms of our $TUG - NPP$-samples this would give a change in length of $\approx 0.00028\,\mathrm{mm}$ [10]. From these slight variations only extremely small cracks can be assumed to (partially) close at higher potentials and cause the sign inversion. In conclusion scenario 3 may explain the negative charging coefficients of NPP in the pseudo capacitive regime.

The comparison of this effect to literature is difficult because such a sign inversion in the charging coefficients in the absence of specific adsorption is not reported as far as the author of this thesis knows. Winkes et al. [63] reported a sign inversion of $\frac{\Delta R}{R_0 \cdot \Delta Q}$ at more positive potentials for a 25 nm Ag(111)/Si(111) silver thin film electrode caused by the adsorption of

---

[7] Note that the point of zero charging did not served as starting value for charge recording.

[8] Determined in both cases via CVs in the pseudo capacitive charging regime combined with in situ dilatometry experiments.

[9] In [5] the length changes linearly with the applied voltage over the entire pseudo capacitive regime

[10] A higher surface-to-mass ratio, or different sample geometries may yield varieties of the percentage in length change used here.

Cl^- in 0.1-M KCl. The decrease in resistance was assigned to the formation of an ordered adlayer. The given explanation is that an ordered adlayer can scatter electrons only with momentum transfer according to the reciprocal vectors of the ordered adsorbate mesh, whereas for unordered adsorption all scattering channels are open. This means a decrease in the number of diffusive scattering events of conduction electrons at the surface. This remarkable characteristic is not expected to cause the sign inversion observed in this thesis, because the high ordered structures investigated in [63] differ drastically from the nanoporous structures arising in the dealloying process.

What this section amounts to is that the resistance behavior of the NPP-samples brings up a lot of still unexplained questions. To answer them, it would be desirable to perform measurements in the double layer charging regime and compare them to data obtained in the pseudo capacitive charging regime. This requires the possibility of generating samples that remain stable after the primary oxide is removed. Experiments have shown that a proper heat treatment can yield more stable structures that still have an impressive surface to volume ratio. In the case of the small sample $KIT - NPP_4$ it was achieved by tempering, to generate a specimen which remained robust and (macroscopically) free of cracks after removing the primary oxide. Investigations on continuously enlarged ligament structures would enable another powerful tool to determine the correct physical backgrounds.

5.1.3 Comparison of nanocrystalline with nanoporous samples and thin films

As discussed in chapter 2.8 the comparison to literature values is not straightforward. Differences in $R_0,\ c_{size}$ and A influence the charging coefficients ϱ & $\varrho_{size.ind.}$. For further evaluation a ratio ϑ compares the resistance changes for (pseudo-) capacitive charging to that for chemisorption, e.g the ad/desorption of oxygen species which was used to ascertain all presented values that refer to chemisorption:

$$\vartheta = \frac{(\varrho_{size.ind})_{capacitive\ charging\ only}}{(\varrho_{size.ind})_{chemisorption}} \overset{\text{equal samples}}{=} \frac{(\frac{\Delta R}{\Delta Q})_{capacitive\ charging\ only}}{(\frac{\Delta R}{\Delta Q})_{chemisorption}}. \tag{5.4}$$

In the case of structurally identical samples, all the values, which make comparison of charging coefficients complicated, would cancel out.

ϑ of NPP

The evaluation using the $\frac{\Delta R}{R_0 \cdot \Delta Q}$ values obtained for the removal of the primary oxide for the samples $TUG - NPP_{2\&3}$ shown in figures 4.12 and 4.13b ($\approx 1.287\,\frac{\%}{\mathrm{As}}$ and $\approx 1.5663\,\frac{\%}{\mathrm{As}}$) and the values for pseudo capacitive charging of sample $TUG - NPP_5$, namely the slopes of region I in the figures 4.15b and 4.17 ($\approx 16.07\,\frac{\%}{\mathrm{As}}$ and $\approx 15.12\,\frac{\%}{\mathrm{As}}$) revealed $\vartheta_{NPP} = 11.7 - 20.7$.

ϑ of NCP
The $\frac{\Delta R}{R_0 \cdot \Delta Q}$ values of sample $TUG-NCP_1$ ($1.4\ \frac{\%}{As}$) determined for chemisorption and in the case of sample $TUG-NCP_2$ ($0.9-1.35\ \frac{\%}{As}$) the determined for pseudo capacitive chargigng yields a value of $\vartheta_{NCP} = 0.6 - 1$.

ϑ of NPG
From Wahl et al. [1] one obtaines the values $\vartheta_{NPG(dl)} = 2.4 - 3.3$ if $\varrho_{capacitive\ charging\ only}$ is determined by means of double layer charging, and $\vartheta_{NPG} = 2.3$. The latter value is determined by means of pseudo capacitive charging.

ϑ of gold thin films
From the charging coefficients of thin films presented in the work of Wahl et al. [1] calculated from other references, a value of $\vartheta_{Au\ thin-film(dl)} = 2.7$ can be extracted for double layer charging. To obtain this value, films of different thicknesses had to be compared which is not valid. Because the thin film used to determine the resistance changes due to chemisorption is ≈ 3 times thicker, which is tantamount to a higher c_{size}, the presented $\vartheta_{Au\ thin-film(dl)}$ might be valued too high.

Determination of more ratios ϑ from literature data turned out to be difficult because of missing data for resistance changes due to chemisorption and capacitive charging, for the same (or an equal kind of) specimen. Higher ϑ values in the case of smaller structure sizes suggest that, for decreasing structure sizes, the size independent charging coefficient for capacitive charging $(\varrho_{size.ind})_{capacitive\ charging\ only}$ increases faster compared to that for chemisorption $((\varrho_{size.ind})_{chemisorption})$. Wahl et al. [1] interpreted the variations in resistance due to the formation of a chemisorbed oxygen layer **and** capacitive charging in terms of charge-dependent scattering at the metal-electrolyte interface. The supposition might not be supported by the increasing values of ϑ for decreasing structure sizes, as explained in the following.
Assuming a simplified model in which diffusive scattering events of conduction electrons at the sample surface are the only contribution to the resistance, $\varrho_{size.ind}$ might be expressed as:

$$\varrho_{size.ind} = S \cdot Var_{Sdiff}. \tag{5.5}$$

Here S takes into account the amount of scattering at the surface and Var_{Sdiff} labels the variations in the rate of diffusive scattering events. Higher values of Var_{Sdiff} in terms of capacitive charging compared to that for chemisorption($(Var_{Sdiff})_{capacitivecharging} > (Var_{Sdiff})_{chemisorption}$) might explain the higher size independent charging coefficients

$\varrho_{size.ind}$ ascribed to capacitive charging:

$$(\varrho_{size.ind})_{capacitive\ charging} = S \cdot (Var_{Sdiff})_{capacitive\ charging} >$$
$$(\varrho_{size.ind})_{chemisorption} = S \cdot (Var_{Sdiff})_{chemisorption}.$$

The amount of conduction electron scattering at the surface is expected to become more significant if the structure sizes d [11] become smaller. Hence S is also expected to decrease with d. Either way, the ratio ϑ is independent of structure sizes and should remain constant for decreasing structure sizes according to this simple model:

$$\vartheta = \frac{S(d) \cdot (Var_S)_{capacitive\ charging}}{S(d) \cdot (Var_S)_{chemisorption}} = \frac{(Var_S)_{capacitive\ charging}}{(Var_S)_{chemisorption}}\ .$$

This independence is contrary to the mentioned values of ϑ which are higher if determined for smaller structure sizes.

---

[11] The designation d of structure sizes is only figurative. It may present the ligament diameters, or film thicknesses but stands for an arbitrary quantity related to the structure size.

Chapter 6

Summary and Conclusion

Physical properties of metals like resistance, optical properties, or the magnetic moment depend strongly on their electronic structure. The latter can be affected locally by applying external electrical fields, which results in variations of charge neutrality in a surface-charge-region. In the case of metals this space-charge-region is restricted to dimensions of one lattice constant, even if *high* fields are applied. The idea of generating samples that exhibit a high surface to volume ratio is the following. If the number of atoms contained in this space-charge-region becomes a comparatively large part, the overall quantities of a sample, if dependent on the electronic structure, can be controlled. Especially in the case of platinum, where charging is expected to have a large influence on the density of states at the Fermi level, this concept might yield interesting properties like controlled magnetism and a tunable resistance.

Very high homogeneous electrical fields can be achieved due to electrochemical charging. Applying proper potentials to the working electrode/sample (referring to a reference electrode which remains at a constant potential) led to the attraction of solvated ions. If these ions do not chemically react with the surface atoms, the latter can be compared to the charging of a capacitor.

If the structure sizes of a sample lie in the range of the mean free path of conducting electrons, scattering events at the surface contribute to the resistance. In addition to pure charging chemical variations in surface composition or geometry can affect the resistance too and might be used to tune the conductivity. In the framework of this work investigations of the resistance and the magnetic moment were performed.

Nanoporous platinum samples were prepared by dealloying copper out of an homogeneous $Cu_{75}Pt_{25}$ starting alloy. The successful generation of porous networks, which exhibit an impressive surface-to-volume ratio, is evidenced by scanning electron microscope images and electrochemical methods.

In the case of freshly created nanoporous platinum samples, an oxide layer was present on the surface. The removal of this primary oxide, by applying sufficiently negative potentials, leads to unavoidable sample destruction. This fact limited the accessible potential range. Detailed investigations of the resistance behavior were restricted to the pseudo capacitive charging regime. Sample charging in the latter regime revealed unexpected behavior and interesting features, like a sign inversion of the slope of $\frac{\Delta R}{R_0}$ vs. ΔQ ($\propto$ the charging coefficient ϱ). Nanocrystalline samples were generated to crosscheck the observed sign inversion but measurements using these samples did not reveal the sign inversion effect. Different models suggesting why this special characteristic was only observed in the case of nanoporous platinum samples have been discussed. A summary of the observed resistance behavior with charging is presented in the following. Changes of the absolute values are presented in table 6.1.

- The initial reversible increase of R with positive charging obeyed the same sign of charging coefficient as that of nanoporous gold and nanocriytalline platinum [1, 9, 2].
- Upon multiple cycling or increasing the charging voltage, sign inversion of the charging coefficient occurs (a local minimum of R is observed at a maximum of charging/voltage).
- This sign inversion is reversible, i.e. the sign of the charging coefficient can be tuned by means of the applied potentials.

Table 6.1: Maximum observed resistance changes $\frac{\Delta R}{R_0}[\%]$

	$TUG-NPP_2$	$TUG-NPP_3$	$TUG-NPP_5$	$TUG-NPP_8$	$TUG-NCP_1$	$TUG-NCP_2$
partially removement of the “primary oxide”	43$\star$	28	-	-	-	-
oxygen + hydrogen atom chemisorption	-	-	-	-	20	-
pseudo capacitive charging (positive sign in $\frac{\Delta R}{R_0}$ vs. ΔQ slope)	-	-	25	1	-	0.4
pseudo capacitive charging (negative sign in $\frac{\Delta R}{R_0}$ vs. ΔQ slope)	-	-	5	4.5	-	-

$\star$... Removal of the “primary oxide” revealed impressive alterations in resistance of $40\ \%$ before sample cracking, even through only a fraction of the latter was reduced

Comparison of the charging coefficient $\varrho = \frac{\Delta R}{R_0} \cdot \frac{A}{\Delta Q}$ determined for pseudo capacitive charging of nanoporous platinum in comparison to that of nanoporous gold from literature, revealed higher values in case of platinum. The latter might confirm the model that the resistivity of platinum is more sensitive to charging because of induced modifications in the scattering rate of conduction electrons into empty states of the d-band.

The introduction of the ratio

$$\vartheta = \frac{\left(\varrho_{size.ind}\right)_{capacitive\ charging\ only}}{\left(\varrho_{size.ind}\right)_{chemisorption}}$$

revealed higher values in case of NPP-samples compared to NCP-samples and in the case of NPG compared to gold thin films. This was shown to be possibly contrary to the interpretation in [1] that charge induced resistance changes by means of capacitive charging and chemisorption originate primarily from alterations in the scattering rate at the surface.

In addition to the charge-induced resistance variations which was the primary focus of the present work, initial studies on charge-induced variations of the magnetic moment were performed. Moreover, initial tests in order to perform the dealloying with ionic liquids were performed.

Appendix A

Initial studies of magnetic behavior of nanoporous platinum in dependence of electrochemical charging

A.1 Principle of tuning the Magnetization of platinum

Platinum is a paramagnetic metal. The main contribution to its magnetic moment results from the conduction electrons in the d-Band [64]. Because of this, the magnetic moment can be described using the model of Pauli-paramagnetism.
In a metal the conduction electrons can be described by the *free electron model* [65]. For both possible electron spin configurations ($m_z = \pm\frac{1}{2}$) there are two degenerated states of the same (kinetic) energy. Applying an external magnetic field H, changes the situation. The density of states for this model is shown in figure A.1 with and without an external magnetic field. Depending on their prior spin orientation, this field causes a de- or increase in energy of the electronic states in the *free-electron-model*.

$$\Delta E = \pm\mu_0\mu_B H \tag{A.1}$$

Here μ_B labels the Bohr-magneton, the magnetic moment of a single electron [66]. The energy difference between both subbands (electron states with either $m_z = +\frac{1}{2}(\uparrow)$ or $m_z = -\frac{1}{2}(\downarrow)$) is $2\mu_0\mu_B H$ and the magnetization results from their different occupation.

$$M_{Pauli} = \mu_B(n_\uparrow - n_\downarrow) \tag{A.2}$$

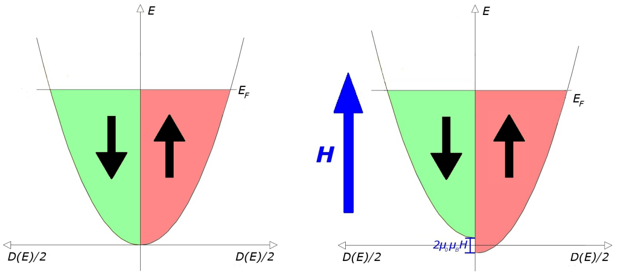

(a) H=0 (b) H>0

Figure A.1: *Free electron model* density of states $D(E)$, without and with external magnetic field H [68]

In the case of low temperatures ($k_B T \ll E_F$), $n_\uparrow$ and $n_\downarrow$ can be approximated as follows [65]:

$$n_\uparrow = \frac{1}{2}\int_{-\mu_0\mu_B H}^{E_F} f(E)D(E+\mu_0\mu_B H)dE \cong \frac{1}{2}\int_0^{E_F} f(E)D(E)dE + \frac{1}{2}\mu_0\mu_B H D(E_F) \tag{A.3a}$$

$$n_\downarrow = \frac{1}{2}\int_{\mu_0\mu_B H}^{E_F} f(E)D(E-\mu_0\mu_B H)dE \cong \frac{1}{2}\int_0^{E_F} f(E)D(E)dE - \frac{1}{2}\mu_0\mu_B H D(E_F) \tag{A.3b}$$

$f(E)$ stands for the Fermi-Dirac-distribution. Taking into account equations A.2 and A.3, the magnetization can be computed using:

$$M_{Pauli} = D(E_F)\mu_0\mu_B^2 H \tag{A.4}$$

Because of interactions between the electrons (molecular field energy in the magnetic field resulting from their own magnetization), described in more detail in [66], this is not the whole story. The so called Stoner enhancement leads to:

$$M = \frac{D(E_F)\mu_0\mu_B^2 H}{1-UD(E_F)} = \frac{M_{Pauli}}{1-UD(E_F)} = C_{stoner}\cdot M_{Pauli} \tag{A.5}$$

U[1] labels the interaction constant. $M > M_{Pauli}$ and C_{stoner} has a value of 3.7 [64].

The magnetization depends strongly on the density of states at the Fermi level. A lower $D(E_F)$ leads to a lower magnetization and reverse. Alternating the electron density might lead to measurable changes in magnetization.

The magnetization is derived from the magnetic moment m of the sample via several normalizations [67]. For example the volume of the sample $M_V = \frac{m}{cm^3}$, its weight $M_g = \frac{m}{g}$, number of moles $M_{mol} = \frac{m}{mol}$ or as derived due to the number of atoms $M_{atom} = \frac{m}{\text{number of atoms}}$, as done in this thesis.

---

[1] $U = \mu_0\mu_B^2\lambda$; λ describes the proportionality factor of the identical mean field, influencing all spins, in *molecular field theory*.

A.2 Procedure of magnetic measurements in dependence of electrochemical charging

Motivated by the idea that variations in electron density may lead to a change of the magnetic moment m of the sample, as described in chapter A.1, measurements of the magnetic moment in dependence of charging were performed by means of SQUID-magnetometry. SQUID measurements were performed at the University Graz using a *Quantum Design - MPMS XL7*.
The sample $KIT - NPP_1$ (see section 3.1 for further information) was used for investigations in the magnetic studies.
For SQUID-measurements a small electrochemical cell was designed as described in the Master's thesis of Topolovec [68] using NPP as WE (figure A.2). Because of limited space in the SQUID, no RE could be placed in this electrochemical cell. With the lack of a RE it is not possible to measure the potential of the WE and to control associated chemical processes. To somehow get an idea of the reactions that take place, investigations in three electrode geometry had to be done first to characterize the behavior for two electrode geometry, which is described in more detail in the thesis of Topolovec [68]. For pure platinum it turned out, that applied potentials of $1250\,\text{mV}$ and $-450\,\text{mV}$ in two electrode geometry correspond to approximately $200\,\text{mV}$ and $-300\,\text{mV}$, in three electrode geometry, using a saturated Ag/AgCl RE and again 1-M KOH as electrolyte[2]. These values are more or less as a rule of thumb, and slight variations are also reported by Topolovec [68]. Nevertheless applying these potentials should cover the regime of adsorption and desorption of oxygen species.

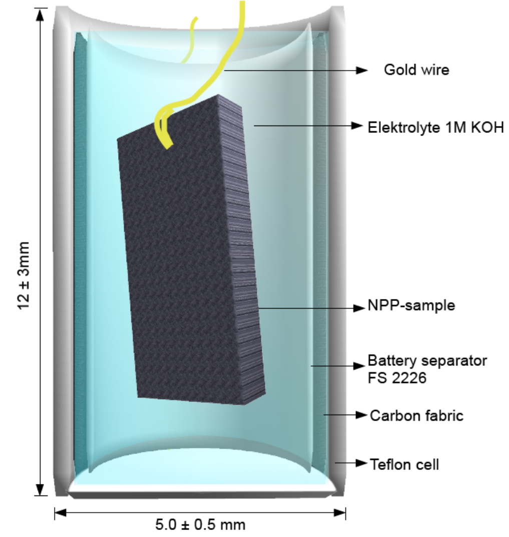

Figure A.2: Electrochemical cell with $KIT - NPP_1$ as working electrode used for SQUID-measurements

---

[2] $200\,\text{mV}$ and $-300\,\text{mV}$ vs. saturated Ag/AgCl $\approx 1250\,\text{mV}$ and $750\,\text{mV}$ versus RHE

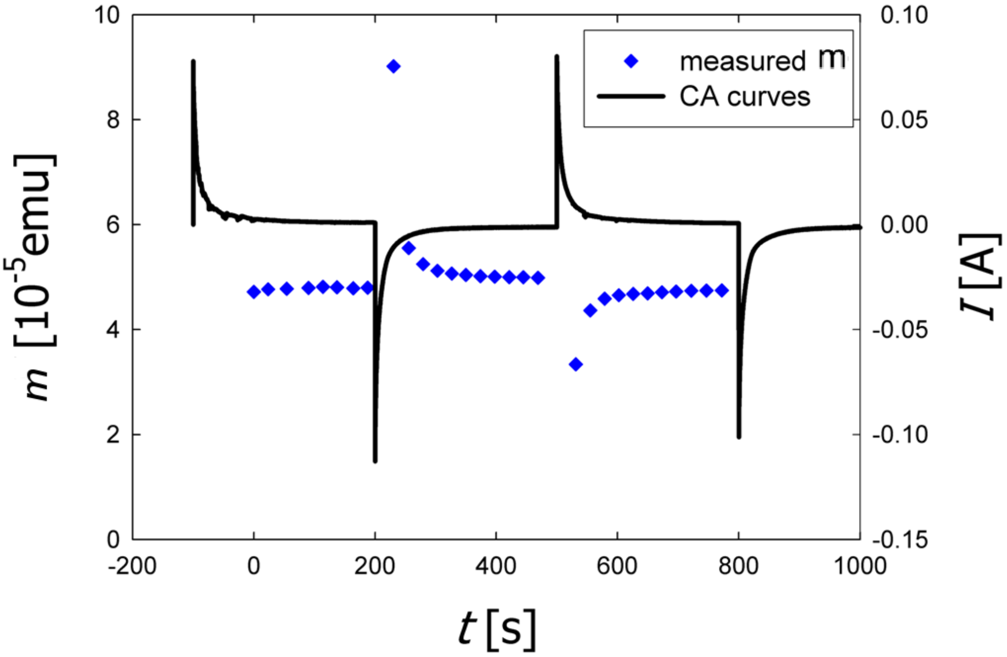

Figure A.3: Current influence on magnetic moment measurements (external field: H= 500 Oe).

A.3 Results of magnetic measurements in dependence of electrochemical charging

The experimental procedure of these measurements is described in chapter A.2. A current influence on the magnetic moment m during amperometric measurements, applied in two electrode geometry, seems to become obvious from figure A.4. Nevertheless, subsequent evaluation via plots of the magnetic moment divided by corresponding current absolute values versus time ($\frac{m}{|I|}$ $vs.$ t) did not reveal a constant behavior, which is in contradiction to the assumption that only a current effect $m \propto I$ had been measured. The question of possible current effects and other influences is discussed in more detail in [68]. To exclude current effects (due to CA measurements), the WE had been disconnected from the potentiostat before m was recorded. After applying alternating potentials of $-450\,\mathrm{mV}$ and $1250\,\mathrm{mV}$ for five minutes, m was measured three times. The results are presented in figure A.4. The first measurements seemed to lead to reproducible m alterations because mean values obtained for the three measurements recorded after charging are twice the differential sensitivity of the SQUID, reported to be 10^{-8} emu in the *Quantum Design* reference chart. The big fluctuations measured after the WE had been disconnected for the last time, after five minutes of charging at $-400\,\mathrm{mV}$, makes serious interpretations impossible. To recapitulate, no reproducible change in the magnetic moment could be measured in the case of sample $KIT-NPP_1$. It should be mentioned that the charge according to the recorded CA curves decreased during the whole day and the measurements presented in figure A.4 were recorded in the end. A high brittleness was also observed in the NPP samples fabricated at the KIT. For this reason subsequent attempts to rebuild the cell described above failed and $KIT - NPP_1$ remained the only investigated NPP sample for SQUID measurements.

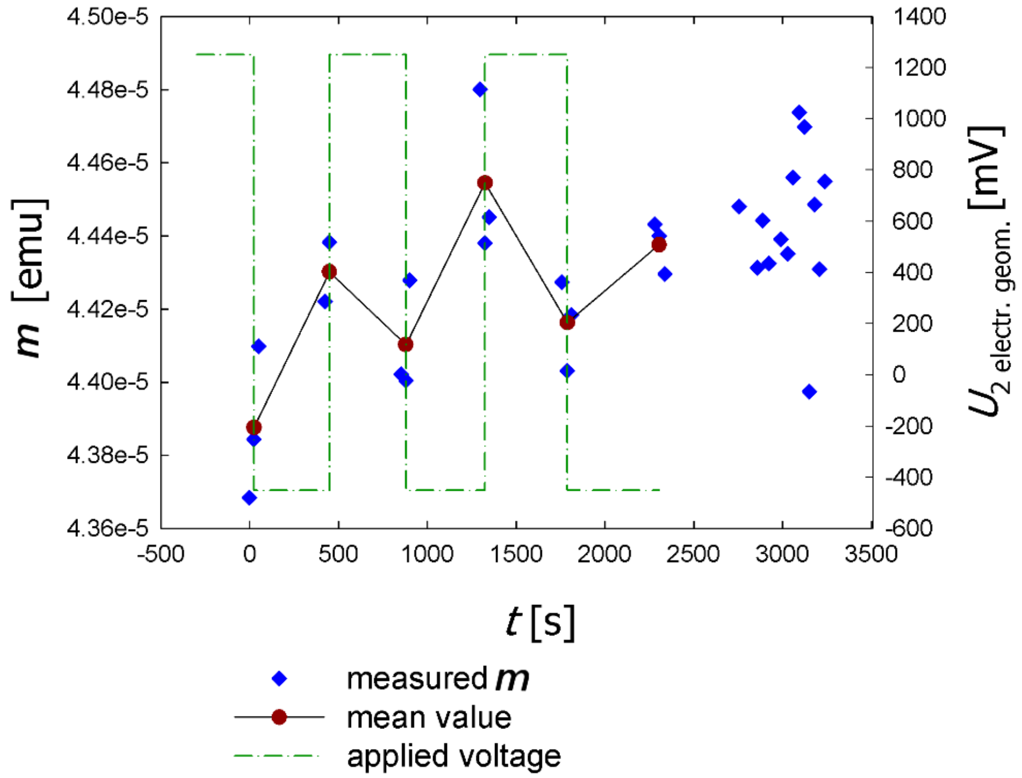

Figure A.4: m measurements after five minutes of preceding charging ($H = 500\ Oe$)

A.4 Discussion of magnetic measurements in dependence of electrochemical charging

Magnetic moment measurements presented in chapter A.3 do not exhibit reliable and reproducible correlations between the measured magnetic moment and applied voltages (corresponding to sample's charging). This section discusses expectable magnetization alterations, by a model derived in the dissertation of Drings.

Electrochemical charging lead to alterations of sample's charge density in the space-charge-region (see chapter 2.7.1), resulting in changes of the Fermi-level and therefore in variations of the DOS at the Fermi level $D(E_F)$, which is shown below. Using the *core-shell-model* shown in figure 5.1 and equation 5.1 to calculate the transferred charge per atom in the space-charge-region, the corresponding local shift of the Fermi-level ΔE is obtained by:

$$\Delta q_{scr} = -e \int_{E_F}^{E_F + \Delta E} D(E) dE. \tag{A.6}$$

Taylor expanding (linear approximation) D(E) around E_F gives:

$$D(E_F + \Delta E) \approx D(E_F) + \frac{dD(E)}{dE}(E_F) \cdot \Delta E. \tag{A.7}$$

Plugging equation A.6 into A.7 results in:

$$\Delta q_{scr} \approx e \cdot \left[D(E_F) \cdot \Delta E^2 + \frac{1}{2}\frac{dD(E)}{dE}(E_F)\Delta E \right] \approx -e \cdot D(E_F) \cdot \Delta E \Rightarrow \Delta E = \frac{\Delta q_{scr}}{-eD(E_F)}. \tag{A.8}$$

The last step's simplification is qualified because $\Delta E_F^2 \ll \Delta E$. To calculate the charge per atom in the space-charge-region by equation 5.1 the sample mass was estimated as follows[3]. As mentioned in chapter 3.1.1 the $KIT - NPP$-samples were about five times smaller than the $TUG - NPP$ samples ($\approx$ 140 mg). The starting alloys consisted of three times more copper than platinum atoms but because a platinum atom is about three times heavier ($\frac{M_{mol-Pt}}{M_{mol-Cu}} = 3.07$), dealloying the entire copper fraction halves the alloy's weight. Hence the weight of sample $KIT - NPP_1$, was estimated by $140 \cdot \frac{1}{5} \cdot \frac{1}{2} = 14$ mg. During the five minute CA curves of figure A.4, a charge of approximately ± 0.6 As was transfered. Assuming a value of $\omega = 1$ discussed in chapter 2.7.1, equation A.8 leads to a shift in the Fermi-level of

$$\Delta E_F = E_F - E_{F0} \approx \pm 0.0456 \text{ eV}.$$

Using equation A.7 a shift in the DOS of

$$\Delta D(E_F) = D(E_F) - D(E_{F0}) \approx \pm 0.2752 \, \frac{1}{\text{eV} \cdot atom}$$

was computed. According to the model used, positive charging ($\Delta Q > 0$), for example, leads to a depletion of electrons in the space-charge-region and hence to a decline of the Fermi level E_F. Consistent with the shape of the DOS shown in figure 2.8, the DOS at the Fermi level $D(E_F)$ increases due to a declinating Fermi level. As described in chapter A.1, alterations of $D(E_F)$ should change the sample's magnetic moment. Calculations (estimations) of possible alterations in the magnetic moment of sample $KIT - NPP_1$ the values for ΔE_F and $\Delta D(E_F)$ given above can be found in section A.5. Although the model of Drings revealed an unrealistic change in the relative magnetization ΔM_{atom} of more than 80 % (eqation A.11), only an alteration in the magnetic moment of $\Delta m \approx 9 \cdot 10^{-11}\, emu$ (equation A.12) was obtained. Such slight variations can not be resolved in our experiment as mentioned in chapter A.3 which would explain the inconclusiveness in figure A.4 [4]. Even assuming a charge ΔQ four times larger than before resulted in the same order of magnitude of Δm.

Regarding the above discussion, much higher external fields H and samples containing more

---

[3] This strange approximation becomes necessary because weight measurements were not executed for the NPP samples due to the danger of the sample cracking.

[4] Apart from this, the behaviour of the mean values after charging presented in this figure is contrary to the described model.

NPP-material seem to be required to detect alterations in the magnetic moment m. Questions of the magnetic moments of oxides formed during charging, or the chemical processes after disconnecting the sample from the potentiostat for m measurement, have also not been discussed here.

A.5 Additional calculations of chapter A.4

Values used for the calculation of properties according to sample $KIT-NPP_1$:

$N_A = 6.02214179 \cdot 10^{23}$...Avogadro constant
$M_{mol-Pt} = 195.08\ [\frac{g}{mol}]$...molar mass of platinum
$\mu_0 = 12.566370 \cdot 10^{-7}\ [\frac{H}{m}]$...vacuum permeability;
$\mu_B = 9.274 \cdot 10^{-24}\ [\frac{J}{T}]$...Bohr magneton;
$m_{sample} = 14 * 10^{-3}\ [g]$...estimated sample mass
$w = 1$...affected material (1 means 100 %)
$H = 500 \cdot 79.577\ [\frac{A}{m}]$...external magnetic field
$\Delta Q = 0.6\ [As]$...Charge transfered during a CA at 1250 mV in figure A.4
$q_e = -1.6022 \cdot 10^{-19}\ [As]$...electron charge
$C_{stoner} = 3.7$...Stoner enhancement factor of platinum [64]
$D(E_F) = 1.908\ [\frac{states}{\text{eV}\ atom}]$...DOS at the Fermi level [46]
$\frac{dD_E}{dE}(E_F) = -12.12\ [\frac{states}{\text{eV}^2\ atom}]$...derivative of the DOS at the Fermi level [46]

After calculating the transfered charge in terms of atoms comprised in the surface-charge-region Δq_{scr} by equation A.6, ΔE_F was calculated using equation A.8. Note that plugging in $q_{scr}\ [As]$ and $D(E_F)\ [\text{eV}]$ led to a shift in ΔE_F in $[\text{eV}]$,

$$\Delta E_F = E_{F-charged} - E_F \approx -0.0456\,\text{eV}.$$

Afterward the resulting “new” $D(E_F)_{charged}$ was calculated by the use of equation A.7,

$$\Delta D(E_F) = D(E_F)_{charged} - D(E_F) \approx 0.2752\ \frac{1}{\text{eV} \cdot atom}.$$

Acording to equation A.5, changes in the magnetization and hence the magnetic moment have been estimated as follows.

$$M_0 = C_{stoner} \cdot H \cdot \mu_B^2 \cdot \mu_0 \cdot D(E_F) \tag{A.9a}$$

$$M_{charged} = C_{stoner} \cdot H \cdot \mu_B^2 \cdot \mu_0 \cdot D(E_F)_{charged} \tag{A.9b}$$

$$\frac{\Delta M}{M_0} = \frac{M_{charged} - M_0}{M_0} \cdot 100 = 14.4239\ \% \tag{A.10}$$

$$\text{Atoms in the surface-charge-layer} = atom_{scr} = \frac{\omega \cdot m_{sample} \cdot N_A}{M_{mol-Pt}} \tag{A.11}$$

$$\Delta m = (M_{charged} - M_0) \cdot atom_{scr} \cdot \frac{1}{79.577} \approx 1.5 \cdot 10^{-11}\ emu \tag{A.12}$$

Note that according to equation A.5, C_{stoner} depends on the $D(E_F)$ too.

$$C_{stoner} = \frac{1}{1 - U \cdot D(E_F)} \Rightarrow U = \frac{-1 \cdot C_{stoner}}{C_{stoner} \cdot D(E_F)} \tag{A.13}$$

Taking into account $C_{stoner} = 3.7$ [64] and $D(E_F) = 1.908\ \frac{states}{atom}$ [46] the second part of equation A.13 yields a value of $U = 0.383$ eV. Estimating that $U = constant$, and does not depend on the DOS at the Fermi level $D(E_F)$, alterations of the latter result in the new Stoner enhancement factors C_{stoner}. With the approximation given above and $\Delta D(E_F) \approx 0.2752$ eV^{-1} a higher value of C_{stoner} is obtained:

$$C_{stoner-charged} \approx 1.7 \cdot C_{stoner}.$$

This new stoner enhancement factor also leads to new values of the change in magnetization[5] and magnetic moment.

$$\frac{\Delta M}{M_0} = 84.4\,\% \tag{A.14}$$

$$\Delta m \approx 10 \cdot 10^{-11}\,emu \tag{A.15}$$

---

[5] Such high values seem unrealistic and must be assigned to the oversimplifications of the described model.

Appendix B

Additional information and data according to resistance measurements

B.1 Additional plots for chapter 4.2.2

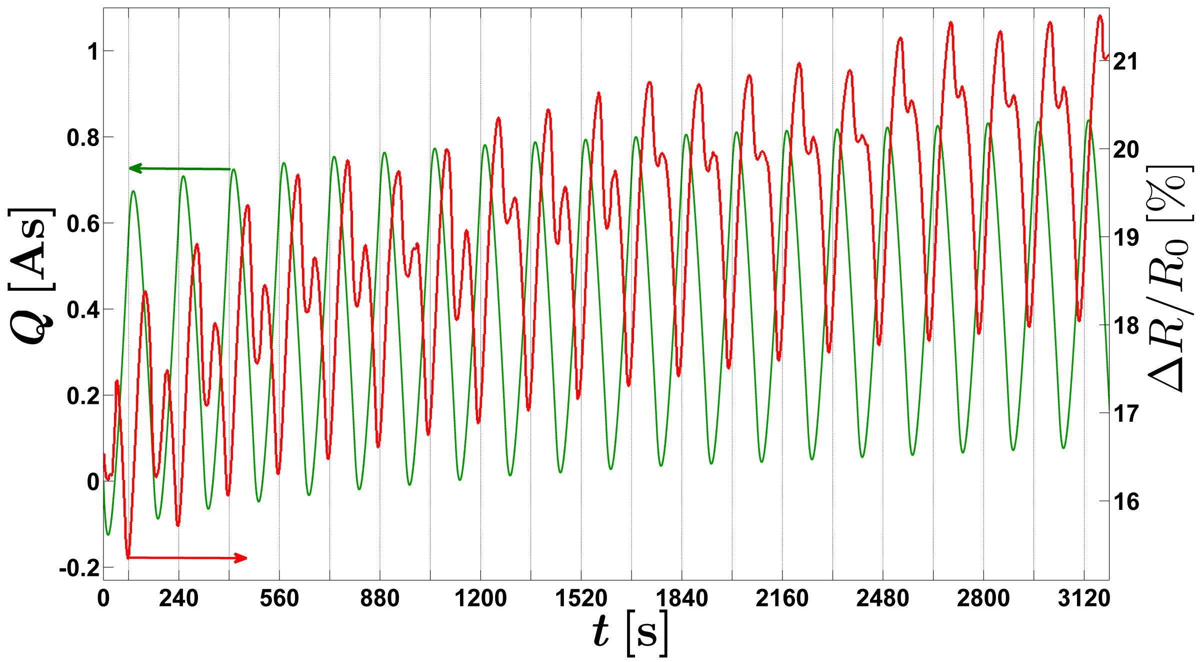

Figure B.1: $TUG-NPP_5$ $R_0 = 1.339\,\Omega$. Complete plot of the excerpts shown in figure 4.16. Charge and resistance changes during the second CV recorded for this sample. The vertical lines mark the times at which the potential reached its maximum value Pot_h.

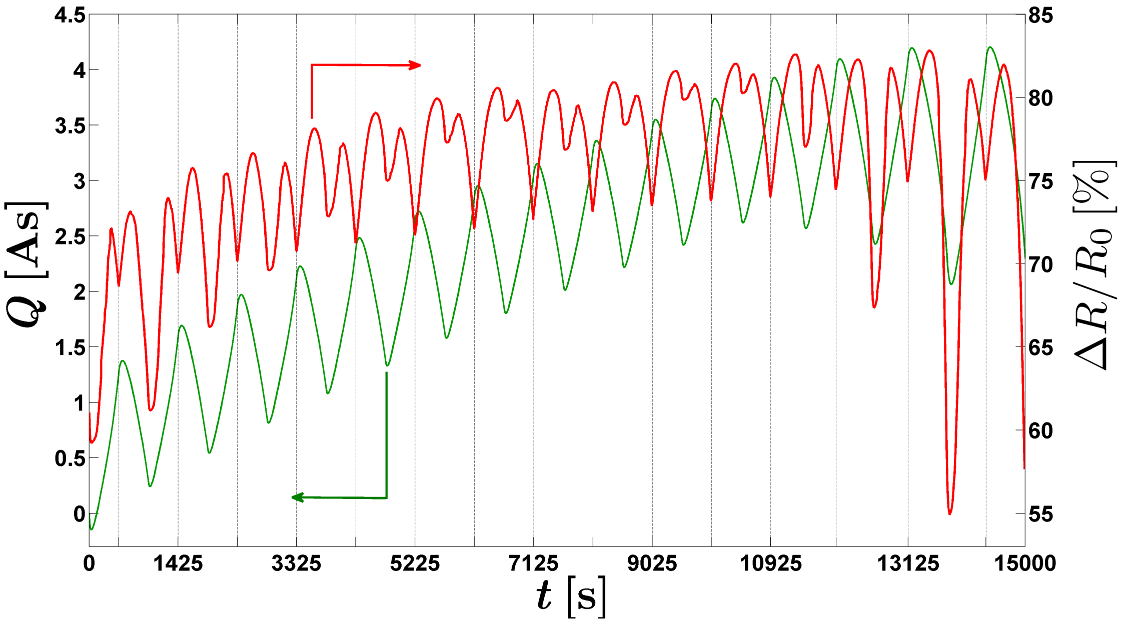

Figure B.2: Sample $TUG-NPP_5$, $R_0 = 1.339\ \Omega$. Additional plot for figure 4.17.Resistance and charge time dependence during a CV recorded (with decreasing Pot_l value for the last four cycles). The vertical lines mark the times at which the potential reached its maximum value Pot_h.

B.2 Additional plots for chapter 4.2.3

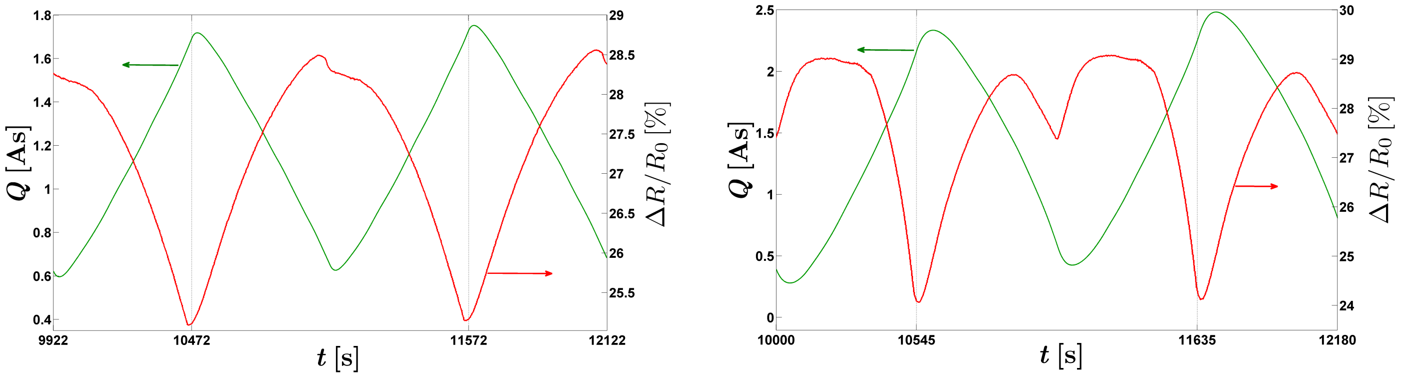

(a) Electrolyte 1-M KCL, pH=7. 10^{th} and 11^{th} cycle

(b) Electrolyte 1-M KOH (as usual), pH=14.10^{th} and 11^{th} cycle

Figure B.3: $TUG-NPP_8$, $R_0 = 2.024\ \Omega$. Excerpts of the time response during a CV, details in figure 4.21 and B.4.

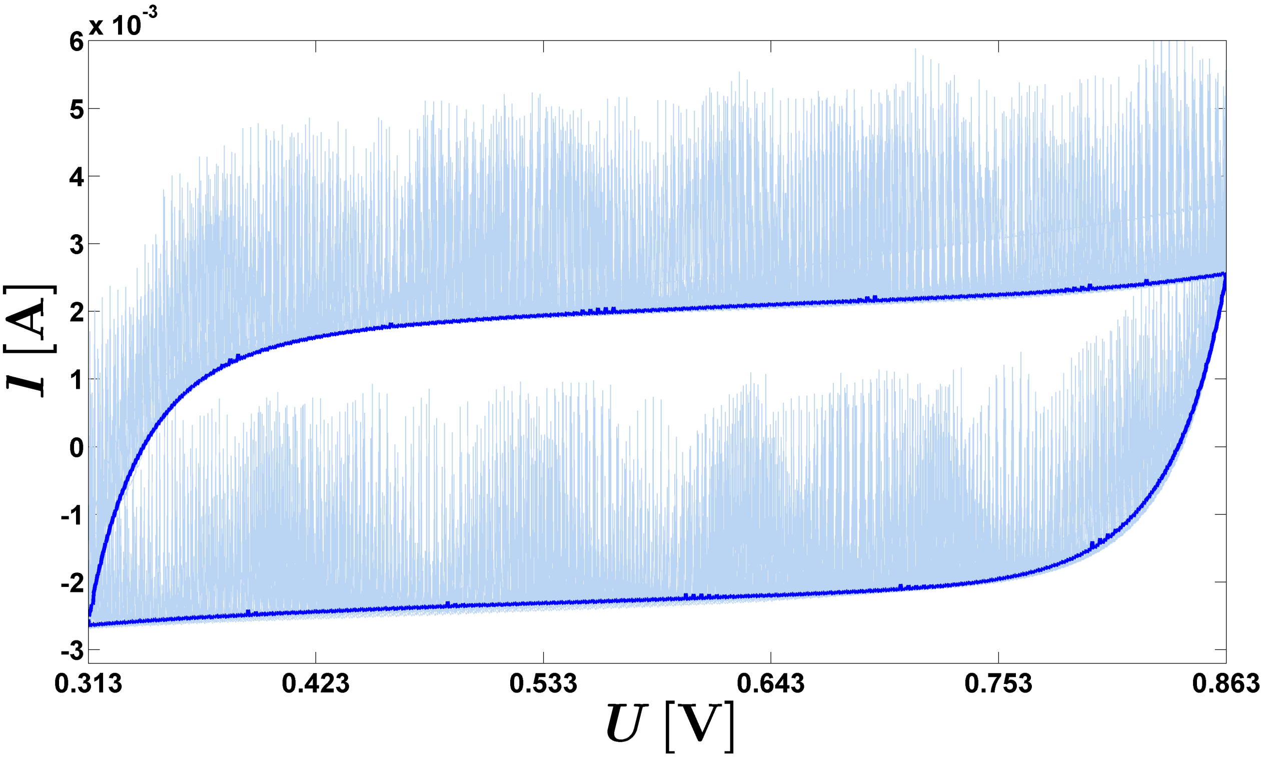

Figure B.4: $TUG - NPP_8$ Complete CV of the sequence presented in figure 4.21a, and, figure B.3a. The dark blue line designates the 8^{th} cycle without the additional peaks resulting from resistance measurements.

B.3 Resistance correction for the TUG-NCP-samples

The specimen holder used for the $TUG - NCP$-samples did not enable the positioning of a fifth wire on the sample in between the sensing wires, see chapter 2.5. As a consequence of this, the potentiostat had to be connected with one of the two outward wires, which lead to asymmetric currents through the sample and hence an additional voltage drop between the sensing wires. This affects the resistance measurement, especially in the case of high currents into the potentiostat and a low sample resistance. The principle is sketched in figure B.5. After the resistance changes during a CV were observed to depend primarily on the connection with the potentiostat (to which of the outward wires), the following correction of measured resistance values was derived. The notation is consistent with figure B.5.

$$I_3 = I_1 + I_2 \tag{B.1}$$

The current I_1 was $100\,\mathrm{mA}$ predetermined by the resistance measurement equipment, and I_2 is the additional current into the potentiostat.

$$R_{measured} = \frac{U_m}{I_1} = \frac{R_{real} I_3}{I_1} = \frac{R_{real}(I_1 + I_2)}{I_1} \Rightarrow R_{real} = R_{measured}\frac{I_1}{(I_1 + I_2)} \tag{B.2}$$

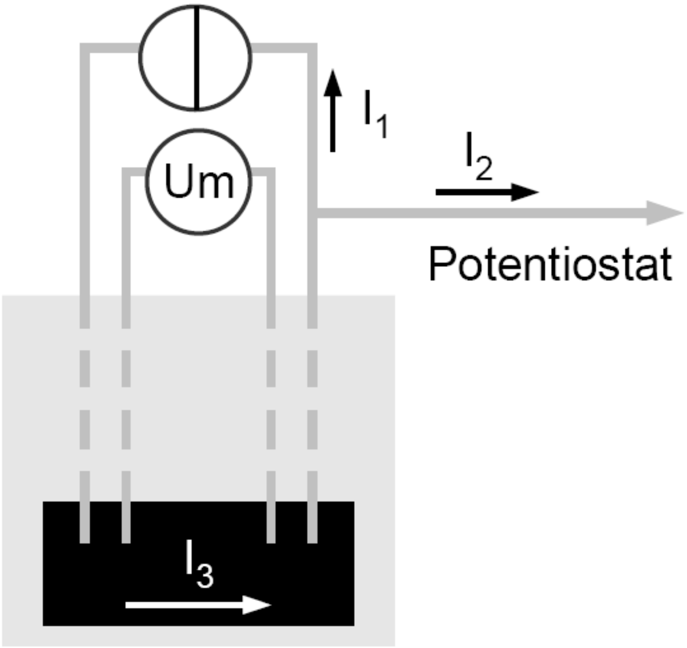

Figure B.5: Draft to explain the impact of currents into the potentiostat, on the resistance measurement

Or better,

$$R_{real} = R_{measured} \frac{I_1}{(I_1 + c_{geometry} \cdot I_2).} \tag{B.3}$$

$c_{geometry}$ was introduced to factor in the fact, that the additional current I_2 originates from reactions at the whole sample surface. Hence I_2 flows not exclusively through samples component between the sensing wires. This was not considered in equation B.1. $c_{geometry} = 0.5$ have been used in this master thesis, which should only be considered as a ruff estimation out of desperation.

The correction, equation B.3, of measured resistance values made the resistance measurements comprehensible (and even possible in case higher currents into the potentiostat), but a complete independence from both possible connections with the potentiostat, have not been accomplished. Nevertheless, using low currents (CA curves instead of a “fast” CV) and the application of the presented correction should yield reasonable results, even for small resistance changes.

Bibliography

[1] P. Wahl, T. Traussnig, S. Landgraf, H.-J. Jin, J. Weissmueller, R. Wuerschum. Adsorption-driven tuning of the electrical resistance of nanoporous gold. *JOURNAL OF APPLIED PHYSICS* **108** (2010).
doi:10.1063/1.3490789

[2] M. Sagmeister, U. Brossmann, S. Landgraf, R. Wuerschum. Electrically tunable resistance of a metal. *PHYSICAL REVIEW LETTERS* **96** (2006) 156601/1

[3] H. Gleiter, J. Weissmuller, O. Wollersheim, R. Wurschum. Nanocrystalline materials: A way to solids with tunable electronic structures and properties? *ACTA MATERIALIA* **49** (2001) 737

[4] J. Weissmuller, R. N. Viswanath, D. Kramer, P. Zimmer, R. Wurschum, H. Gleiter. Charge-Induced Reversible Strain in a Metal. *SCIENCE* **300** (2003) 312.
doi:10.1126/science.1081024

[5] R. N. Viswanath, D. Kramer, J. Weissmueller. Adsorbate effects on the surface stress-charge response of platinum electrodes. *ELECTROCHIMICA ACTA* **53** (2008) 2757.
doi:10.1016/j.electacta.2007.10.049

[6] H.-J. Jin, X.-L. Wang, S. Parida, K. Wang, M. Seo, J. Weissmueller. Nanoporous Au-Pt Alloys As Large Strain Electrochemical Actuators. *NANO LETTERS* **10** (2010) 187.
doi:10.1021/nl903262b

[7] H. Drings. *Nanoskalige Materialien mit durstimmbaren Eigenschaften*. Dissertation, Karlsruhe Institute of Technology, 2004

[8] R. Tucceri. A review about the surface resistance technique in electrochemistry. *SURFACE SCIENCE REPORTS* **56** (2004) 85.
doi:10.1016/j.surfrep.2004.09.001

[9] M. Sagmeister. *Tuneable properties of nano-scale metals*. Diplomarbeit, TU Graz, 2005

[10] J. Erlebacher. An atomistic description of dealloying - Porosity evolution, the critical potential, and rate-limiting behavior. *JOURNAL OF THE ELECTROCHEMICAL SOCIETY*

151 (2004) C614.
doi:10.1149/1.1784820

[11] J. Erlebacher, M. Aziz, A. Karma, N. Dimitrov, K. Sieradzki. Evolution of nanoporosity in dealloying. *NATURE* **410** (2001) 450

[12] P. Wahl. *Tunable electrical resistance of nanoporous gold.* Diplomarbeit, Technische Universität Graz Betreuer Univ.-Prof. Dr.rer.nat Roland Würschum Institut für Materialphysik Graz, Juli, 2010

[13] C. E. Mortimer. *Das Basiswissen der Chemie in Schwerpunkten.* Georg Thieme Verlag Stuttgart . New York, 1983

[14] C. H. Hamann, W. Vielstich. *Elektrochemie*, Band 3. WILEY-VCH, 1998

[15] B. Conway. Electrochemical oxide film formation at noble-metals as a surface-chemical process. *PROGRESS IN SURFACE SCIENCE* **49** (1995) 331

[16] G. Jerkiewicz, G. Vatankhah, J. Lessard, M. Soriaga, Y. Park. Surface-oxide growth at platinum electrodes in aqueous H_2SO_4 - Reexamination of its mechanism through combined cyclic-voltammetry, electrochemical quartz-crystal nanobalance, and Auger electron spectroscopy measurements. *ELECTROCHIMICA ACTA* **49** (2004) 1451.
doi:10.1016/j.electacta.2003.11.008. 197th Meeting of the Electrochemical-Society, Toronto, CANADA, MAY, 2000

[17] S. Trasatti, O. Petrii. Real surface-area measurements in electrochemistry. *JOURNAL OF ELECTROANALYTICAL CHEMISTRY* **327** (1992) 353

[18] M. E.I.Khrushcheva. Electrochemical Determination of Surface Area of Metals. *RUSSIAN CHEMICAL REVIEWS* **47** (1978) 416

[19] H. Binder, A. Köhling, K. Metzelthin, G. Sandstede, M.-L. Schrecker. Elektrochemische Bestimmung der spezifischen Oberfläche und der Aktivität von porösem Platin. *CHEMIE INGENIEUR TECHNIK* **40** (1986) 586.
doi:10.1002/cite.330401208

[20] W. T. Kessler, A.M.Castro Lura, A. Arvia. The behaviour of platinized platinum electrodes in acid solutions: correlation between voltammetric data and electrode structure. *JOURNAL OF APPLIED ELECHTROCHEMISTRY* **16** (1986) 693.
doi:10.1007/BF01006921

[21] D. A. Jones. *Principles and Prevention of Corrosion.* Prentice Hall, 1995

[22] D. Pugh, A. Dursun, S. Corcoran. Formation of nanoporous platinum by selective dissolution of Cu from Cu0.75Pt0.25. *JOURNAL OF MATERIALS RESEARCH* **18** (2003) 216

[23] D. Pugh, A. Dursun, S. Corcoran. Electrochemical and morphological characterization of Pt-Cu dealloying. *JOURNAL OF THE ELECTROCHEMICAL SOCIETY* **152** (2005) B455. doi:10.1149/1.2048140

[24] D. Pugh. *Nanoporous Platinum.* Dissertation, State University Virgina, 2003

[25] H.-J. Jin, S. Parida, D. Kramer, J. Weissmueller. Sign-inverted surface stress-charge response in nanoporous gold. *SURFACE SCIENCE* **602** (2008) 3588. doi:10.1016/j.susc.2008.09.038

[26] J. Huang, I. Sun. Fabrication and surface functionalization of nanoporous gold by electrochemical alloying/dealloying of Au-Zn in an ionic liquid, and the self-assembly of L-cysteine monolayers. *ADVANCED FUNCTIONAL MATERIALS* **15** (2005) 989. doi:10.1002/adfm.200400382

[27] L. Lee, D. He, A. G. Carcea, R. C. Newman. Exploring the reactivity and nanoscale morphology of de-alloyed layers. *CORROSION SCIENCE* **49** (2007) 72. doi:10.1016/j.corsci.2006.05.005. International Symposium on Progress in Corrosion Research, Sapporo, JAPAN, SEP 14-16, 2005

[28] S. Van Petegem, S. Brandstetter, R. Maass, A. M. Hodge, B. S. El-Dasher, J. Biener, B. Schmitt, C. Borca, H. Van Swygenhoven. On the Microstructure of Nanoporous Gold: An X-ray Diffraction Study. *NANO LETTERS* **9** (2009) 1158. doi:10.1021/nl803799q

[29] L. Spiess, G. Teichert, R. Schwarzer, H. Behnken, C. Genzel. *Moderne Röntgenbeugung*, Band 2. Vieweg+Teubner, 2008

[30] Y. Sun, K. Kucera, S. Burger, T. Balk. Microstructure, stability and thermomechanical behavior of crack-free thin films of nanoporous gold. *SCRIPTA MATERIALIA* **58** (2008) 1018

[31] J. Biener, A. Hodge, A. Hamza, L. Hsiung, J. Satcher. Nanoporous Au: A high yield strength material. *JOURNAL OF APPLIED PHYSICS* **97** (2005). doi:10.1063/1.1832742

[32] A. Hodge, J. Biener, L. Hsiung, Y. Wang, A. Hamza, J. Satcher. Monolithic nanocrystalline Au fabricated by the compaction of nanoscale foam. *JOURNAL OF MATERIALS RESEARCH* **20** (2005) 554. doi:10.1557/JMR.2005.0081

[33] A. M. HODGE, J. BIENER, J. R. HAYES, P. M. BYTHROW, C. A. VOLKERT, A. V. HAMZA. Scaling equation for yield strength of nanoporous open-cell foams. *ACTA MATERIALIA* **55** (2007) 1343.
doi:10.1016/j.actamat.2006.09.038

[34] G. GUPTA, D. A. SLANAC, P. KUMAR, J. D. WIGGINS-CAMACHO, X. WANG, S. SWINNEA, K. L. MORE, S. DAI, K. J. STEVENSON, K. P. JOHNSTON. Highly Stable and Active Pt-Cu Oxygen Reduction Electrocatalysts Based on Mesoporous Graphitic Carbon Supports. *CHEMISTRY OF MATERIALS* **21** (2009) 4515.
doi:10.1021/cm901203n

[35] A. RUBAN, H. SKRIVER, J. NORSKOV. Surface segregation energies in transition-metal alloys. *PHYSICAL REVIEW B* **59** (1999) 15990

[36] M. YUGUANG, P. BALBUENA. Pt surface segregation in bimetallic Pt/sub 3/M alloys: a density functional theory study. *SURFACE SCIENCE* **602** (2008) 107

[37] Y. SHEN, D. OCONNNOR, K. WANDELT, R. MACDONALD. Studies of srface-composition and structure of Cu3Pt(111) by low-energy Alkaliion-scattering. *SURFACE SCIENCE* **328** (1995) 21

[38] Y. GAUTHIER, A. SENHAJI, B. LEGRAND, G. TREGLIA, C. BECKER, K. WANDELT. An unusual composition profile: a LEED-TBIM study of Pt25Cu75(111). *SURFACE SCIENCE* **527** (2003) 71.
doi:10.1016/S0039-6028(03)00008-6

[39] H.-J. JIN, D. KRAMER, Y. IVANISENKO, J. WEISSMULLER. Macroscopically strong nanoporous pt prepared by dealloying. *ADVANCED ENGINEERING MATERIALS* **9** (2007) 849.
doi:10.1002/adem.200700177

[40] B. PREDEL. *Landolt-Börnstein - Group IV Physical Chemistry Numerical Data and Functional Relationships in Science and Technology Ag-Au (Silver - Gold)*, Band 12A: Ac-Ag ... Au-Zr.
doi:10.1007/10793176_17

[41] B. PREDEL. *Landolt-Börnstein - Group IV Physical Chemistry Numerical Data and Functional Relationships in Science and Technology Cu-Pt (Copper-Platinum)*, Band 5d: Cr-Cs 2̌013 Cu-Zr.
doi:10.1007/10086090_1106

[42] W. SCHMICKLER. *Grundlagen der Elektrochemie*. Vieweg, 1996

[43] R. WÜRSCHUM. Personal reference, 2011

[44] S. Haussener, C. Suter. CT-based determination of effective transport properties for porous media, 2010. Http://www.pre.ethz.ch/research/projects/?id=comptom

[45] R. Tucceri, D. Posadas. The effect of surface-charge on the surface conductance of silver in surface inactive electrolytes. *JOURNAL OF ELECTROANALYTICAL CHEMISTRY* **283** (1990) 159

[46] F. Müller, J. Garland, M. Cohen, K. Benneman. Quadratic integration - Theory and application to electronic structure of platinum. *ANNALS OF PHYSICS* **67** (1971) 19

[47] M. Fujihira, T. Kuwana. Studies of electrochemical interfaces of thin Pt film electrodes by surface conductance. *ELECTROCHIMICA ACTA* **20** (1975) 565

[48] P. Wissman. Effects of gas adsorption on conductivity of thin metal-films. *THIN SOLID FILMS* **13** (1972) 189

[49] S. Landgraf. e-mail, 2010

[50] A. K. Mishra, C. Bansal, H. Hahn. Surface charge induced variation in the electrical conductivity of nanoporous gold. *JOURNAL OF APPLIED PHYSICS* **103** (2008).
doi:10.1063/1.2912982

[51] H.-J. Jin. Privat communication

[52] B. Conway, G. Tremiliosifilho, G. Jerkiewicz. Independence of formation and reduction of monolayer surface oxide on Pt from presence of thicker phase-oxide layers. *JOURNAL OF ELECTROANALYTICAL CHEMISTRY* **297** (1991) 435

[53] M. Armand, F. Endres, D. R. MacFarlane, H. Ohno, B. Scrosati. Ionic-liquid materials for the electrochemical challenges of the future. *NATURE MATERIALS* **8** (2009) 621.
doi:10.1038/NMAT2448

[54] J.-F. Huang, B.-T. Lin. Application of a nanoporous gold electrode for the sensitive detection of copper via mercury-free anodic stripping voltammetry. *ANALYST* **134** (2009) 2306.
doi:10.1039/b910282e

[55] Y.-W. Lin, C.-C. Tai, I.-W. Sun. Electrochemical preparation of porous copper surfaces in zinc chloride-1-ethyl-3-methyl imidazolium chloride ionic liquid. *JOURNAL OF THE ELECTROCHEMICAL SOCIETY* **154** (2007) D316.
doi:10.1149/1.2724154

[56] F. Yeh, C. Tai, J. Huang, I. Sun. Formation of porous silver by electrochemical alloying/dealloying in a water-insensitive zinc chloride-1-ethyl-3-methyl imidazolium chloride

ionic liquid. *JOURNAL OF PHYSICAL CHEMISTRY B* **110** (2006) 5215.
doi:10.1021/jp0552527

[57] L. ZHONGHAO, J. ZHEN, L. YUXIA, M. TIANCHENG. Ionic liquids for synthesis of inorganic nanomaterials. *CURRENT OPINION IN SOLID STATE & MATERIALS SCIENCE* **12** (2009) 1

[58] S. LANDGRAF. Personal reference, 2010

[59] G. MANSUROV, O. PETRII, I. GLADKIKH, M. SURANOVA, V. SAFONOV. Study of adsorbtion phenomena by method of measurement of thin-film electrode electrical-resistance. *DOKLADY AKADEMII NAUK SSSR* **236** (1977) 153

[60] J. ELLIOTT, P. BIRKIN, P. BARTLETT, G. ATTARD. Platinum microelectrodes with unique high surface areas. *LANGMUIR* **15** (1999) 7411

[61] T. RICKER, E. PFLÜGER. Die temperaturabhängigkeit des Widerstandes und andere elektrische eigenschaften von Palladium-Silber- und Palladium-Rhodium-Legierungen. *ZEITSCHRIFT FUR METALLKUNDE* **57** (1966) 39

[62] A. SEEGER, G. SCHOTTKY. Energy and electrical resistivity of high-angle grain boundaries in metals. *ACTA METALLURGICA* **7** (1959) 495

[63] H. WINKES, D. SCHUMACHER, A. OTTO. Surface resistance measurements at the metal/-electrolyte interface of Ag(100) and Ag(111) thin film electrodes. *SURFACE SCIENCE* **400** (1998) 44

[64] S. MISAWA, K. KANEMATSU. 4d and 5d elementes, alloys and compounds - Magnetic susceptibility. *Band III-19a*, S. 500. Wijn, H. P. J., 1986.
doi:10.1007/10311893-73

[65] C. KITTEL. *Einführung in die Festkörperphysik.* Oldenburg, 2006

[66] M. GETZLAFF. *Fundamentals of Magnetism.* Springer, 2008

[67] M. MCELSFRESH. Fundamentals of magnetism andmagnetic measurements featuring Quantum Design's magnetic property measurement system, 1994

[68] S. TOPOLOVEC. *Magnetische Eigenschaften nanokristalliner Metalloxide unter elektrochemischer Beladung.* Diplomarbeit, TU-Graz, 2010

Acknowledgments

It is a pleasure to thank those who made this thesis possible. Many people supported me during this work, due to advice, supervision and fruitful discussions.

- I owe my deepest gratitude to Roland Würschum, not only for supervision of this master thesis. I would also like to thank him for making time to answer all of my questions, even if time was scarce, and his guidance during the last year
- Thomas Traußnig has made available his support in a number of ways. Starting from the introduction of the experimental procedures, supporting data evaluation and rendering assistance in the discussion of experimental data.
- Stefan Landgraf, for sample fabrication, advices according to chemical questions and giving me extra tuition about the wonderful world of electrochemistry.
- Stefan Topolovec, for his support on evaluation and interpretation the SQUID-measurements.
- Peter Parz, for assistance and advice in furnace processes.
- Patrick Wahl, preparing the ground for accurate resistance measurements in an electrolyte.
- Bernd Oberdorfer, for his support in operating the SEM in Leoben.
- Jörg Weissmüller (TU Hamburg), Hai-Jun Jin (KIT), and Yi Zhong (KIT) for providing CuPt starting alloys as well as already dealloyed samples.
- Heinz Krenn, for the fruitful cooperation with the Universität Graz facilitating the magnetic measurements.

Financial support by the Austrian science fund (FWF) is appreciated (project: S10405-N16)